Transport and correlations in one-dimensional interacting particle systems

A Thesis

Submitted to

Tata Institute of Fundamental Research, Mumbai, India

for the degree of

Doctor of Philosophy

in Physics

by

Avijit Das

International Centre for Theoretical Sciences

Tata Institute of Fundamental Research

Bangalore 560089, India

July, 2021

Final Version Submitted in Dec, 2021

Declaration

This thesis is a presentation of my original research work. Wherever contributions of others are involved, every effort is made to indicate this clearly, with due reference to the literature, and acknowledgement of collaborative research and discussions. The work was done under the guidance of Prof. Abhishek Dhar at International Centre for Theoretical Sciences, Tata Institute of Fundamental Research (ICTS-TIFR), Bangalore.

Avijit Das

Avijit Das
ICTS-TIFR, Bangalore

In my capacity as supervisor of the candidate's thesis, I certify that the above statements are true to the best of my knowledge.

Abhishek Dhar

Prof. Abhishek Dhar
ICTS-TIFR, Bangalore

Date : January 15, 2022

Certificate

I certify that this thesis entitled "**Transport and correlations in one-dimensional interacting particle systems**" comprises research work carried out by **Avijit Das** at International Centre for Theoretical Sciences under the supervision of **Prof. Abhishek Dhar** during the period 2015 - 2020 for the degree of Doctor of Philosophy of the Tata Institute of Fundamental Research (TIFR). The results presented in this thesis have not been submitted previously to this or any other University for a PhD or any other degree.

Head of Academics
International Centre for Theoretical Sciences
Tata Institute of Fundamental Research
Bangalore, India

Publication

1. **"Light-cone spreading of perturbations and the butterfly effect in a classical spin chain"** – *Avijit Das*, Saurish Chakrabarty, Abhishek Dhar, Anupam Kundu, David A. Huse, Roderich Moessner, Samriddhi Sankar Ray, Subhro Bhattacharjee, Physical Review Letters, **121**, 024101, (2018).
   DOI: https://doi.org/10.1103/PhysRevLett.121.024101

2. **"Nonlinear Fluctuating Hydrodynamics for the Classical XXZ Spin Chain"** – *Avijit Das*, Kedar Damle, Abhishek Dhar, David A Huse, Manas Kulkarni, Christian B Mendl, Herbert Spohn, Journal of Statistical Physics, **180**, 238-262, (2019).
   DOI: https://doi.org/10.1007/s10955-019-02397-y

3. **"Kardar-Parisi-Zhang scaling for an integrable lattice Landau-Lifshitz spin chain"** – *Avijit Das*, Manas Kulkarni, Herbert Spohn, Abhishek Dhar, Physical Review E, **100**, 042116, (2019).
   DOI: https://doi.org/10.1103/PhysRevE.100.042116

4. **"Quantum Brownian Motion: Drude and Ohmic Baths as Continuum Limits of the Rubin Model"** – *Avijit Das*, Abhishek Dhar, Ion Santra, Urbashi Satpathi, Supurna Sinha, Physical Review E, **102**, 062130, (2020).
   DOI: https://doi.org/10.1103/PhysRevE.102.062130

Acknowledgments

I acknowledge my guru Prof. Abhishek Dhar and other collaborators for their guidance, teaching and contribution towards the research presented in this thesis. I acknowledge my peers and other members of the stat-phys group at ICTS for stimulating discussions other fruitful research activities from time to time. Needless to mention that the funding, infrastructure, computing facilities and other basic amenities provided by ICTS-TIFR, IISc, NCBS have only made it possible to successfully pursue and finish the projects. The schools, conferences, workshops and discussion meetings frequently arranged by ICTS have played a significant role in bringing in new ideas and collaborations. I acknowledge ICTS, ICTP, MPIPKS and other funding agencies like Infosys to give me opportunities to visit ICTP and MPIPKS to attend conferences and contribute posters and talks. I also thank the friendly, highly competent administration, and all other staff and faculty members to solve any type of issues which have arisen from time to time.

Collaborators

I am thankful to the following collaborators of mine for their valuable discussions and contributions to the works presented in this thesis.

Prof. Abhishek Dhar[1]
Prof. Manas Kulkarni[1]
Prof. Subhro Bhattacharjee[1]
Prof. Anupam Kundu[1]
Prof. Samriddhi Sankar Ray[1]
Dr. Urbashi Satpathi[1]
Dr. Saurish Chakrabarty[1]
Prof. Kedar Damle[2]
Prof. Supurna Sinha[3]
Ion Santra[3]
Prof. David A. Huse[4]
Prof. Roderich Moessner[5]
Prof. Herbert Spohn[6]
Dr. Christian B. Mendl[7]

Affiliations during the time of collaboration:
1 – ICTS-TIFR, Bengaluru 560089, India. 2 – TIFR, Mumbai 400005, India.
3 – RRI, Bangalore-560080, India. 4 – Princeton University, Princeton, NJ 08544, USA.
5 – MPIPKS, 01187 Dresden, Germany. 6 – TUM, Garching, Germany.
7 – TUM, Institute of Scientific Computing, Dresden, Germany.

Contents

Overview **8**

1 Light-cone spreading of perturbations and the butterfly effect in a classical spin chain **9**

1.1 Introduction 10
1.2 The Heisenberg spin chain: 11
1.3 Classical OTOC analogue 12
1.4 Numerical Results 13
1.5 Summary 16
Bibliography 18

2 Nonlinear Fluctuating Hydrodynamics for the Classical XXZ Spin Chain **21**

2.1 Introduction 22
2.2 High-temperature, non-integrable and integrable Lattice Landau-Lifshitz equations 23
2.2.1 LLL equations 23
2.2.2 High-temperature diffusive regime 24
2.2.3 Integrable LLL model 27
2.3 Easy plane at low-temperatures 28
2.3.1 Low-temperature effective hamiltonian: 28
2.3.2 Nonlinear fluctuating hydrodynamics (NFH) in the low temperature regime: 32
2.4 Numerical results at low temperature 36
2.4.1 Simulation details 37
2.4.2 Case-I ($\nu = 0,\ h = 0.3$) 38
2.4.3 Case-II ($\nu = 0,\ h = 0$) 39
2.5 Discrete time LLL dynamics 40
2.5.1 Case-III ($\beta = 8.0, h = 0.3, N = 8192$) 43
2.5.2 Case-IV ($\beta = 8.0, h = 0.0, N = 8192$) 44
2.6 Summary 44

Appendices **46**
2.A Coupling coefficients for nonlinear fluctuating hydrodynamics 46
2.B Low temperature approximation 48
Bibliography 50

3 Kardar-Parisi-Zhang Scaling for an Integrable Lattice Landau-Lifshitz Spin Chain **53**
3.1 Introduction 54
3.2 The classical chain 56
3.2.1 KPZ equation and scaling functions 58
3.2.2 Simulation details 58
3.3 Simulation results for equilibrium dynamical correlations 60
3.3.1 Isotropic regime 60
3.3.2 Easy-plane regime 61
3.3.3 Easy-axis regime 62
3.4 Magnetization profile for step initial condition 62
3.5 Summary 63
Bibliography 65

4 Quantum Brownian Motion: Drude and Ohmic Baths as Continuum Limits of the Rubin Model **68**
4.1 Introduction 69
4.2 Hamiltonian and derivation of the generalised Langevin equation 70
4.2.1 Continuum string limit 74
4.3 Mean Square Displacement, Velocity Autocorrelation Function and Response Function 74
4.4 Comparison of the forms of $\gamma(t), \Delta(t)$ and $C(t)$ for the three models . . . 76
4.4.1 Form of $\gamma(t)$ 76
4.4.2 Form of $\Delta(t)$ 80
4.4.3 Form of $C(t)$ 83
4.4.4 Form of $R(t)$ 85
4.5 Summary 86
Bibliography 87

Overview

Hamiltonian systems can be broadly classified as integrable and non-integrable. An integrable Hamiltonian system is characterized by having sufficiently large number of independent constants of motion, whereas a non-integrable or chaotic system possesses only a handful number of, in most cases just one or two, conserved quantities. A classical Hamiltonian system with n degrees of freedom is said to be integrable if there exists n independent constants of motion $f_1, f_2, \cdots, f_n$ which Poisson commute: $\{f_i, f_j\} = 0$ for all $i, j = 1, 2, \cdots, n$. It is known that the transport properties of integrable and non-integrable systems are usually very different. One probe of transport properties is through equilibrium correlation functions of conserved quantities — the difference observed here typically is ballistic scaling for integrable systems and diffusive scaling for non-integrable ones. Recently, much progress has been made in our understanding of transport in one-dimensional systems using the theory of non-linear fluctuating hydrodynamics [for non-integrable, mostly classical, see Spohn, Lect. Notes in Phys. **921**, 107-155 (2017)] and generalized hydrodynamics [for integrable, both classical and quantum systems, see Doyon, SciPost Phys. Lect. Notes **18** (2020)]. A different probe that has recently been used to characterize chaos in many-body quantum systems is the so-called OTOC. This quantifies the propagation of chaos and attempts are currently being made to relate this to transport [see Khemani et al., PRB **98**, 144304].

The first two chapters consider a specific paradigmatic example of a non-integrable one-dimensional system, namely the classical Heisenberg spin chain. (a) **(ch1)** A classical analogue of the OTOC is studied to understand chaos propagation in this system and its possible relation to transport. (b) **(ch2)** Some predictions of nonlinear fluctuating hydrodynamics on anomalous scaling of correlation functions at low temperatures are tested via simulations. The last two chapters consider integrable models. **(ch3)** In one case we consider an integrable version of the classical Heisenberg spin chain and ask whether recent observations of anomalous transport properties in quantum integrable spin chains [see Bulchandani et al., arXiv:2013.01976] are also seen in the classical system. **(ch4)** In the second case we consider the harmonic chain and study the effective dynamics of a tagged particle and emergence of quantum Brownian motion — one main interest is to understand precisely the Ohmic and Drude limits and the detailed form of the mean square displacement and velocity autocorrelation function.

Chapter 1

Light-cone spreading of perturbations and the butterfly effect in a classical spin chain

Key ideas: We find that the effects of a localized perturbation in a chaotic classical many-body system–the classical Heisenberg chain at infinite temperature–spread ballistically with a finite speed even when the local spin dynamics is diffusive. We study two complementary aspects of this butterfly effect: the rapid growth of the perturbation, and its simultaneous ballistic (light-cone) spread, as characterized by the Lyapunov exponents and the butterfly speed, respectively. We connect this to recent studies of the out-of-time-ordered commutators (OTOC), which have been proposed as an indicator of chaos in a quantum system. We provide a straightforward identification of the OTOC with a natural correlator in our system and demonstrate that many of its interesting qualitative features are present in the classical system. Finally, by analyzing the scaling forms, we relate the growth, spread and propagation of the perturbation with the growth of one-dimensional interfaces described by the Kardar-Parisi-Zhang (KPZ) equation.

1.1 Introduction

The butterfly effect [1–3] is a vivid picture for the sensitivity of a spatially extended chaotic many-body system to arbitrarily small changes to its initial conditions. In this picture, this exquisite sensitivity – the proverbial butterfly wing-beat is enough to make the difference between presence or absence of a tornado – perhaps takes precedence over the fact that these changes are global – tornado activity is toggled in a place far away from the butterfly. While this sensitivity to initial conditions is well-studied and quantified via the (positive) Lyapunov exponents, the spatial spreading of the perturbation has received somewhat less attention. This spreading, if ballistic, is characterized by a *butterfly speed*. Lyapunov exponents and butterfly speed thus encode two complementary aspects of the butterfly effect.

These issues have acquired additional interest in the context of many recent studies of scrambling of information in quantum many body systems [4–22]. In this setting, the out-of-time-ordered commutator (OTOC) [23, 24] has emerged as a diagnostic [5–9, 9–23]: for two Hermitian operators $\hat{W}(x,t)$ and $\hat{V}(0,0)$ localized around x at time t and $x=0$ at time $t=0$ respectively, the OTOC, defined as $F(t) = -\langle[\hat{W}(x,t),\hat{V}(0,0)]^2\rangle$, estimates the effect of the operator, $V(0,0)$ on the measurement of operator, $W(x,t)$. In a class of large N gauge theories it was found that, for a given x and t, the OTOC is generically characterized by an exponent $\tilde{\lambda}$, and a velocity $\tilde{v}_{\rm B}$, which are respectively the measure of the exponential growth and the speed of spreading of the initially localized perturbation. Analogous to classical dynamical systems, the former is often identified with the largest Lyapunov exponent, and the latter with the butterfly speed.

Interestingly, these twin features are present even when the usual probes for relaxation and equilibration in a many-body system, the two-point functions $\langle\hat{W}(t)\hat{V}(0)\rangle$, are diffusive and hence do not capture the above ballistic spread. This was observed in a study of the OTOC in a system with diffusive energy transport– the one-dimensional Bose-Hubbard chain [18, 25] and diffusive metals [26] at finite temperature and also in the context of random unitary circuits [27, 28], which lend themselves to a considerable degree of analytical and numerical insight [29–31].

In this chapter, we present a detailed analysis of the spatiotemporal evolution of the divergence of the dynamical trajectories of perturbed and unperturbed systems. Our model is a well-known classical many-body system–the Heisenberg spin-chain at high temperatures, whose classical Hamiltonian dynamics of the spins is diffusive. We first identify a correlator which represents a natural classical limit of an OTOC, and turns out to be a very simple quantity: the decrease of the correlation between the system and its perturbed copy under time evolution. In particular, we find that the divergence of dynamical trajectories spreads in space ballistically. We provide an accurate extraction of the corresponding Lyapunov exponent and butterfly speed, and provide a description

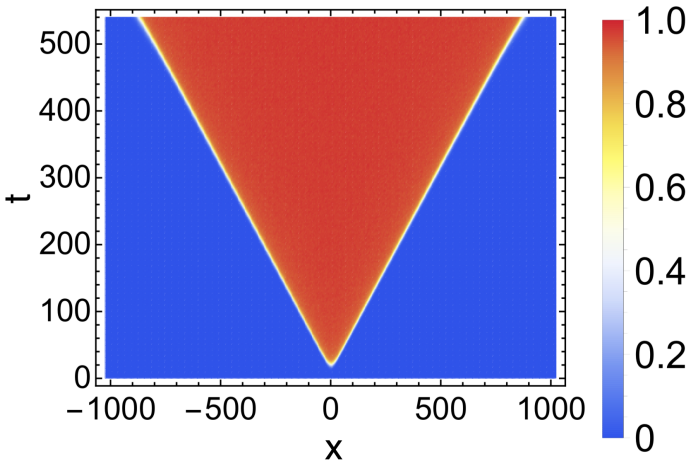

Figure 1.1: Simultaneous growth and ballistic spread of a perturbation in a classical Heisenberg spin chain whose spin dynamics [Fig. (1.4)] is diffusive at $T = \infty$. The speed of spreading obtained from the classical OTOC, $D(x,t)$ (see text), defines a "light cone". The results are shown for a perturbation at time $t = 0$ of size $\varepsilon = 10^{-3}$ at the center of a system of size $L = 2048$.

of the variations in the divergence between different initial states in terms of a KPZ-based analysis, which yields scaling forms for the distributions.

Our work connects to earlier studies of the propagation of chaos on coupled map lattices with discrete time evolution [32, 33], partial differential equations [34–36] and anharmonic coupled oscillator chains [37], where the concept of a velocity-dependent Lyapunov exponent was formulated [32, 38, 39] and related to the speed of spread of correlations [37]. In parallel, the concrete classical limit of the OTOC provides a natural platform to investigate the existence and nature of intrinsic differences in spatio-temporal chaos between classical and quantum many-body systems [40–42].

1.2 The Heisenberg spin chain:

We consider a one-dimensional lattice of spins $\mathbf{S}_x$, $x = 0, \ldots, N-1$ described by the Heisenberg Hamiltonian

$$\mathcal{H} = -J \sum_{x=0}^{N-1} \mathbf{S}_x \cdot \mathbf{S}_{x+1} \ , \tag{1.1}$$

where $J > 0$ and $\mathbf{S}_x$ are unit three component classical vectors and we take periodic boundary conditions $\mathbf{S}_x \equiv \mathbf{S}_{x+N}$. We consider a classical precessional dynamics

$$\frac{d\mathbf{S}_x}{dt} = J\mathbf{S}_x \times (\mathbf{S}_{x-1} + \mathbf{S}_{x+1}) = \{\mathbf{S}_x, H\} \ , \tag{1.2}$$

where the spin-Poisson bracket is defined as $\{f, g\} = \sum_x \sum_{\alpha,\beta,\gamma} \epsilon^{\alpha\beta\gamma} S_x^\gamma (\partial f/\partial S_x^\alpha)(\partial g/\partial S_x^\beta)$ for arbitrary functions f, g of the spin variables.

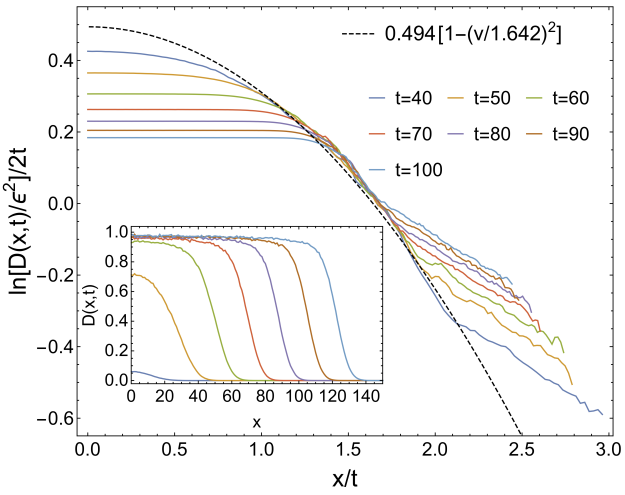

Figure 1.2: The inset plots $D(x,t)$ as a function of x, at different times ($t = 40, 50, \cdots 100$), showing growth and ballistic propagation of the perturbation front. The scaled data (main panel) shows that the front is fit well by Eq. (1.6) with $\mu = 0.494$ and $v_b = 1.642$ near $x \sim v_b t$. Here $\epsilon = 10^{-8}$ and averaging was done over 2×10^4 realizations.

1.3 Classical OTOC analogue

We consider two spin configurations which, at $t = 0$, differ *only* at site $x = 0$ by a rotation, ε, that is either small or infinitesimal, about an axis $\hat{\mathbf{n}} = (\hat{\mathbf{z}} \times \mathbf{S}_0)/|\hat{\mathbf{z}} \times \mathbf{S}_0|$ (where $\hat{\mathbf{z}}$ is the unit vector along the global z-axis) such that $\delta\mathbf{S}_0 = \varepsilon(\hat{\mathbf{n}} \times \mathbf{S}_0)$. We study the spreading of such a localized perturbation. For infinitesimal ε, the change at some point x is given by $\delta S_x^\alpha(t) \approx (\partial S_x^\alpha(t)/\partial S_0^\beta)\delta S_0^\beta = \varepsilon\ n^\gamma \epsilon^{\beta\gamma\nu} S_0^\nu\ (\partial S_x^\alpha(t)/\partial S_0^\beta) = \varepsilon\ n^\gamma \{S_x^\alpha(t), S_0^\gamma(0)\}$. To measure the evolution of the perturbation we define

$$2D(x,t) := \langle (\delta\mathbf{S}_x(t))^2 \rangle \approx \varepsilon^2 \langle \{\mathbf{S}_x(t), \hat{\mathbf{n}} \cdot \mathbf{S}_0\}^2 \rangle. \tag{1.3}$$

where, throughout this chapter, $\langle \cdots \rangle$ denotes averaging over spin configurations chosen from the equilibrium distribution $P(\{\mathbf{S}_x\}) = e^{-\mathcal{H}/T}/Z(T)$ and $Z(T)$ is the partition function. Denoting the two initial spin configurations discussed above by $\{\mathbf{S}_x^a(t=0)\}$ and $\{\mathbf{S}_x^b(t=0)\}$, we can obtain a simpler expression as

$$D(x,t) = 1 - \langle \mathbf{S}_x^a(t) \cdot \mathbf{S}_x^b(t) \rangle. \tag{1.4}$$

where $\langle \mathbf{S}_x^a(t) \cdot \mathbf{S}_x^b(t) \rangle$ is the *cross-correlator* between the two copies. If the dynamics is chaotic, as is known to be in this classical spin-chain at infinite temperatures [43, 44], we expect that for any $x \neq 0$, the above quantity, as a function of time, t, starts from the value 0 (when the spins of the two copies at a given x are perfectly correlated) and asymptotes to 1 (when they are completely decorrelated). *Thus $D(x,t)$ indeed measures the spatiotemporal evolution of decorrelation throughout the system.* Apart from $D(x,t)$, we also calculate the usual dynamic spin-correlation function

$$C(x,t) = \langle \mathbf{S}_x(t) \cdot \mathbf{S}_0(0) \rangle\ . \tag{1.5}$$

At this point, it is useful to understand the connection between $D(x,t)$ and the OTOC.

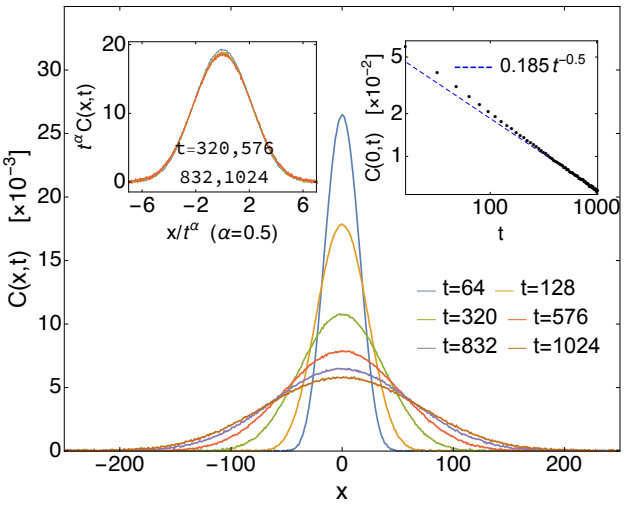

Figure 1.3: The spatial profile of $C(x,t)$ [Eq. (1.5)] at different times, t, for a system of size $L = 512$ at $T = \infty$ with averaging over 10^5 initial conditions. The left inset shows a collapse of the data after a diffusive scaling of $x/\sqrt{t}$ while the right inset shows the resultant $t^{-1/2}$ scaling of the auto-correlation.

On canonical quantization of the theory obtained by replacing the Poisson bracket with the commutator, i.e., $\{f, g\} \to \frac{1}{i\hbar}[f, g]$, we get $D(x,t) \to -\frac{\varepsilon^2}{\hbar^2} Tr\left[\rho_T([\mathbf{S}_x(t), \hat{\mathbf{n}} \cdot \mathbf{S}_0(0)])^2\right]$, where $\mathbf{S}_x$ are now quantum operators. This is nothing but the finite temperature generalization of the OTOC introduced earlier with $\hat{W}(x,t) = \mathbf{S}_x(t)$ and $\hat{V}(0,0) = \varepsilon \hat{\mathbf{n}} \cdot \mathbf{S}_0(0)$.

1.4 Numerical Results

We now present representative results of our numerical simulation of the Heisenberg spin chain with periodic boundary conditions. The simulations were performed using a fourth-order Runge-Kutta (RK4) numerical integration scheme for the spin dynamics. For the numerical simulations, energy is measured in units of J. The time-step in RK4 was taken to be $\Delta t = 0.001 - 0.005$ such that the energy/site and magnetization/site were conserved up to $\sim 10^{-12}$. The configuration averaging was done over $\sim 10^5$ equilibrated initial conditions for $C(x,t)$ and $\sim 10^4$ for $D(x,t)$. Many of the simulations had to be performed at quadruple level machine precision.

Our first main finding, namely ballistic propagation of the de-correlation, is summarised in Fig. (1.2) which shows that the OTOC falls sharply outside a light cone. The light cone is specified by the lines $x = \pm v_b t$ where v_b is the butterfly speed. For the two systems whose de-correlation $D(x,t)$ measures, the red region in Fig. (1.2) corresponds to complete de-correlation with $\langle \mathbf{S}_x^a(t) \cdot \mathbf{S}_x^b(t) \rangle \cong 0$. This also gives the natural definition of the *light-cone* velocity in the sense of a "classical Lieb-Robinson speed" [45–47] which is then equal to the butterfly speed.

In Fig. (1.3) we plot the signal $D(x,t)$ at different times to show the propagation of the front. As can be seen from the scaling, the front (for $x \sim v_b t$) is fit well by

$$D(x,t) = \varepsilon^2 \exp\left[2\mu t(1 - (x/v_b t)^2)\right] , \tag{1.6}$$

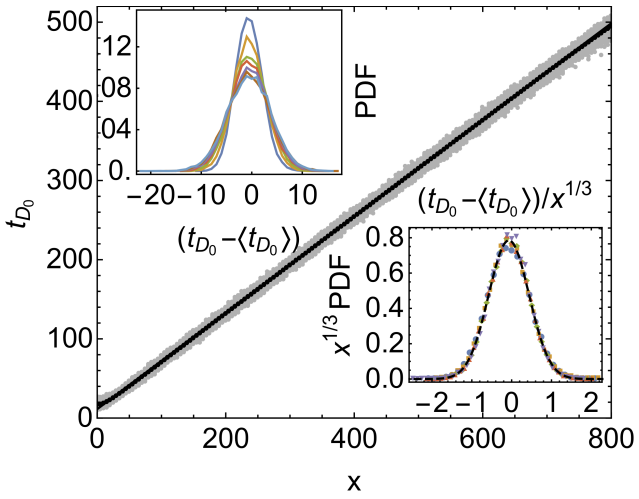

Figure 1.4: The main panel shows t_{D_0} (defined in the main text) as a function of x, for $D_0 = 100\epsilon = 0.1$ and different initial spin-configurations (grey scatter). The mean (black connected data-points) over 10^4 configurations is also shown and has a slope $\approx 1/(1.6417(2))$. The upper inset shows the distribution of t_{D_0} at space-points $x = 100, 200, \ldots, 700$ while the lower inset shows collapse of the distributions with a width scaling as $\sim x^{1/3}$. The dotted curve in the lower inset is the Gaussian fit to the fluctuations at $x = 600$.

with $\mu \approx 0.494$, $v_b \approx 1.6417(2)$. The deviations in scaling seen for $x \sim v_b t$ arise from errors due to finite machine precision (quadruple level precision in this case). Later [see Fig. (1.4)] we shall see that working with a linearized dynamics avoids these errors and we get much better collapse of data in the entire range. The scaling function is quite accurate within the light cone but in general is only an approximate fit for $x \gtrsim v_b t$. The finite butterfly speed is in stark contrast with the entirely diffusive [48] spin dynamics as recorded by the regular two point correlator $C(x,t)$ (Eq. (1.5)) shown in Fig. (1.4). The characteristic signature of diffusion– $x/\sqrt{t}$ collapse at long times– is clearly visible in the insets of Fig. (1.4).

An alternate way of analyzing the data is to ask at what time, t_{D_0}, the signal attains a threshold value D_0 at a given x for a set of different realization of random initial configurations. In Fig. (1.4) we plot the resulting set of t_{D_0}'s as a function of x. Its mean grows as $t_{D_0} = x/v_b$, with $v_b \approx 1.64$ in accordance with Fig. (1.3). Importantly, there is a spread of times for the arrival of the front leading to a distribution of times t_{D_0} for a given x. This distribution for different values of x as well as its collapse indicating a $x^{2/3}$ scaling of variance of t_{D_0} is shown in the inset of Fig. (1.4). Thus there are variations between different initial states in the timing of the front's arrival that are of order $\sim x^{1/3}$.

We next analyze the properties of the front in more detail, starting with its exponential growth in the temporal regime and then considering its fluctuations within a KPZ framework. From the usual definition of the Lyapunov exponents, we expect the quantity $\lim_{\epsilon\to 0} \delta S_x(t)^2/\epsilon^2$ to grow exponentially with time (at large, but finite times) as $\sim e^{2\lambda(\mathbf{S},t)t}$, for any x, where the Lyapunov exponent at time t, $\lambda(\mathbf{S},t)$, may depend on the initial spin-configuration $\{\mathbf{S}\}$ of a given realization. In the limit $\varepsilon \to 0$, it is possible to write the linearized equation of motion for $\lim_{\epsilon\to 0} \delta\mathbf{S}_x := \mathbf{z}_x$,

$$\dot{\mathbf{z}}_x = J\mathbf{S}_x \times (\mathbf{z}_{x-1} + \mathbf{z}_{x+1}) + J\mathbf{z}_x \times (\mathbf{S}_{x-1} + \mathbf{S}_{x+1}) \ , \tag{1.7}$$

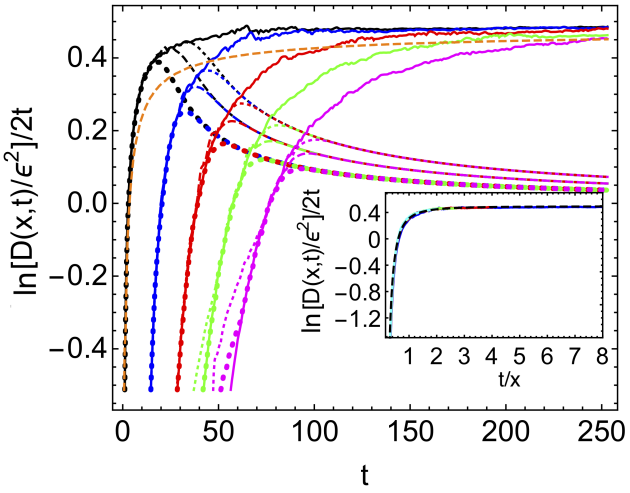

Figure 1.5: (a) Plot of $\ln[D(x,t)/\varepsilon^2]/(2t)$ versus t at $x = 0$ (black), 32, 64, 96, 128 (magenta), for $\varepsilon = 10^{-4}$ (thick dotted lines), $\varepsilon = 10^{-6}$(dashed lines) and $\varepsilon = 10^{-8}$ (thin dotted lines), for $L = 1024$ from solving the non-linear Equation of motion [Eq. (1.2)]. The solid lines are results from the linearized dynamics and correspond to the limit $\epsilon \to 0$ and hence gives λ_D (see text). The dashed orange line corresponds to $\langle \ln[\delta \mathbf{S}^2(x,t)/2\varepsilon^2]\rangle/(2t)$, obtained from the linearized dynamics for $x = 0$ and we see the slightly different saturation value corresponding to λ_L (see text). (b) Inset plots the results for the linearized dynamics for $x = 32, 64, 96, 128$ on scaling the time axis by x. The collapsed data approximately fits the solid line corresponding to the scaling form Eq. (1.6) with $\mu \approx 0.494, v_b \approx 1.64$.

where $\mathbf{S}$, obtained by solving the equation of motion Eq. (1.2) for a given random initial configuration, acts as the dynamic field for $\mathbf{z}$. The linearised equation can then be used to obtain the Lyapunov exponent. By sampling random initial configurations, we can then define an average exponent $\lambda_L(t) = \langle \lambda(\mathbf{S}, t)\rangle$. Given [from Eq. (1.4)], $D(x,t) = \langle (\delta \mathbf{S}_x(t))^2\rangle/2$, we expect $\lim_{\epsilon\to 0} D(x,t)/\epsilon^2$ to grow exponentially with time as $\sim e^{2\lambda_D(t)t}$. However, the rate of growth, quantified by $\lambda_D(t)$ is in general different from $\lambda_L(t)$, due to the difference in the order of averaging. A straightforward application of Jensen's inequality [49] gives $\lambda_L(t) \leq \lambda_D(t)$ at any finite time where the two values become equal in the limit $t \to \infty$ as the width of the distribution of $\lambda(\mathbf{S}, t)$ decreases as $t^{-2/3}$ (see below).

Fig. (1.4) compares the numerical results of the linearised and non-linear equations of motion, which confirms the above expectations. In the limit $t \to \infty$, we find from linear extrapolation of our data $\lambda_L(\infty) = \lambda_D(\infty) := \lambda \approx 0.492(5)$. This compares well with the value of $\lambda \approx 0.47$ reported earlier [43]. For any small but finite ε, $D(x,t)$ would eventually saturate to the value 1, when de-correlation is complete [see Eq. (1.4)]. The time for saturation goes as $\sim -\ln\varepsilon/\lambda$. Hence, the exponential growth-regime lasts longer for smaller ε. This can be seen in Fig. (1.4) where we also plot the results from the non-linear dynamics for values of $\varepsilon = 10^{-4}, 10^{-6}$ and 10^{-8}. The inset shows that for the linearized dynamics, the scaling form in Eq. (1.6) holds accurately over the entire time range, with $\mu \approx \lambda_D$. This means that we can identify a velocity dependent Lyapunov exponent through the relation $D(x = vt, t) \sim e^{2\mu(v)t}$ with $\mu(v) = \lambda_D[1 - (v/v_b)^2]$ to a very good approximation. For the non-linear dynamics, as seen in Fig. (1.3), the scaling form holds only for $x \sim v_b t$.

We now turn to the issue of realization to realization fluctuation of the wave-front

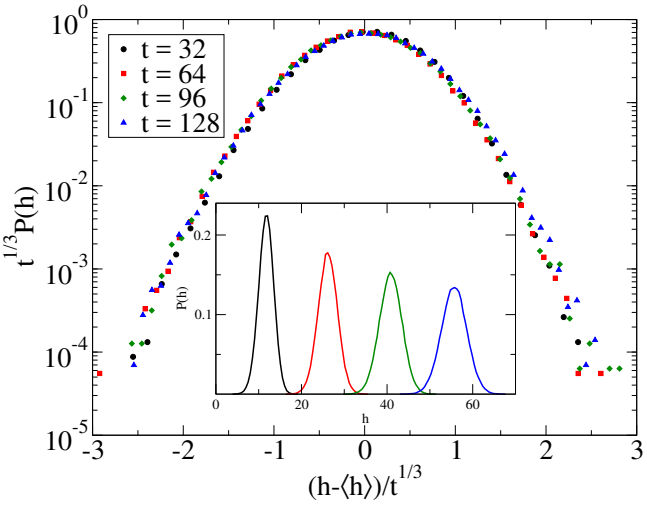

Figure 1.6: Distribution of the "height" variable $h(x,t) = \log[\delta\mathbf{S}^2(x,t)/\epsilon^2]/2$ at $x = 0$. The inset shows the distribution of $h(0,t)$ at different times while the main plot shows the collapse of data obtained after a $t^{1/3}$ scaling.

and the finite variance in the arrival times, t_{D_0}, at a given x [Fig. (1.4)]. We define

$$h(x,t) = \lim_{\epsilon\to 0} \log[\delta\mathbf{S}^2(x,t)/2\epsilon^2]/2 \tag{1.8}$$

(where we no longer average over initial configurations) and calculate $h(x,t)$ using the linearized equation of motion [Eq. (1.7)] for $\mathbf{z}_x$. Our results so far suggest that

$$h(x = vt, t) = t\mu(v) + t^{1/3}\eta(x,t) \ , \tag{1.9}$$

where $\mu(v)$ is the velocity-dependent Lyapunov exponent, and η describes the fluctuations. In Fig. (1.4) we see that the probability distribution of $h(0,t)$ shows a clear $t^{1/3}$ scaling as mentioned above.

The above observation leads us to interpret the dynamics of $h(x,t)$ as similar to the problem of interface growth [50] with $h(x,t)$ as the "height function". In particular, our numerical results for both $h(x,t)$ and $D(x,t)$ are consistent with the growth of height, as predicted from the KPZ equation for the so-called "wedge" initial conditions [51]. This would then suggest that the variable η follow a Tracy-Widom distribution. However, our system should differ from KPZ in that the noise from the chaos should have power-law correlations in time due to the diffusing conserved energy and magnetization densities. The distributions in Fig. (1.4) inset and Fig. (1.4) are found to be more symmetric than Tracy-Widom and closer to Gaussians. The reasons for this are at present unclear.

1.5 Summary

We have studied the butterfly effect in a classical Heisenberg spin chain at infinite temperature and have shown that a systematic understanding of this effect includes two simultaneous, but logically complementary aspects – the exponential growth and ballistic spread of an infinitesimal local perturbation determined by the Lyapunov exponents

and the butterfly speed. Both effects are quantified by an appropriately defined measure that is naturally related to the OTOC recently studied in context of scrambling in quantum many-body systems [9–12, 14–16, 24, 52–55]. Though we have presented infinite temperature results, the above features of the butterfly effect survive at finite $T/J \gg 1$. We have obtained the scaling-form of the fluctuations of the propagation front via the KPZ model for interface growth. Notably, the above ballistic spread of perturbation is present even while the usual two-point dynamic spin correlator shows diffusion and hence does not reflect correlations spreading with the butterfly speed. A natural question then pertains to the nature of correlators that are directly sensitive to this ballistic effect. A closely related desideratum is an analytical derivation of the equation of motion for the propagating ballistic front. The features reported here for the nearest neighbor spin-chain are expected to survive in presence of further neighbor couplings, albeit, with different values for λ and v_b. Such issues and particularly the effect of long-range spin exchanges form interesting future avenues of research, particularly the latter where the ballistic effects may not survive.

Bibliography

[1] E. N. Lorenz, *The essence of chaos* (University of Washington Press, Seattle, Washington, 1993).

[2] R. C. Hilborn, American Journal of Physics **72**, 425 (2004).

[3] E. Lorenz, World Scientific Series on Nonlinear Science Series A **39**, 91 (2000).

[4] I. L. Aleiner, L. Faoro, and L. B. Ioffe, Annals of Physics **375**, 378 (2016).

[5] Y. Sekino and L. Susskind, Journal of High Energy Physics **10**, 065 (2008).

[6] S. H. Shenker and D. Stanford, Journal of High Energy Physics **03**, 067 (2014), arXiv:1306.0622 [hep-th] .

[7] W. Brown and O. Fawzi, arXiv preprint arXiv:1210.6644 (2012).

[8] N. Lashkari, D. Stanford, M. Hastings, T. Osborne, and P. Hayden, Journal of High Energy Physics **4**, 22 (2013).

[9] J. Maldacena, S. H. Shenker, and D. Stanford, Journal of High Energy Physics **8**, 106 (2016).

[10] E. B. Rozenbaum, S. Ganeshan, and V. Galitski, Physical Review Letters **118**, 086801 (2017).

[11] N. Tsuji, T. Shitara, and M. Ueda, arXiv preprint arXiv:1706.09160 (2017).

[12] E. Iyoda and T. Sagawa, arXiv preprint arXiv:1704.04850 (2017).

[13] I. Kukuljan, S. Grozdanov, and T. Prosen, arXiv preprint arXiv:1701.09147 (2017).

[14] J. Kurchan, arXiv preprint arXiv:1612.01278 (2016).

[15] D. A. Roberts and B. Swingle, Physical review letters **117**, 091602 (2016).

[16] B. Swingle, G. Bentsen, M. Schleier-Smith, and P. Hayden, Physical Review A **94**, 040302 (2016).

[17] B. Swingle and D. Chowdhury, Physical Review B **95**, 060201 (2017).

[18] A. Bohrdt, C. Mendl, M. Endres, and M. Knap, New Journal of Physics **19**, 063001 (2017).

[19] D. Stanford, Journal of High Energy Physics **10**, 9 (2016).

[20] S. Banerjee and E. Altman, Physical Review B **95**, 134302 (2017).

[21] S. H. Shenker and D. Stanford, Journal of High Energy Physics **3**, 067 (2014).

[22] P. Hosur, X.-L. Qi, D. A. Roberts, and B. Yoshida, Journal of High Energy Physics **2016**, 4 (2016).

[23] A. I. Larkin and Y. N. Ovchinnikov, Soviet Journal of Experimental and Theoretical Physics **28**, 1200 (1969).

[24] A. Y. Kitaev, KITP Program: Entanglement in Strongly- Correlated Quantum Matter (2015).

[25] H. Shen, P. Zhang, R. Fan, and H. Zhai, Physical Review B **96**, 054503 (2017).

[26] A. A. Patel, D. Chowdhury, S. Sachdev, and B. Swingle, Physical Review X **7**, 031047 (2017).

[27] V. Khemani, A. Vishwanath, and D. A. Huse, arXiv preprint arXiv:1710.09835 (2017).

[28] T. Rakovszky, F. Pollmann, and C. von Keyserlingk, arXiv preprint arXiv:1710.09827 (2017).

[29] C. von Keyserlingk, T. Rakovszky, F. Pollmann, and S. Sondhi, arXiv preprint arXiv:1705.08910 (2017).

[30] A. Nahum, J. Ruhman, S. Vijay, and J. Haah, Physical Review X **7**, 031016 (2017).

[31] A. Nahum, S. Vijay, and J. Haah, arXiv preprint arXiv:1705.08975 (2017).

[32] K. Kaneko and I. Tsuda, *Complex systems: chaos and beyond: a constructive approach with applications in life sciences* (Springer Science & Business Media, 2011).

[33] S. Lepri, A. Politi, and A. Torcini, Journal of statistical physics **82**, 1429 (1996).

[34] J. A. Vastano and H. L. Swinney, Physical Review Letters **60**, 1773 (1988).

[35] P. Gaspard, M. Briggs, M. Francis, J. Sengers, R. Gammon, J. R. Dorfman, and R. Calabrese, Nature **394**, 865 (1998).

[36] P. Grassberger, Nature (London) **401**, 875 (1999).

[37] G. Giacomelli, R. Hegger, A. Politi, and M. Vassalli, Physical review letters **85**, 3616 (2000).

[38] R. J. Deissler and K. Kaneko, Physics Letters A **119**, 397 (1987).

[39] S. Lepri, A. Politi, and A. Torcini, Journal of statistical physics **88**, 31 (1997).

[40] T. Scaffidi and E. Altman, arXiv preprint arXiv:1711.04768 (2017).

[41] V. Khemani, D. A. Huse, and A. Nahum, arXiv preprint arXiv:1803.05902 (2018).

[42] Z. Nussinov, F. Nogueira, M. Blodgett, and K. Kelton, arXiv preprint arXiv:1409.1915 (2014).

[43] A. de Wijn, B. Hess, and B. Fine, Physical review letters **109**, 034101 (2012).

[44] J. Das, M. Rao, and S. Ramaswamy, EPL (Europhysics Letters) **60**, 418 (2002).

[45] E. H. Lieb and D. W. Robinson, in *Statistical Mechanics* (Springer, 1972) pp. 425–431.

[46] D. Métivier, R. Bachelard, and M. Kastner, Physical Review Letters **112**, 210601 (2014).

[47] C. Marchioro, A. Pellegrinotti, M. Pulvirenti, and L. Triolo, Journal of Statistical Physics **19**, 499 (1978).

[48] R. Gerling and D. Landau, Physical Review B **42**, 8214 (1990).

[49] J. L. W. V. Jensen, Acta Math. **30**, 175 (1906).

[50] A. S. Pikovsky and J. Kurths, Physical Review E **49**, 898 (1994).

[51] S. Prolhac and H. Spohn, Physical Review E **84**, 011119 (2011).

[52] S. Sachdev and J. Ye, Physical Review Letters **70**, 3339 (1993).

[53] A. Lucas, Y. Gu, and X.-L. Qi, SciPost Physics **2**, 018 (2017).

[54] A. A. Patel and S. Sachdev, Proceedings of the National Academy of Sciences **114**, 1844 (2017).

[55] Y. L. Zhang, Y. Huang, and X. Chen, arXiv preprint arXiv:1802.04492 (2018).

Chapter 2

Nonlinear Fluctuating Hydrodynamics for the Classical XXZ Spin Chain

Key ideas: Using the framework of nonlinear fluctuating hydrodynamics (NFH), we examine equilibrium spatio-temporal correlations in classical ferromagnetic spin chains with nearest neighbor interactions. In particular, we consider the classical XXZ-Heisenberg spin chain (also known as Lattice Landau Lifshitz or LLL model) evolving deterministically and chaotically via Hamiltonian dynamics, for which energy and z-magnetization are the only locally conserved fields. For the easy-plane case, this system has a low-temperature regime in which the difference between neighboring spin's angular orientations in the XY plane is an *almost conserved* field. According to the predictions of NFH, the dynamic correlations in this regime exhibit a heat peak and propagating sound peaks, all with anomalous broadening. We present a detailed molecular dynamics test of these predictions and find a reasonably accurate verification. We find that, in a suitable intermediate temperature regime, the system shows two sound peaks with Kardar-Parisi-Zhang (KPZ) scaling and a heat peak where the expected anomalous broadening is less clear. In high temperature regimes of both easy plane and easy axis case of LLL, our numerics show clear diffusive spin and energy peaks and absence of any sound modes, as one would expect. We also simulate an integrable version of the XXZ-model, for which the ballistic component instead moves with a broad range of speeds rather than being concentrated in narrower peaks around the sound speed.

2.1 Introduction

For generic classical and quantum spin chains the only conservation law is the energy, perhaps in addition one spin component (or all three). Momentum conservation is destroyed by the underlying lattice and in thermal equilibrium the average currents vanish. One therefore expects that a local perturbation of the thermal state will spread diffusively, a behavior which is actually observed in a large variety of systems, as prototypical examples we refer to[1, 2]. There are obvious exceptions such as integrable spin chains, for which a small perturbation induces a ballistic response. Also, at least classically, at very low temperatures the harmonic approximation generally becomes valid, which then implies ballistic transport over a suitable time scale.

The goal of this chapter is to explain that, beyond the standard folklore, there can be a parameter regime, in which the dynamic correlations consist of a "heat" peak at the origin and in addition two sound peaks symmetrically moving to the right and left. These peaks broaden sub-ballistically but faster than diffusion. The theoretical argument is based on nonlinear fluctuating hydrodynamics (NFH), which refers to long wavelength behavior and should thus be equally valid for both classical and quantum chains. For quantum chains, because of numerical limitations, it is difficult to pin down the phenomenon, even less so the precise scaling form. In this contribution we thus restrict our study to classical spin chains of XXZ type. We note that for off-lattice models, where there is momentum conservation (e.g anharmonic oscillator chains), the presence of sound peaks with anomalous scaling has been observed in several recent studies and is well understood within the framework of NFH [3, 4]. The results presented here for the XXZ model bear close resemblance to those seen for the rotor model, where early results in [5–7] indicated a diffusive to super-diffusive transport, and has recently been understood in the framework of NFH [8, 9]. It should also be noted that there are no phase transitions (from diffusive to anomalous transport regimes), rather the anomalous scaling is observed over very long transient time-scales.

For our argument we require that the anisotropy parameter $\Delta = |J_z/J_x| = |J_z/J_y|$, where J_z is the nearest neighbor coupling between z-components of spin and $J_x = J_y$ between the x or y-components respectively, satisfies $\Delta < 1$. Then, at high temperatures, energy and the z-component of the spin diffuse. However at low temperatures the spin motion is confined to a plane orthogonal to the z-axis (the easy-plane) and phase differences between neighboring spins are small. To achieve differences of order π (in other words "phase slips" or, equivalently, "umklapp") is an activated process and is thus strongly thermally suppressed in a low temperature regime. In this regime, the phase differences are an almost conserved field, so there is a broad range of time scales where this conservation law dictates the hydrodynamics. Under such conditions, nonlinear fluctuating hydrodynamics can be applied. The theory predicts the dynamical correlations

contain a central non-propagating heat peak and left- and right-moving sound peaks. The three peaks broaden as nontrivial powers of time according to characteristic explicitly known scaling functions [10, 11].

To illustrate the difference between sound peaks and ballistic broadening, we also simulate the integrable spin chain of Fadeev and Takhtajan [12]. The infinite number of conservation laws then leads to a structured scaling function which scales self-similarly as $\sim t^{-1} f(x/t)$.

There has been previous work on non-integrable classical models (and their KPZ connection) such as the Fermi-Pasta-Ulam chain [3, 4], the discrete nonlinear Schrödinger equation [13–15], coupled rotors [8, 9, 11], and one-dimensional hard-point systems [16]. However, to our knowledge the present work is the first exploration of NFH in classical spin chains.

2.2 High-temperature, non-integrable and integrable Lattice Landau-Lifshitz equations

2.2.1 LLL equations

We consider spins of unit length on the one-dimensional lattice, $\vec{S}_j = (S_j^x, S_j^y, S_j^z)$ with $|\vec{S}_j| = 1$, $j = 1, \cdots, N$. The standard LLL interaction is quadratic in the spins with Hamiltonian

$$H = -\sum_{j=1}^{N} \left(S_j^x S_{j+1}^x + S_j^y S_{j+1}^y + \Delta S_j^z S_{j+1}^z \right), \tag{2.1}$$

Δ the asymmetry parameter, $\Delta \geq 0$. The LLL equations of motion then read

$$\tfrac{d}{dt}\vec{S}_j = \{\vec{S}_j, H\} = \vec{S}_j \times \vec{B}_j, \quad \vec{B}_j = -\nabla_{\vec{S}_j} H, \tag{2.2}$$

where the Poisson bracket between two functions, g_1, g_2, of the spin variables is defined by $\{g_1, g_2\} = \sum_j \epsilon_{\alpha\beta\gamma} \left(\partial g_1/\partial S_j^\alpha\right)\left(\partial g_2/\partial S_j^\beta\right) S_j^\gamma$ with the usual summation convention. Clearly $|\vec{S}_j(t)| = 1$ for all times. The Hamiltonian character of the dynamics can be seen also by introducing the position-like angular variable $\phi_j \in S^1$ and the conjugate canonical momentum-like variable $s_j \in [-1, 1]$ defined through

$$S_j^x = f(s_j)\cos\phi_j, \quad S_j^y = f(s_j)\sin\phi_j, \quad S_j^z = s_j, \tag{2.3}$$

where $f(x) = (1-x^2)^{1/2}$. Indeed, one checks that $\{s_i, \phi_j\} = \delta_{ij}$, $\{\phi_i, \phi_j\} = 0$, $\{s_i, s_j\} = 0$. In these variables the Hamiltonian (2.1) reads

$$H = -\sum_{j=1}^{N} \Big(f(s_j) f(s_{j+1}) \cos(\phi_{j+1} - \phi_j) + \Delta s_j s_{j+1} \Big). \tag{2.4}$$

Thus at low energies the phases tend to align, while Δ sets the interactions between the z components. The isotropic model corresponds to $\Delta = 1$, easy-plane to $\Delta < 1$, and easy-axis to $\Delta > 1$. In the new variables the equations of motion become

$$\begin{aligned} \tfrac{d}{dt}\phi_j &= -f'(s_j) f(s_{j+1}) \cos(\phi_{j+1} - \phi_j) - f(s_{j-1}) f'(s_j) \cos(\phi_j - \phi_{j-1}) \\ &\quad - \Delta(s_{j-1} + s_{j+1}), \\ \tfrac{d}{dt} s_j &= f(s_j) f(s_{j+1}) \sin(\phi_{j+1} - \phi_j) - f(s_{j-1}) f(s_j) \sin(\phi_j - \phi_{j-1}). \end{aligned} \tag{2.5}$$

For $|s_j(t)| < 1$ the angle $\phi_j(t)$ is defined modulo 2π. For $s_j(t) = \pm 1$ the angle $\phi_j(t)$ is ill-defined. However, in our context, trajectories where a spin precisely hits either the north or south pole of the unit sphere ($|s_j(t)| = 1$) have measure zero and therefore can be ignored.

The s-s interaction could have additional contributions. One example is the ionic potential $\sum_j s_j^2$ [17]. Many of our results are valid in greater generality, but we explore the simplest case (2.5).

The LLL dynamics has two locally conserved fields, namely the z-component of the spin, s_j, and the energy

$$e_j = -f(s_j) f(s_{j+1}) \cos(r_j) - \Delta s_j s_{j+1}, \tag{2.6}$$

where for convenience we have introduced the phase difference $r_j = \phi_{j+1} - \phi_j$. From the equations of motion (2.5) one deduces the form of the spin current, $\mathcal{J}_j^{\mathsf{s}}$, and energy current, $\mathcal{J}_j^{\mathsf{e}}$, as

$$\mathcal{J}_j^{\mathsf{s}} = -f(s_{j-1}) f(s_j) \sin(r_{j-1}), \tag{2.7}$$

$$\begin{aligned} \mathcal{J}_j^{\mathsf{e}} &= f(s_{j-1}) f(s_j) f'(s_j) f(s_{j+1}) \sin(r_{j-1} + r_j) \\ &\quad + \Delta f(s_j) f(s_{j+1}) s_{j-1} \sin(r_j) + \Delta f(s_j) f(s_{j-1}) s_{j+1} \sin(r_{j-1}). \end{aligned} \tag{2.8}$$

2.2.2 High-temperature diffusive regime

We first assume that there are no further conservation laws. The equilibrium Gibbs measures are then given by the two-parameter family

$$Z_N(\beta, h)^{-1} \exp\Big[-\beta \Big(H - h \sum_j s_j \Big) \Big] \prod_j dr_j ds_j, \quad \beta \geq 0,\ h \in \mathbb{R}, \tag{2.9}$$

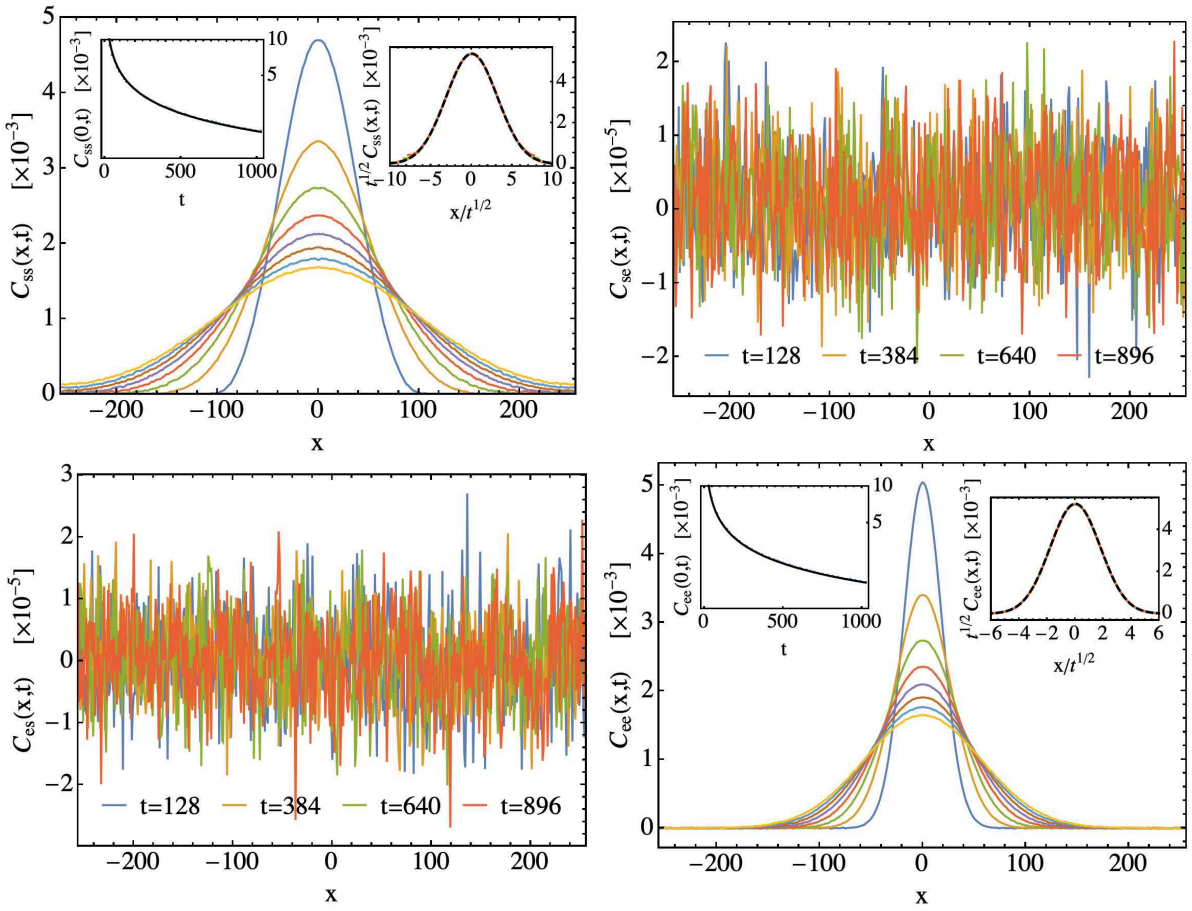

Figure 2.1: Plots of $C_{ab}(x,t)$ for XXZ easy plane regime at high temperature. Parameters are $\Delta = 0.5, \beta = 1$, $N = 512$ and $h = 0$. $C_{ss}(x,t)$ and $C_{ee}(x,t)$ are plotted at time $128, 256, ..., 1024$. Insets show the slow temporal decay of $C_{ss}(0,t)$ and $C_{ee}(0,t)$, and the diffusive scaling of $C_{ss}(x,t)$ and $C_{ee}(x,t)$ with the Gaussian fits at times $640, 768, 896$ and 1024. The diffusion constants are 4.95 and 1.72 for spin and energy respectively, obtained from the corresponding Gaussian fits and the decay of $C_{ss}(0,t), C_{ee}(0,t)$. As expected, energy and spin are uncorrelated.

for a chain of length N spins with periodic boundary conditions and partition function $Z_N(\beta, h)$. Infinite volume equilibrium averages will be denoted by $\langle\cdot\rangle_{\beta,h}$. We note that the Hamiltonian is even and the currents are odd in r_j. Hence

$$\langle \mathcal{J}^{\mathsf{s}}_j \rangle_{\beta,h} = 0, \quad \langle \mathcal{J}^{\mathsf{e}}_j \rangle_{\beta,h} = 0. \tag{2.10}$$

But then also their derivatives with respect to β, h vanish and, using the definition of the Drude weight given in [18], one concludes that both Drude weights are zero. Thus the conventional expectation is to have a diffusive spreading of the equilibrium time-correlations for spin and energy. Since they have opposite signature under time reversal, the cross diffusion coefficient should vanish.

To confirm, we performed molecular dynamics simulations at inverse temperature $\beta = 1$ (see Sec. 2.4 for simulation details). In Fig. (2.1) we show numerical results for

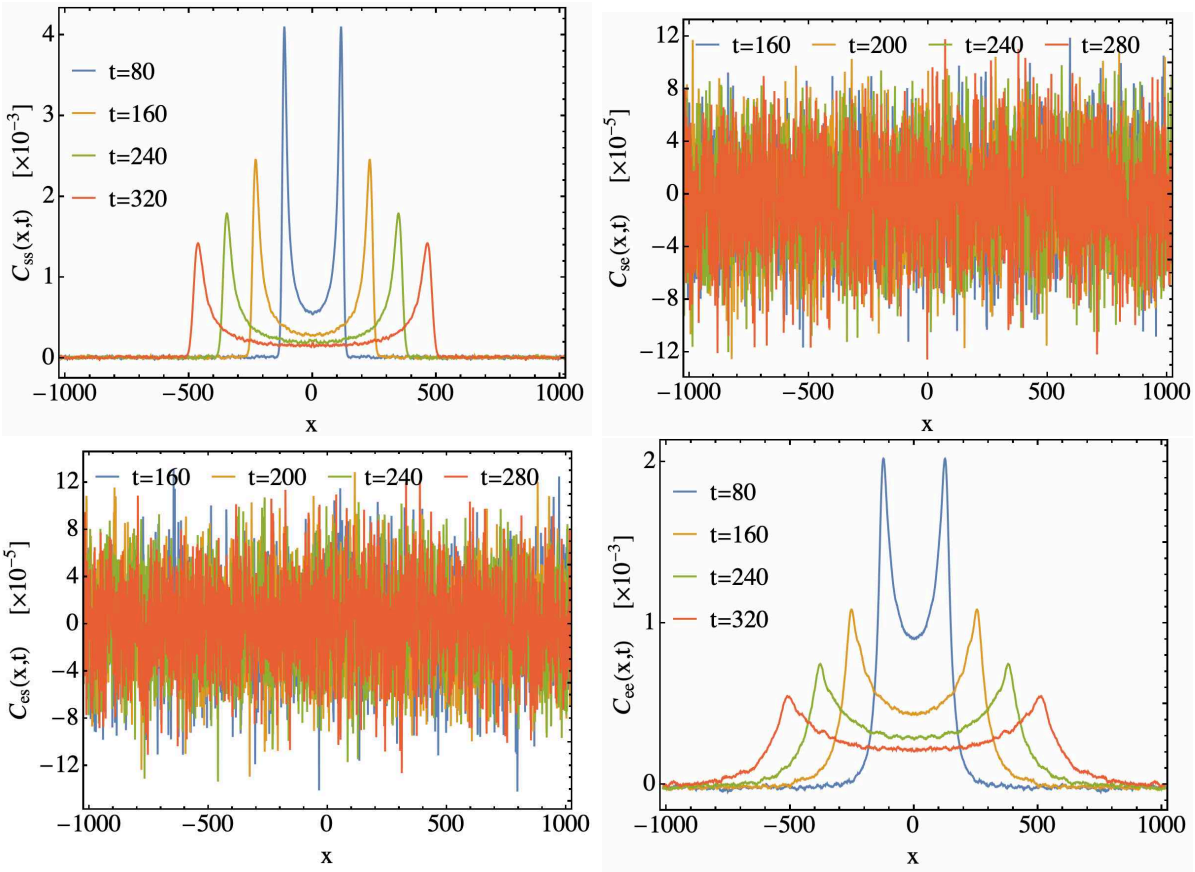

Figure 2.2: Plots of $C_{ab}(x,t)$ for the integrable LLL model in easy plane regime at high temperature at different times. Parameters are $\rho = 1.0, \beta = 1.0$ and $N = 2048$. The energy and spin are uncorrelated. Energy correlation reaches the boundary of the system faster than the spin correlation. From the maxima of the peaks, the estimated speed is 1.4448 for the spin mode, whereas it is 1.5888 for the energy mode. Scaling plots are shown in Fig. (2.3).

the spin and energy correlations defined by

$$\begin{aligned} C_{\rm ss}(j,t) &= \langle s_j(t) s_0(0)\rangle^{\rm c}_{\beta,h}, \\ C_{\rm ee}(j,t) &= \langle e_j(t) e_0(t)\rangle^{\rm c}_{\beta,h} \end{aligned} \tag{2.11}$$

where $\langle \dots \rangle^{\rm c}_{\beta,h}$ denotes the connected correlation defined as $\langle Q_j(t) Q_0(0)\rangle^{\rm c}_{\rm eq} := \langle (Q_j(t) - \langle Q_0\rangle_{\rm eq})(Q_0(0) - \langle Q_0\rangle_{\rm eq})\rangle_{\rm eq}$.

These simulations are for system size $N = 512$ and were run up to time $t = 1024$ [simulation details are given later in Sec. 2.4]. We see that spin and energy autocorrelations indeed show diffusive behavior, while there are no cross correlations.

The novelty of our contribution is to establish that at lower temperatures the dynamical properties change dramatically through the appearance of ballistic sound propagation. But before embarking on that discussion we use the opportunity to illustrate that equilibrium time-correlations for an integrable spin-chain are dominated by a broad ballistic

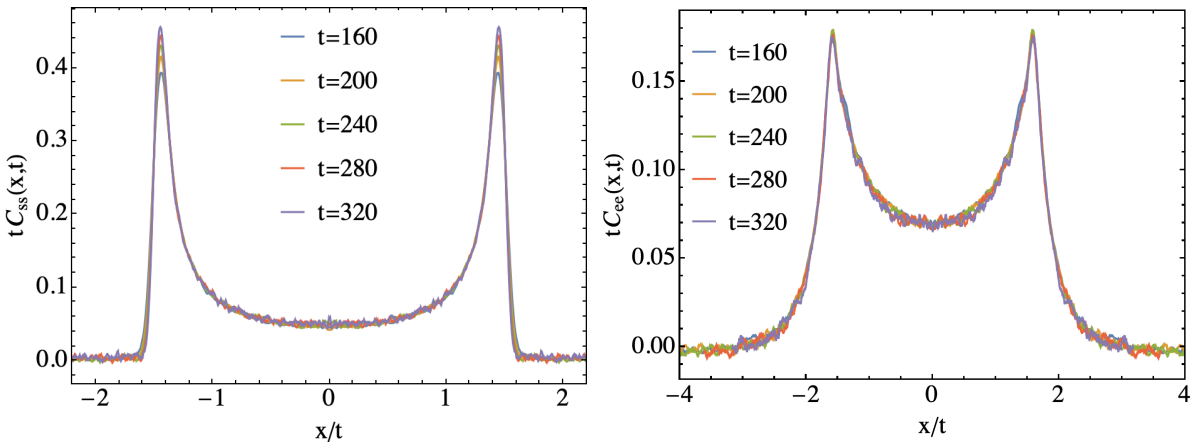

Figure 2.3: Scaling plots of $C_{ss}(x,t)$ and $C_{ee}(x,t)$ for the integrable LLL model in easy plane regime at high temperature. Parameters are $\rho = 1.0, \beta = 1.0$ and $N = 2048$. The figures show the ballistic scaling of $C_{ss}(x,t)$ and $C_{ee}(x,t)$ at different times.

spreading, in contrast to the sub-ballistic broadening of the two sound peaks in the case of a nonintegrable chain. The form of dynamical correlations in classical integrable models have been discussed in several earlier work including [19, 20] for the Toda chain and in [21] for a particular integrable spin chain, which we will now discuss.

2.2.3 Integrable LLL model

Faddeev and Takhtajan [12] discovered an integrable version of the LLL model, which still has nearest neighbor coupling but is no longer quadratic. Their Hamiltonian is given by

$$H = -\sum_{j=1}^{N} h(\vec{S}_j, \vec{S}_{j+1}) \tag{2.12}$$

with local energy

$$\begin{aligned} h(\vec{S},\vec{S}') = \log\Big|&\cos(\rho S^z)\cos(\rho S'^z) + (\cot(\rho))^2 \sin(\rho S^z)\sin(\rho S'^z) \\ &+(\sin(\rho))^{-2} G(S^z) G(S'^z)(S^x S'^x + S^y S'^y)\Big|, \\ G(x) = \big(1-x^2\big)^{-\frac{1}{2}}&\big(\cos(2\rho x) - \cos(2\rho)\big)^{\frac{1}{2}} \end{aligned} \tag{2.13}$$

with $\rho \geq 0$. The Hamiltonian (2.12) seems to be the only known integrable classical spin chain. Easy plane corresponds to $\rho > 0$, while in the limit $\rho \to 0$ one recovers the isotropic interaction

$$h(\vec{S},\vec{S}') = \log\big(1 + \vec{S}\cdot\vec{S}'\big). \tag{2.14}$$

The infinitely extended Faddeev-Takhtajan spin chain has a countable number of locally conserved fields, which are constructed by successive differentiations of the R-matrix, see [12].

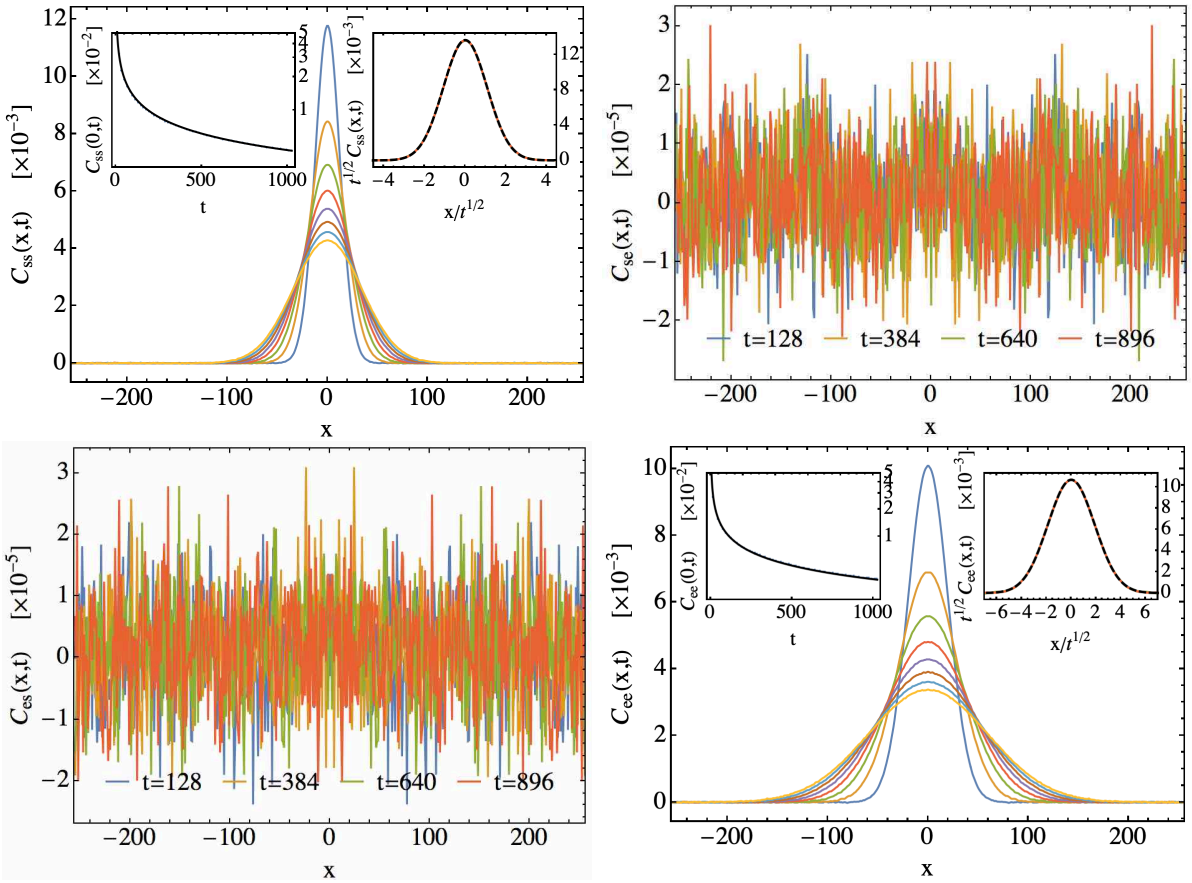

Figure 2.4: Easy axis data $\Delta = 1.5$, $\beta = 0.1$, $N = 512$. We observe perfect diffusive behaviour (see inset).

Here we focus on the z-component of the magnetization, s_j, and the local energy, e_j, as the first items in the list of conservation laws. We display their time-correlations at $\rho = 1$ with inverse temperature $\beta = 1$ and magnetic field $h = 0$, see Fig. (2.2). In the scaling plot Fig. (2.3), we see that the energy and spin correlations show good ballistic scaling already at short times. In [21] simulations of the spin current correlations are reported at parameters $\rho = 1, \beta = 0.25, h = 0$.

Without losing integrability, the Hamiltonian (2.13) can be analytically continued to purely imaginary ρ, which amounts to replace the trigonometric functions by their hyperbolic cousin [12]. Physically this corresponds to easy-axis regime. We refer to the discussions in [21, 22], also reporting on parameters with diffusive spreading.

2.3 Easy plane at low-temperatures

2.3.1 Low-temperature effective hamiltonian:

We now return to the nonintegrable XXZ spin chain. As the temperature is lowered, if we impose easy-axis anisotropy, $\Delta > 1$, the spreading of spin and energy correlations is

still diffusive, as confirmed by further molecular dynamics simulations. In Fig. (2.4) we show the easy axis data. Apparently diffusion still holds at $\Delta = 1$, although with slow convergence [23]. However, for easy-plane, $\Delta < 1$, phase differences become locally almost conserved, which drastically changes the dynamical behavior, as will now be explained in detail. The equations of motion are given by (2.5).

Phase differences are defined through

$$r_j = \phi_{j+1} - \phi_j \ , \quad \mod \ 2\pi, \tag{2.15}$$

where we choose coordinates such that $r_j \in [-\pi, \pi]$. $r_j = 0$ corresponds to $\phi_j = \phi_{j+1}$ which is the minimum of the cosine-potential. The dynamics of the $r_j(t)$'s has the following generic structure. One starts from their extended version with $\tilde{r}_j \in \mathbb{R}$ governed by

$$\tfrac{d}{dt}\tilde{r}_j(t) = g_j(t) - g_{j+1}(t) \tag{2.16}$$

for a given collection of smooth functions $\{g_j(t), j \in \mathbb{Z}\}$. The restriction to the unit circle S^1 is achieved by setting

$$\tilde{r}_j(t) = r_j(t) + 2\pi n_j(t) \tag{2.17}$$

with $n_j(t)$ the integer winding number for bond j; we may choose $n_j(t = 0) = 0$, while $r_j(t)$ is a smooth function on S^1. By construction the $\tilde{r}_j$'s have the form of a local conservation law, which in integrated version reads

$$\sum_j \big(\tilde{r}_j(t) - \tilde{r}_j(0)\big) = \sum_j \int_0^t ds \big(g_j(s) - g_{j+1}(s)\big) = 0, \tag{2.18}$$

for a system with periodic boundary conditions. On the other hand,

$$\sum_j \big(r_j(t) - r_j(0)\big) = -2\pi \sum_j n_j(t) \ . \tag{2.19}$$

Hence $r_j(t)$ is locally conserved only if the total winding number remains constant: $\sum_j n_j(t) = 0$. The dynamical events $r_j(t) = \pm\pi$ are the "phase slip" processes where the winding number changes. Thus the field of phase differences r_j is locally conserved only until the first phase slip event. However, as we show in Fig. (2.5), at low temperatures most phase slip events come in closely-spaced pairs with no change in the total winding number, so the coarse-grained dynamics actually respects this conservation law until one has unpaired phase slip events.

As illustrated in Fig. (2.5a) and (2.5b), for high temperatures there are lots of phase slips. However for easy-plane and low enough temperatures the z-component is approximately constant and the phase difference is trapped by the cosine-potential. Then phase slips are very much suppressed, see Fig. (2.5c) and (2.5d). Therefore, there is an emer-

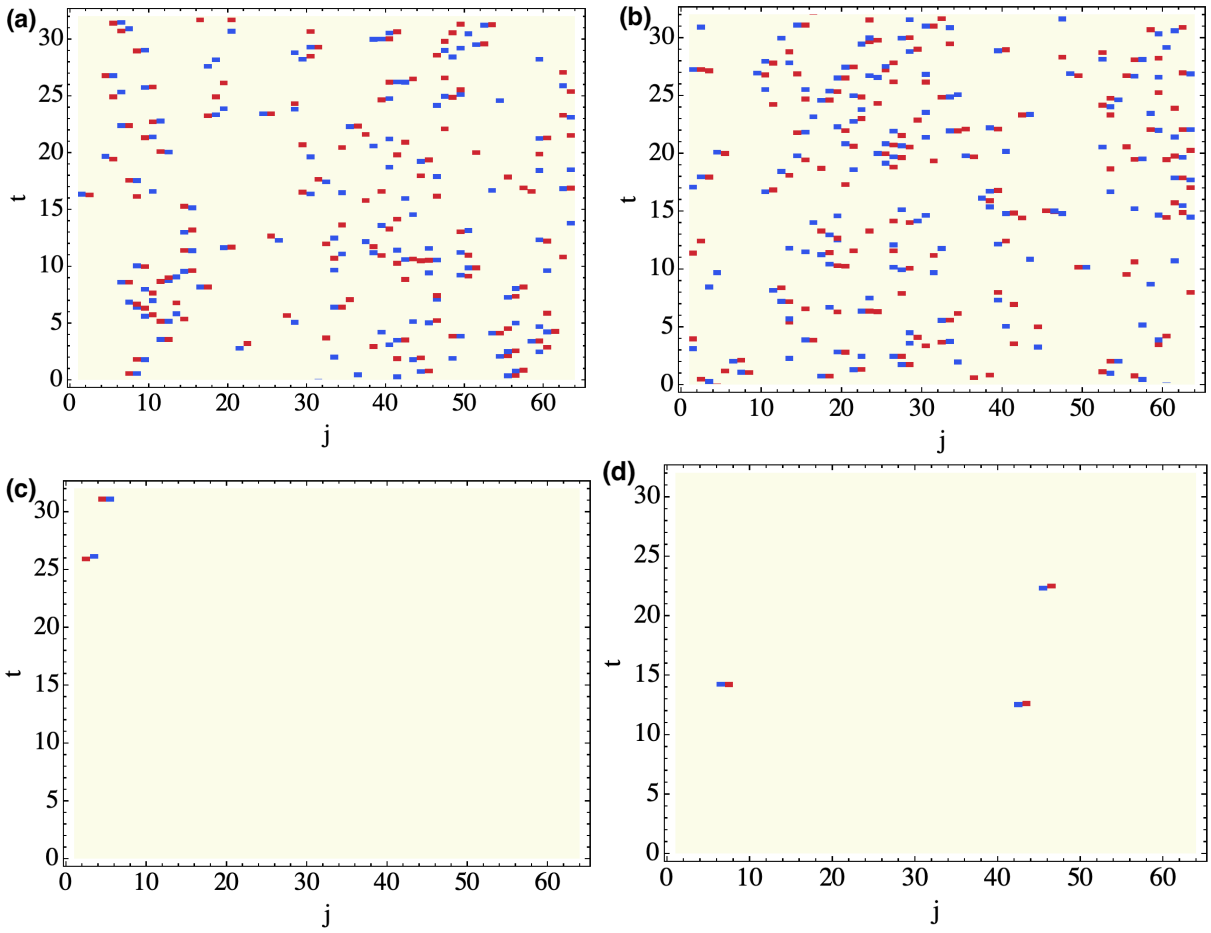

Figure 2.5: (a) Phase slip events at $\beta = 1, h = 0$, (b) $\beta = 1, h = 0.1$, (c) $\beta = 5, h = 0$ and (d) $\beta = 5, h = 0.1$ in easy plane regime with $\Delta = 0.5$. It shows that the phase slip events become rare with decreasing temperature and decreasing external magnetic field. Red (blue) boxes indicate sites where phase slips occur, i.e, δn_j is $+1(-1)$ [Eq. (2.17)].

gence of an approximately conserved quantity. In other words, phase slips are thermally activated process which, in a low-temperature regime, can safely be ignored on the time scales reached by our simulation and, in fact, much longer. Phase differences are thus *approximately conserved* in this regime.

Let us first attempt a rough estimate for the presence of a third conservation law. We assume constant $r_j = r$ and $s_j = s$. Adding also an external field, h, the energy of this configuration equals

$$e_{\mathrm{g}}(r, s) = -(1 - s^2)\cos r - \Delta s^2 - hs. \tag{2.20}$$

Its minimum is located at $r = 0, s = h/[2(1-\Delta)]$ and we require $|h| < 2(1-\Delta)$ to ensure that the minimum lies inside $\{|s| < 1\}$. Let us compute the energy required for a phase slip event caused by motion of a single spin. For the case where s remains fixed but r changes to π, the energy barrier E_{slip} can be easily computed and leads to

$$E_{\mathrm{slip}} = 4\left(1 - \tfrac{1}{4}(1-\Delta)^{-2}h^2\right) > 1 \tag{2.21}$$

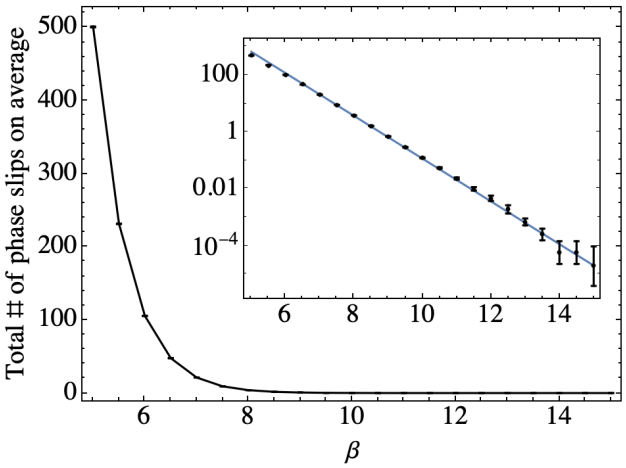

Figure 2.6: The figure illustrates that the average number of phase slip events decays exponentially with β. The parameters are – $h = 0, \Delta = 0.5, N = 1024, t = 512$, 10^5 initial states. Inset shows the same plot in log scale. In log scale the slope is -1.73 which is consistent with our theoretical estimation within error bars.

On the other hand for the case where the angle r remains fixed and the spin moves to the north pole (given by $s = 1$), the energy barrier is

$$E_{\text{slip}} = 2\left(1 - \tfrac{h}{2} - \tfrac{1}{2}(1-\Delta)^{-1}\Delta h\right) \ . \tag{2.22}$$

We expect phase slips to occur at a rate $\sim e^{-\beta \Delta E_{\text{slip}}}$ where β is the inverse temperature, and so $\beta E_{\text{slip}} > 1$ could be a rough criterion for small number of phase-slips and a new approximate conservation law. In Fig. (2.5) we show space-time plots showing phase-slip events seen in simulations at (a) high temperature ($\beta = 1$), zero magnetic field, (b) high temperature ($\beta = 1$), finite magnetic field ($h = 0.3$), (c) low temperature ($\beta = 5$), zero magnetic field and (d) low temperature ($\beta = 5$), finite magnetic field ($h = 0.3$) with parameters $\Delta = 1/2, N = 64$. In Fig. (2.6), we show the dependence of average total number of observed phase slips on the inverse temperature β up to $t = 512$ seen in the low temperature simulations (with parameters $\Delta = 1/2$, $h = 0$). We see that E_{slip} takes the values 4 and 2 from the two energy estimates mentioned above. From the simulations we find the expected activated dependence form, however with a barrier $\Delta E \approx 1.73$. To understand such behavior we have to investigate in more detail the actual process of phase slips. Let us consider the spin chain with zero external magnetic field and in the easy-plane regime ($h = 0, \Delta < 1$). In the ground state all spins are aligned and lying on the xy plane. We are interested in finding the minimum-energy spin configuration in which there is a phase slip. What we find at the lowest temperatures where such phase slip events do happen in our simulations is that the phase slip event is centered on a single spin j that moves out of the xy plane and is very close to either $\theta_j = 0$ or $\theta_j = \pi$. The nearby spins i move to near the configuration of their angles θ_i that minimizes the energy given the special orientation of the one "central" spin j, with all spins except the central one oriented near the same ϕ_i. When we do this minimization for $\Delta = 0.5$ and $h = 0$, the resulting minimum energy of the phase slip event is $E_{\text{slip}} \cong 1.73$ [24]. As expected, the measured density of phase slip events shows a thermally activated

dependence on temperature as $\sim \exp(-\beta E_{\text{slip}})$, as shown in Fig. (2.6). These phase slip events are produced at this low density by the chaotic equilibrium dynamics of the LLL chain.

To work with an almost conserved field is somewhat vague and it is more convenient to modify the dynamics such that $r_j(t)$ is strictly locally conserved. Of course, this is a valid approximation only in a regime with a very low density of phase slips. We rewrite our Hamiltonian in a slightly more general form as

$$H_{\text{lt}} = \sum_{j\in\mathbb{Z}} \big(f(s_j)f(s_{j+1})U(r_j) - \Delta s_j s_{j+1}\big). \tag{2.23}$$

If one would set $U(x) = -\cos(x)$, included to have motion on S^1, then $H_{\text{lt}} = H$. To suppress phase slips entirely we modify $U(x)$ by adding infinitely high potential barriers at $x = \pm\pi$. Then up to the first phase slip event, the dynamics generated by H agrees with the dynamics generated by H_{lt}, but they differ later on. Actually, for what we want to show the precise shape of the potential barriers plays no role, as long as phase slips are forbidden.

2.3.2 Nonlinear fluctuating hydrodynamics (NFH) in the low temperature regime:

As before, the Hamiltonian equations of motions for (2.23) are

$$\tfrac{d}{dt}\phi_j = \partial_{s_j} H_{\text{lt}}, \quad \tfrac{d}{dt}s_j = -\partial_{\phi_j} H_{\text{lt}}. \tag{2.24}$$

The conserved fields are phase difference, spin, and energy,

$$r_j, \quad s_j, \quad e_j = f_j f_{j+1} U_j - \Delta s_j s_{j+1}, \tag{2.25}$$

where for later convenience we introduced the shorthand $f_j = f(s_j)$ and $U_j = U(r_j)$. From the equations of motion we obtain for the current of the phase difference,

$$\mathcal{J}^{\mathsf{r}}_j = -f'_j f_{j+1} U_j - f_{j-1} f'_j U_{j-1} + \Delta(s_{j-1} + s_{j+1}), \tag{2.26}$$

for the spin current,

$$\mathcal{J}^{\mathsf{s}}_j = -f_{j-1} f_j U'_{j-1}, \tag{2.27}$$

and for the energy current,

$$\mathcal{J}^{\mathsf{e}}_j = -f_{j-1} f_j f'_j f_{j+1}\big(U'_{j-1}U_j + U_{j-1}U'_j\big) + \Delta\big(f_{j-1} f_j U'_{j-1} s_{j+1} + f_j f_{j+1} U'_j s_{j-1}\big). \tag{2.28}$$

The grand canonical ensemble of $H_{\rm lt}$ for a finite system with N lattice sites and periodic boundary conditions is given by

$$Z_N(\nu,h,\beta)^{-1}\,\exp\Big[-\beta\Big(H_{\rm lt}-\nu\sum_{j=1}^N r_j-h\sum_{j=1}^N s_j\Big)\Big]\prod_{j=1}^N \mathrm{d}r_j\mathrm{d}s_j \tag{2.29}$$

with the normalizing partition function

$$Z_N(\nu,h,\beta)=\int_{([-1,1]\times[-\pi,\pi])^N}\exp\Big[-\beta\Big(H_{\rm lt}-\nu\sum_{j=1}^N r_j-h\sum_{j=1}^N s_j\Big)\Big]\prod_{j=1}^N \mathrm{d}r_j\mathrm{d}s_j, \tag{2.30}$$

where ν is the "chemical potential" for the additional conserved field r_j. Infinite volume averages with respect to (2.29) are denoted by $\langle\cdot\rangle_{\nu,h,\beta}$. The canonical free energy is defined as

$$F(\nu,h,\beta)=-\beta^{-1}\lim_{N\to\infty}\tfrac{1}{N}\log Z_N(\nu,h,\beta). \tag{2.31}$$

The infinite volume equilibrium averages of r_j, s_j, e_j are

$$\begin{aligned}&\mathsf{r}=\langle r_j\rangle_{\nu,h,\beta}=-\partial_\nu F(\nu,h,\beta),\qquad \mathsf{s}=\langle s_j\rangle_{\nu,h,\beta}=-\partial_h F(\nu,h,\beta),\\ &\mathsf{e}=\langle e_j\rangle_{\nu,h,\beta}=\partial_\beta(\beta\,F(\nu,h,\beta))+\nu\mathsf{r}+h\mathsf{s},\end{aligned} \tag{2.32}$$

independent of j because of translation invariance. By convexity of F, these relations define the inverse mapping $(\mathsf{r},\mathsf{s},\mathsf{e})\mapsto(\nu(\mathsf{r},\mathsf{s},\mathsf{e}),h(\mathsf{r},\mathsf{s},\mathsf{e}),\beta(\mathsf{r},\mathsf{s},\mathsf{e}))$.

Under the constraints (3.8) the LLL equilibrium time-correlations of s_j, e_j should be well approximated by the same time-correlations as computed from the dynamics governed by $H_{\rm lt}$. But $H_{\rm lt}$ is just one particular anharmonic chain and, as explained in [15], the time-correlations can be predicted from nonlinear fluctuating hydrodynamics. We do not repeat here the details, but merely point out that in normal mode representation one arrives at a three-component fluctuating field, $\vec{\phi}(x,t)=\big(\phi_{-1}(x,t),\phi_0(x,t),\phi_1(x,t)\big)$. The Euler currents have to be expanded to second order, which in approximation then leads to the coupled Langevin equations

$$\partial_t\vec{\phi}(x,t)+\partial_x\Big[\mathrm{diag}(-c,0,c)\vec{\phi}+\langle\vec{\phi},\vec{G}\vec{\phi}\rangle-D\partial_x\vec{\phi}+B\vec{\xi}\Big]=0. \tag{2.33}$$

Here D is a constant diffusion matrix and $B\vec{\xi}(x,t)$ is Gaussian white noise, both related through fluctuation-dissipation as $BB^T=2D$. This part of the equation is a phenomenological ansatz for the effective noise and dissipation produced by the deterministic chaos. However the sound speed, c, and the three symmetric coupling matrices $\vec{G}$ have to be computed from the underlying microscopic model. In particular $\vec{G}$ determines the dynamical universality class. Fortunately, for the LLL chain the magic identity (proven

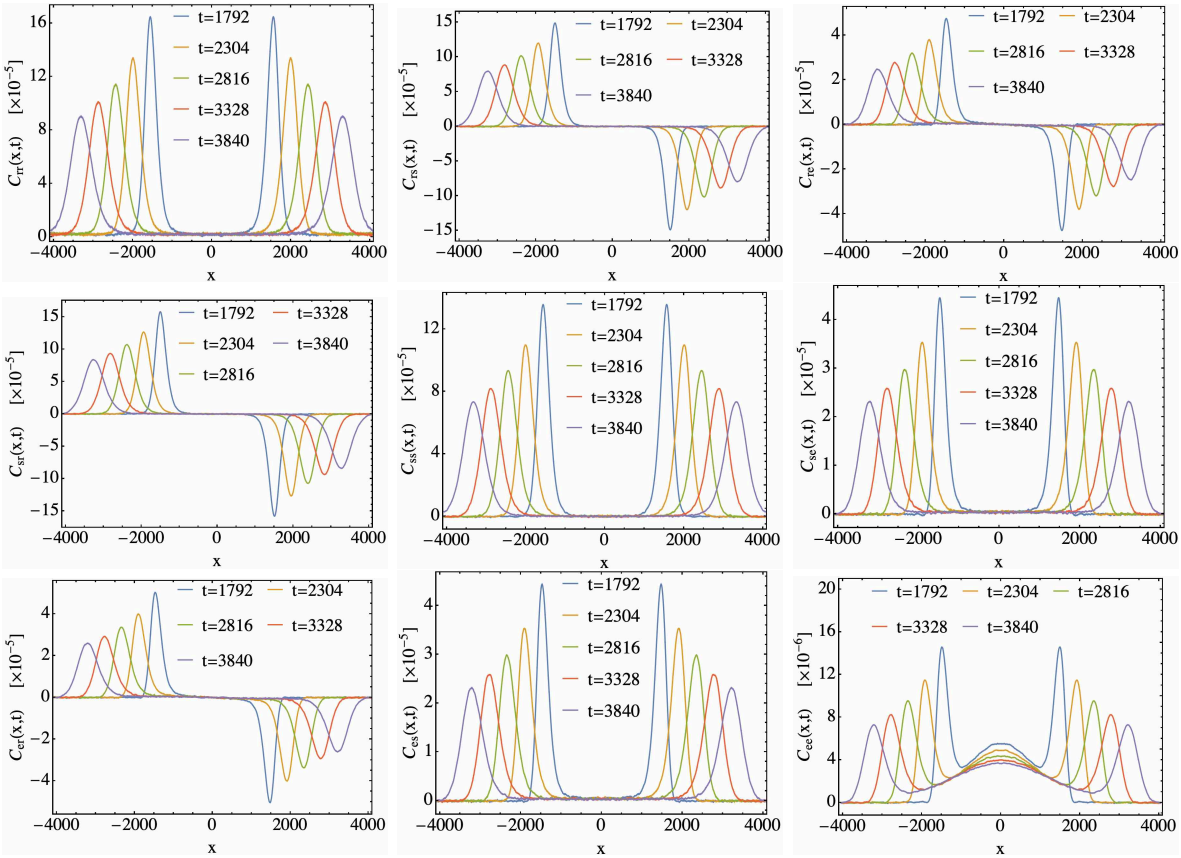

Figure 2.7: Parameters: $\Delta = 0.5, \beta = 10.0, h = 0.3, N = 8192$ – RK-4 with $dt = 0.005$: Plot of $C_{ab}(x,t)$ at different times.

below)

$$\langle \vec{\mathcal{J}}_j \rangle_{\nu,h,\beta} = \langle (\mathcal{J}^{\mathsf{r}}_j, \mathcal{J}^{\mathsf{s}}_j, \mathcal{J}^{\mathsf{e}}_j) \rangle_{\nu,h,\beta} = (-h, -\nu, -h\nu) \tag{2.34}$$

is available. Using this property the precise form of $\vec{G}$ and its relation to second derivatives of the free energy have been established in [15].

We turn to the proof of (2.34).

(i) For the phase difference current we obtain

$$\begin{aligned} \langle \mathcal{J}^{\mathsf{r}}_j \rangle_{\nu,h,\beta} &= \big\langle -f'_j f_{j+1} U_j - f_{j-1} f'_j U_{j-1} + \Delta(s_{j-1} + s_{j+1}) \big\rangle_{\nu,h,\beta} \\ &= \beta^{-1} Z_N^{-1} \int \big(\partial_{s_j} \mathrm{e}^{-\beta H_{\mathrm{lt}}}\big)\big(\mathrm{e}^{\beta\nu \sum_j r_j + \beta h \sum_j s_j}\big) = -h. \end{aligned} \tag{2.35}$$

(ii) Correspondingly, for the spin current we obtain

$$\begin{aligned} \langle \mathcal{J}^{\mathsf{s}}_j \rangle_{\nu,h,\beta} &= -\langle f_{j-1} f_j U'_{j-1} \rangle_{\nu,h,\beta} \\ &= \beta^{-1} Z_N^{-1} \int f_{j-1} f_j \big(\partial_{r_{j-1}} \mathrm{e}^{-\beta H_{\mathrm{lt}}}\big)\big(\mathrm{e}^{\beta\nu \sum_j r_j + \beta h \sum_j s_j}\big) \\ &= -\nu, \end{aligned} \tag{2.36}$$

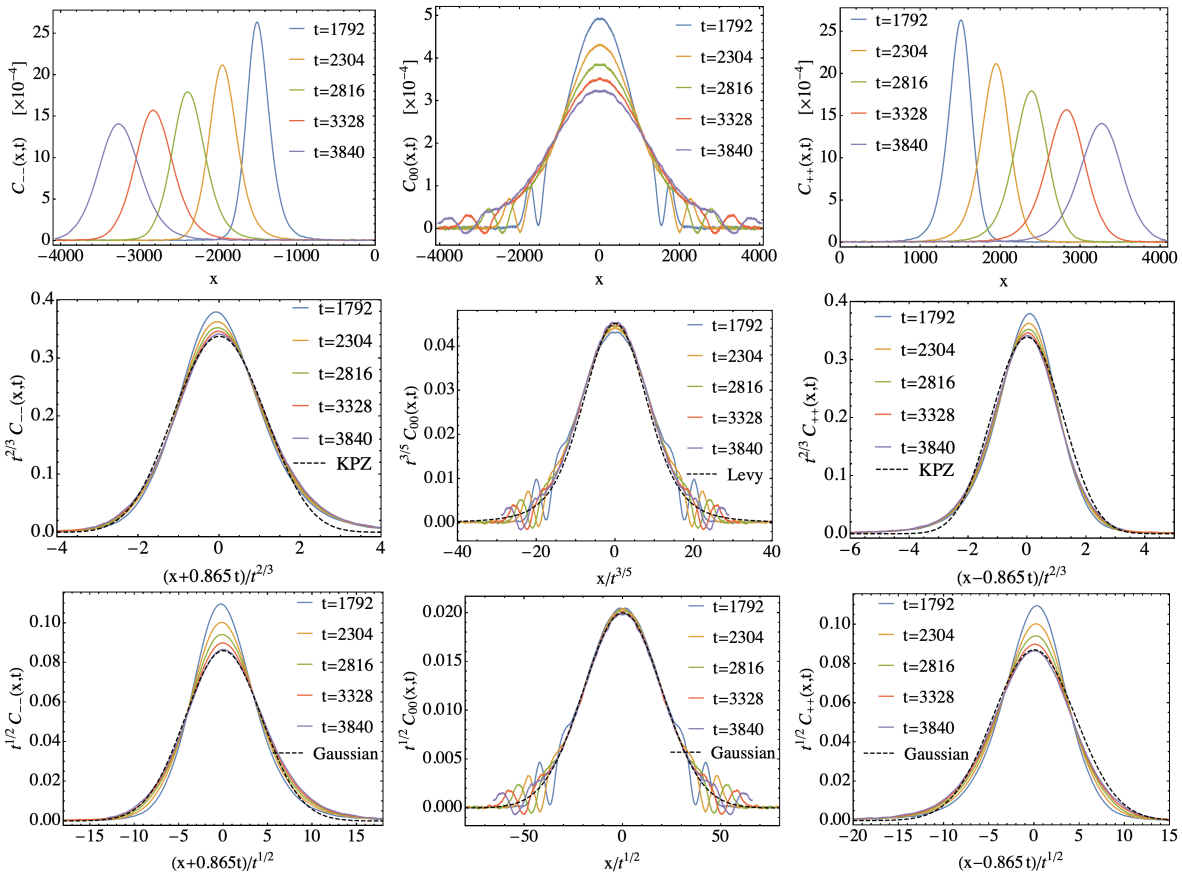

Figure 2.8: Parameters: $\Delta = 0.5, \beta = 10.0, h = 0.3, N = 8192$ – RK4 with $dt = 0.005$: Plot of $C_{++}(x,t)$, $C_{00}(x,t)$ and $C_{--}(x,t)$, obtained after normal mode transformation. The 2nd row shows the sound modes with KPZ scaling and heat mode with the predicted Levy scaling, while the 3rd row shows diffusive scaling of the same data. Sound speed estimate from theory is $c = 0.865$.

where we used partial integration in the last step.

(iii) For the energy current there are more terms to be considered,

$$\begin{aligned}
\langle \mathcal{J}^{\mathrm{e}}_j \rangle_{\nu,h,\beta} &= \big\langle -f_{j-1}f_jf'_jf_{j+1}\big(U'_{j-1}U_j + U_{j-1}U'_j\big) \\
&\qquad + \Delta\big(f_{j-1}f_jU'_{j-1}s_{j+1} + f_jf_{j+1}U'_js_{j-1}\big)\big\rangle_{\nu,h,\beta} \\
&= \beta^{-1}Z_N^{-1}\int \Big[\big(f'_jf_{j+1}U_j - \Delta s_{j+1}\big)\partial_{r_{j-1}}\mathrm{e}^{-\beta H_{\mathrm{lt}}} \\
&\qquad + \big(f_{j-1}f'_jU_{j-1} - \Delta s_{j-1}\big)\partial_{r_j}\mathrm{e}^{-\beta H_{\mathrm{lt}}}\Big]\,\mathrm{e}^{\beta\nu\sum_j r_j + \beta h\sum_j s_j} \\
&= -\nu\, Z_N^{-1}\int \Big[f_{j-1}f'_jU_{j-1} + f'_jf_{j+1}U_j \\
&\qquad - \Delta(s_{j-1}+s_{j+1})\Big]\mathrm{e}^{-\beta(H_{\mathrm{lt}} - \nu\sum_j r_j - h\sum_j s_j)} \\
&= -h\nu. \qquad (2.37)
\end{aligned}$$

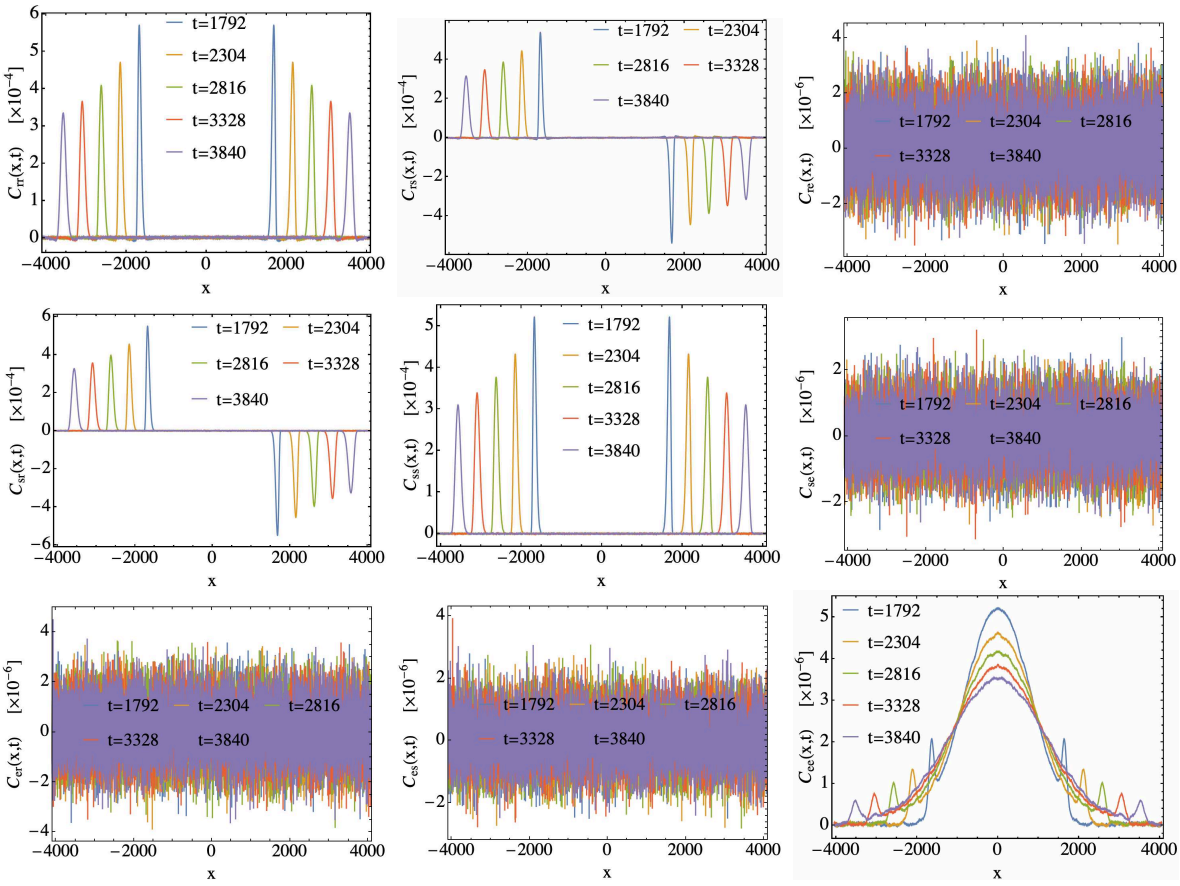

Figure 2.9: Parameters: $\Delta = 0.5, \beta = 10.0, h = 0, N = 8192$ – RK-4 with $dt = 0.005$: Plot of $C_{ab}(x,t)$ at different times. $C_{es}(x,t)$, $C_{se}(x,t)$, $C_{re}(x,t)$ and $C_{er}(x,t)$ are essentially zero, which is expected from symmetry.

We conclude that the H_{lt}-currents satisfy (2.34) independently of U, provided U diverges sufficiently fast at the two border points so as to have the boundary terms vanish.

When applying the magic identity, the potential U is specified as the cosine with infinitely high barriers added at $x = \pm\pi$. This does not change the free energy. Thus at the end the coupling matrix $\vec{G}$ is given in terms of the LLL free energy. We refer to Appendix A for more details. The chemical potential ν is not a physical control parameter that we will explore. It is needed in the second order expansion, but will be set to $\nu = 0$ afterwards.

2.4 Numerical results at low temperature

We now present numerical results for the dynamical correlations for two cases with (I) finite magnetic field and (II) zero field, at inverse temperature $\beta = 10$. Apart from the

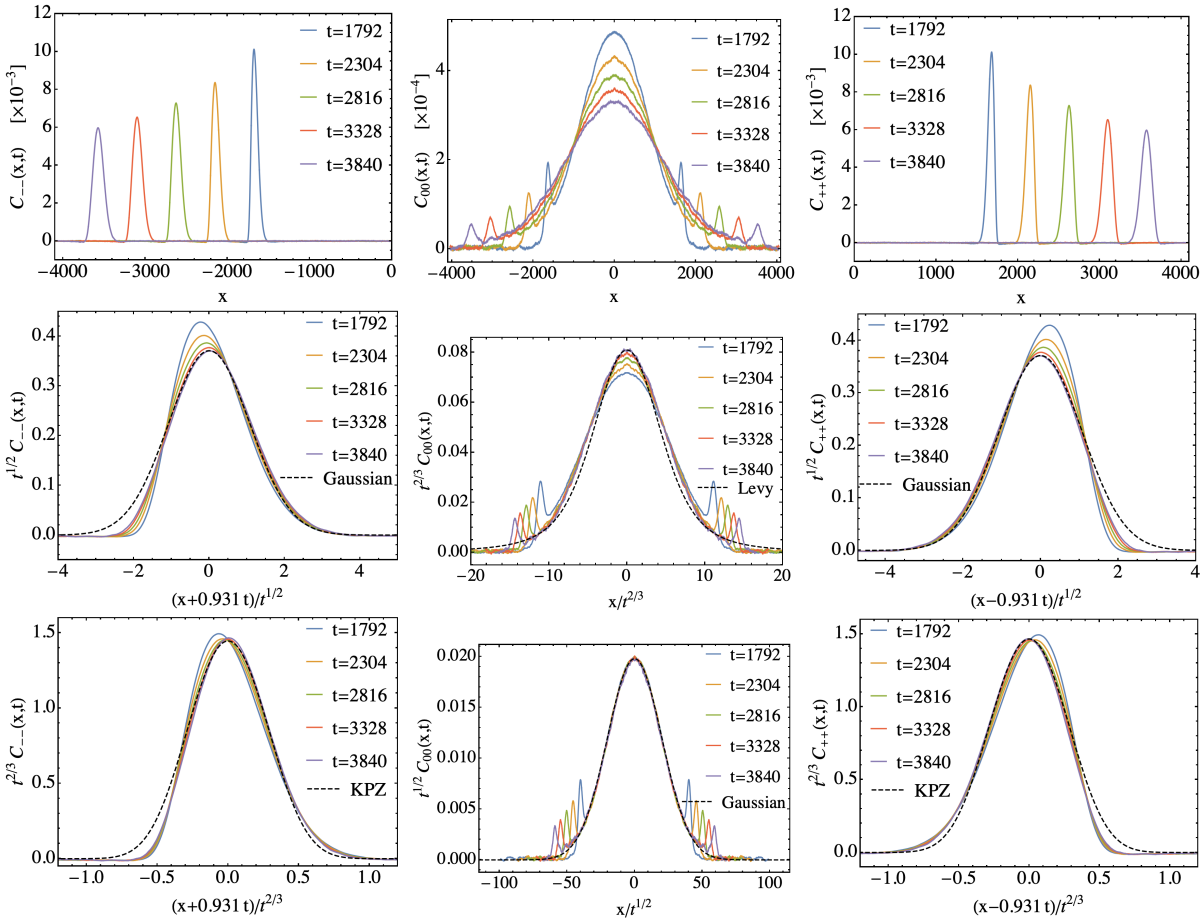

Figure 2.10: Parameters: $\Delta = 0.5, \beta = 10.0, h = 0, N = 8192$ – RK-4 with $dt = 0.005$: Plot of $C_{--}(x,t)$, $C_{00}(x,t)$ and $C_{++}(x,t)$, obtained after normal mode transformation. The 2nd row shows the diffusive scaling of both the sound modes and the heat mode with Levy scaling, while the 3rd row shows the same data with KPZ scaling of sound modes and diffusive scaling of the heat mode. Sound speed estimate from theory is $c = 0.931$.

spin and energy correlations defined in Eq. (2.38) we now measure

$$C_{\rm rr}(j,t) = \langle r_j(t) r_0(0) \rangle^{\rm c}_{\beta,h}, \tag{2.38}$$

corresponding to the extra conserved variable. We also compute the normal mode correlations $C_{\sigma,\sigma'}$, where $\sigma, \sigma' = +1, 0, -1$ correspond to the modes $\phi_{+1}, \phi_0, \phi_{-1}$ respectively.

2.4.1 Simulation details

In the simulations we first generated equilibrium configurations corresponding to the canonical distribution, specified by β, h, using a Metropolis Monte Carlo algorithm. The equilibrated configuration was then evolved with our Hamiltonian dynamics using either a fixed step size and sometimes an adaptive step size 4th order Runge-Kutta (RK4) integrator. This maintains the global conservations (total energy and magnetization) up to an absolute deviation of $\sim 10^{-6}$ and $\sim 10^{-13}$ respectively until the final time of

Table 2.1: G matrices ($\beta = 10,\ h = 0.3,\ \nu = 0$)

G matrix	MD simulation	NFH
G^-	$\begin{bmatrix} 0.0355 & -0.411 & 0.0117 \\ -0.411 & -3.961\text{E-}5 & 5.238\text{E-}7 \\ 0.0118 & -7.658\text{E-}5 & -0.0118 \end{bmatrix}$	$\begin{bmatrix} 0.03536 & -0.4079 & 0.01179 \\ -0.4079 & 0 & 0 \\ 0.01179 & 0 & -0.01179 \end{bmatrix}$
G^0	$\begin{bmatrix} -0.411 & -2.989\text{E-}16 & -3.828\text{E-}5 \\ -3.961\text{E-}5 & 2.057\text{E-}20 & 2.104\text{E-}5 \\ -3.829\text{E-}5 & 3.118\text{E-}16 & 0.411 \end{bmatrix}$	$\begin{bmatrix} -0.4079 & 0 & 0 \\ 0 & 0 & 0 \\ 0 & 0 & 0.4079 \end{bmatrix}$
G^+	$\begin{bmatrix} 0.0118 & -7.657\text{E-}5 & -0.0118 \\ 5.280\text{E-}7 & 2.104\text{E-}5 & 0.411 \\ -0.0118 & 0.411 & -0.0352 \end{bmatrix}$	$\begin{bmatrix} 0.01179 & 0 & -0.01179 \\ 0 & 0 & 0.4079 \\ -0.01179 & 0.4079 & -0.03536 \end{bmatrix}$
speed of sound c	0.865 (maxima of the sound peaks) 0.859 (normal mode transformation)	0.85217

evolution. Individual spin lengths are also conserved up to $\sim 10^{-13}$. Averages were compute over around 10^6 initial conditions.

In all our simulations we fixed $\beta = 10$. At much smaller temperatures, phase slips would be even rarer but the dynamics of small fluctuations about the ordered state is expected to be closer to integrable, and the time required to see the asymptotic scaling becomes inaccessible.

2.4.2 Case-I ($\nu = 0,\ h = 0.3$)

In this regime we expect to confirm the KPZ sound modes and Levy heat modes as predicted by NFH. We have chosen thing parameters: $\Delta = 0.5,\ \beta = 10.0,\ N = 8192$. The z-component of the total spin, energy, and individual spin length are conserved up to 10^{-15} and 10^{-5} and 10^{-10} respectively. Phase Slip processes are rare but not completely absent. In Fig. (2.7), the correlations $C_{\alpha\beta}(x,t)$ are plotted at different times.

In Fig. (2.8), we plot the sound and heat modes obtained after normal mode transformations and with different scalings. Values of the G-matrices are given in Table-2.1.

As for anharmonic chains, $G^0_{00} = 0$ which implies that the self-coupling term is absent for the heat mode. Also $G^\sigma_{\sigma\sigma}$ ($\sigma = \pm 1$) are non-zero which in the context of NFH is the

Table 2.2: G matrices ($\beta = 10,\ h = 0,\ \nu = 0$)

G matrix	MD simulation	NFH
G^-	$\begin{bmatrix} 6.655\text{E-}6 & -0.4494 & 1.520\text{E-}4 \\ -0.4494 & -3.415\text{E-}5 & 1.080\text{E-}8 \\ 1.768\text{E-}4 & -6.453\text{E-}5 & -1.358\text{E-}5 \end{bmatrix}$	$\begin{bmatrix} 0 & -0.4488 & 0 \\ -0.4488 & 0 & 0 \\ 0 & 0 & 0 \end{bmatrix}$
G^0	$\begin{bmatrix} -0.4494 & 3.275\text{E-}20 & -3.227\text{E-}5 \\ -3.415\text{E-}5 & 0. & 2.480\text{E-}5 \\ -3.226\text{E-}5 & 6.551\text{E-}20 & 0.4494 \end{bmatrix}$	$\begin{bmatrix} -0.4488 & 0 & 0 \\ 0 & 0 & 0 \\ 0 & 0 & 0.4488 \end{bmatrix}$
G^+	$\begin{bmatrix} 1.768\text{E-}4 & -6.453\text{E-}5 & -1.355\text{E-}5 \\ 1.457\text{E-}8 & 2.480\text{E-}5 & 0.4494 \\ 2.055\text{E-}5 & 0.4494 & -5.058\text{E-}4 \end{bmatrix}$	$\begin{bmatrix} 0 & 0 & 0 \\ 0 & 0 & 0.4488 \\ 0 & 0.4488 & 0 \end{bmatrix}$
speed of sound c	0.931 (maxima of the sound peaks) 0.930 (normal mode transformation)	0.92837

crucial property for the KPZ scaling of sound modes and Levy-5/3 scaling of heat mode:

$$C_{\sigma\sigma}(x,t) \sim \frac{1}{(\lambda_s t)^{2/3}} f_{\rm KPZ}\left[\frac{x - c\sigma t}{(\lambda_s t)^{2/3}}\right], \tag{2.39}$$

$$C_{00}(x,t) \sim \frac{1}{(\lambda_h t)^{3/5}} f^{5/3}_{\rm Levy}\left[\frac{x}{(\lambda_h t)^{3/5}}\right], \tag{2.40}$$

where $f^{\alpha}_{\rm Levy}(x) = \text{InverseFourier}\left[e^{-|k|^{\alpha}}\right] \sim \frac{1}{\pi}\frac{1}{|x|^{\alpha+1}}$ and the universal $f_{\rm KPZ}$ function is tabulated in [36].

From the results of our simulations, shown in Fig. (2.8), we find that the sound mode is better described by a KPZ-type scaling while the heat mode appears to be closer to diffusive than the expected Levy-5/3. The sound speed from the simulations is $c \approx 0.865$ which is close to the theoretical estimate $c = 0.85217$.

2.4.3 Case-II ($\nu = 0,\ h = 0$)

In this regime, the r- interaction potential is symmetric under reflection. This leads to a distinct universality class. On the basis of NFH the sound modes are expected to be diffusive and the heat mode to be Levy-3/2. We have chosen the following parameters: $\Delta = 0.5,\ \beta = 10.0,\ N = 8192$. Phase Slip events are absent in this regime. The z-component of the spin, energy, and individual spin length are conserved up to 10^{-12}

and 10^{-5} and 10^{-10} respectively. In Fig. (2.9), the correlations $C_{\alpha\beta}(x,t)$ are plotted at different times. In Figs. (2.10), we plot the sound and heat modes obtained after normal mode transformations and with different scalings. The G-matrices are given in Table-2.2.

We have $G^0_{00} = 0$ here as well. Unlike the previous case $G^\sigma_{\sigma\sigma}$ ($\sigma = \pm 1$) are *zero* which gives rise to diffusive sound mode and Levy-3/2 heat mode in NFH:

$$C_{\sigma\sigma}(x,t) \sim \frac{1}{(\lambda_s t)^{1/2}} \exp\left[\frac{(x - c\sigma t)^2}{\lambda_s t}\right], \tag{2.41}$$

$$C_{00}(x,t) \sim \frac{1}{(\lambda_h t)^{2/3}} f^{3/2}_{\text{Levy}}\left[\frac{x}{(\lambda_h t)^{2/3}}\right], \tag{2.42}$$

As mentioned earlier the expectation from theory is that the sound modes are diffusive while the heat mode is Levy-3/2. However, as can be seen from our simulations, i.e. Fig. (2.10), these scalings are not seen conclusively. The sound speed from the simulations is $c \approx 0.931$ which agrees well with the theoretical estimate $c = 0.92837$.

2.5 Discrete time LLL dynamics

In this section we discuss a discrete version of the lattice Landau-Lifshitz equations, using an integration algorithm that explicitly preserves the total angular momentum and the total energy of the system to machine precision independent of the time step used in the numerical integration, while allowing a bounded error in the fixed-length constraint on each classical spin (in the anisotropic case with $\Delta \neq 1$, it is of course only the z component of the angular momentum which is thus conserved). As will be apparent from the description below, the smallness of the violation of the fixed-length constraint for each spin is controlled by the size of the time-step used in the numerical integration. Additionally, this error does not grow with the total time over which the system is evolved. Since all our general arguments and theoretical analysis rely heavily on the existence of a conserved energy and angular momentum density, and the fixed-length constraint on each individual classical spin does not play a similar central role in the theoretical analysis, our procedure allows us to use relatively large time-steps while preserving the universality class of the dynamics to machine precision.

Our procedure may be viewed as a modification of the so-called "odd-even dynamics" that has been employed previously in the literature [26]. In the odd-even decomposition, one splits the time-evolution into two steps, one of which sets in motion all the odd spins, allowing them to precess in the exchange field supplied by the (temporarily) static even spins, while the other step reverses the role of even and odd spins to evolve the even spins. Below we refer to these individual steps as odd and even precessions.

Our modification is suggested by a particular approximation (the Cayley approximation) to the evolution operators that implement these even or odd precessions over a small

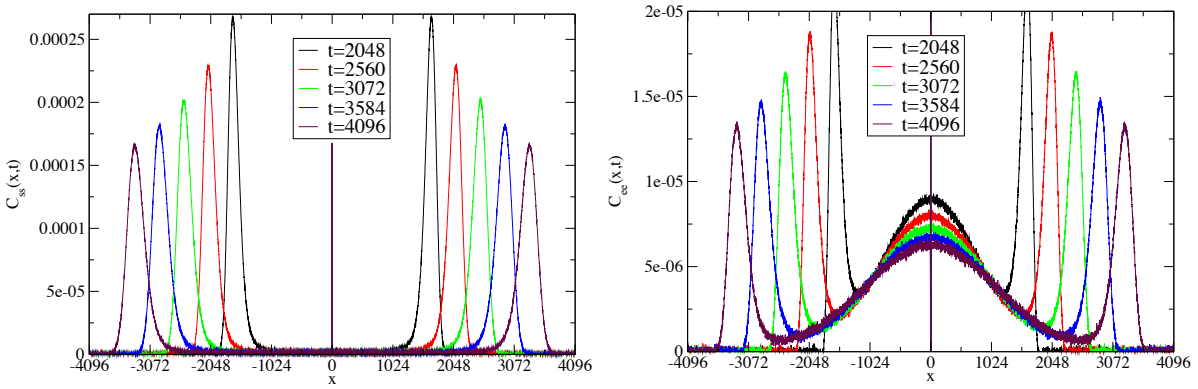

Figure 2.11: Results from discrete dynamics with $dt = 1.0$: Plot of $C_{ss}(x,t)$ and $C_{ee}(x,t)$ for parameters $\beta = 8.0, h = 0.3, N = 8192$ at five different times. Note that there is a spurious peak, constant in time, which is an artifact of the discrete dynamics and goes away in the limit $dt \to 0$, however this does not affect the properties of the relevant remaining part of the correlation functions.

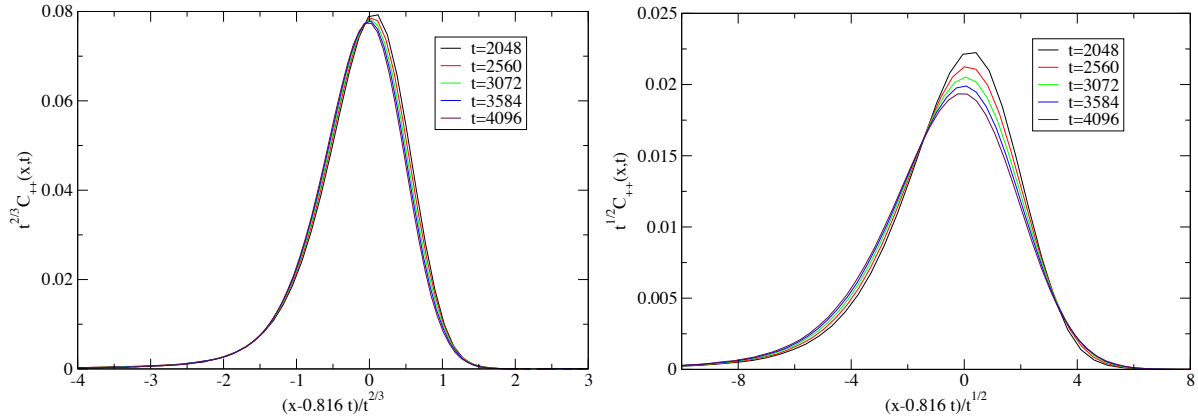

Figure 2.12: Results from discrete dynamics with $dt = 1.0$: Plot of $C_{++}(x,t)$, obtained after normal mode transformation, with KPZ and diffusive scaling respectively, for parameters $\beta = 8.0, h = 0.3, N = 8192$, at five different times. Sound estimate from theory is $c = 0.809$.

time δ in a way that preserves the orthogonal nature of the evolution operator. Consider Eqn. (2.2) with j odd and all B_j held fixed (by keeping all even spins fixed). With all B_j fixed, the right hand side is a B_j dependent rotation of all the odd spins. Let us denote the corresponding linear operator by $R_o(B_e)$ (where o stands for odd and the subscript e on B reminds us that B depends on the current configuration of all even spins, held fixed for the duration of this step). Here R_o and R_e are antisymmetric matrices that serve as the generators of the corresponding rotations. The odd spins after a time δ can be obtained by applying the operator $\exp(\delta R_o)$ to the initial configuration of odd spins.

We begin with the Cayley approximation to individual precessions,

$$\exp(\delta R_o) \approx (1 - \frac{\delta}{2} R_o)^{-1} (1 + \frac{\delta}{2} R_o), \tag{2.43}$$

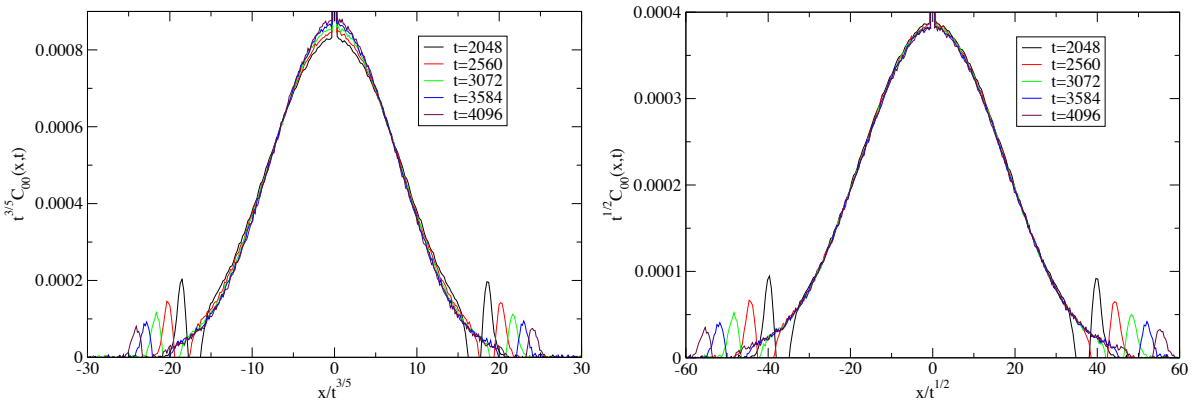

Figure 2.13: Results from discrete dynamics with $dt = 1.0$: Plot of $C_{00}(x,t)$, obtained after normal mode transformation, with Levy-5/3 and diffusive scaling respectively for parameters $\beta = 8.0, h = 0.3, N = 8192$, at five different times.

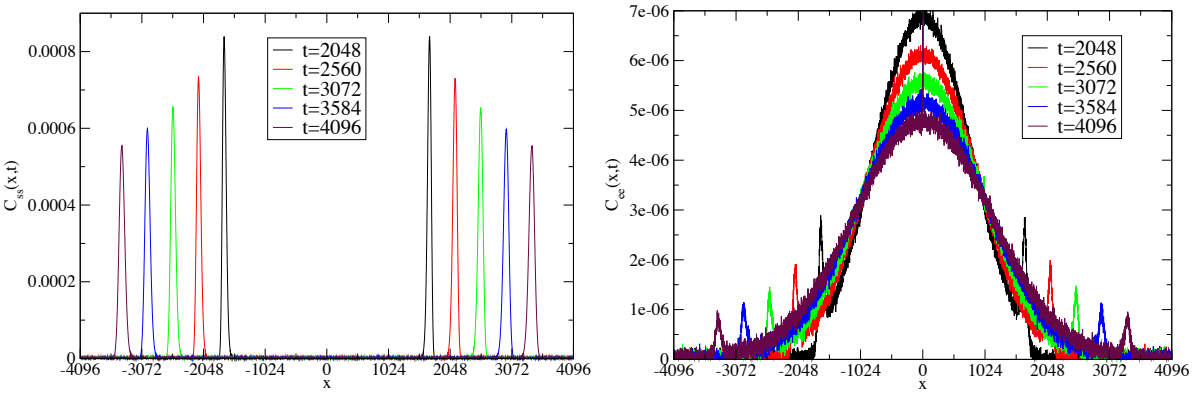

Figure 2.14: Results from discrete dynamics with $dt = 1.0$: Plot of $C_{ss}(x,t)$ and $C_{ee}(x,t)$ for parameters $\beta = 8.0, h = 0.0, N = 8192$ at five different times.

and similarly for R_e. With this in hand, we define the operator

$$O_1 = \left[1 + \frac{\delta}{2} R_e(B_o)\right] \left[1 - \frac{\delta}{2} R_o(B_e)\right]^{-1}. \tag{2.44}$$

Here, we have explicitly displayed the dependence of R_o (R_e) on B_e (B_o) in the configuration on which the operator acts. Let us schematically denote the configuration of odd spins after the action of the first term by $S_o^{1/2}$. The second term is a first order approximation to the precession of even spins in the exchange field provided by $S_o^{1/2}$, starting with the initial configuration of even spins, denoted schematically by S_e^0. Now, the first term amounts to precessing odd spins backwards in time (again using the same first order approximation), using the exchange field provided by the configuration S_e^0, but starting with the configuration $S_o^{1/2}$ in order to end up finally with the initial configuration S_o^0 of the odd spins.

As a result, it is easy to see that O_1 explicitly preserves both the total angular momentum (only the z component of the angular momentum if $\Delta \neq 1$) and the total energy

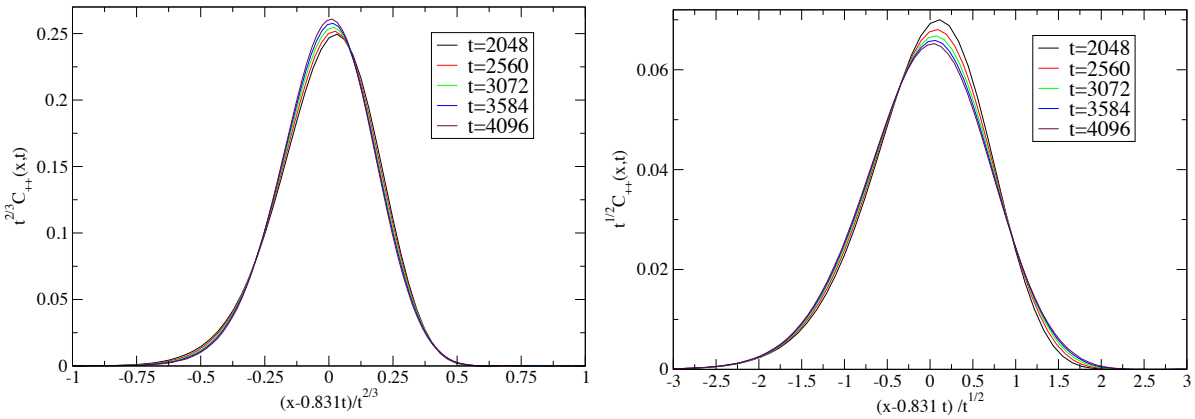

Figure 2.15: Results from discrete dynamics with $dt = 1.0$: Plot of $C_{++}(x,t)$, obtained after normal mode transformation, with KPZ and diffusive scaling respectively, for parameters $\beta = 8.0, h = 0.0, N = 8192$, at five different times. Sound estimate from theory is $c = 0.906$.

of the system, independently of the value of δ. However, O_1 is not orthogonal. O_2 defined as

$$O_2 = \left[1 + \frac{\delta}{2} R_o(B_e)\right] \left[1 - \frac{\delta}{2} R_e(B_o)\right]^{-1} \tag{2.45}$$

has the same properties.

Next we note that the product $O_2 O_1$ provides a second order accurate (in δ) approximation to the actual spin dynamics. This approximation preserves the total angular momentum and total energy independently of δ, while preserving the fixed-length constraint on each spin only to second order. Additionally, our numerical tests reveal that the violation of the fixed length constraint does not grow with total time of integration if each time step is implemented by the operator $O_2 O_1$, even for relatively large values of δ.

Therefore, we integrate the lattice Landau Lifshitz equations using $O_2 O_1$ to evolve the system over one time step. As noted earlier, this can be viewed as a modification of the standard odd-even dynamics used earlier.

We display our results from discrete time dynamics with $dt = 1$.

2.5.1 Case-III ($\beta = 8.0, h = 0.3, N = 8192$)

In Fig. (2.11), we show plots for evolution of the correlations $C_{ss}(x,t)$ and $C_{ee}(x,t)$, while in Figs. (2.12,2.13) we plot the sound mode and heat modes after appropriate translation and with different scalings. As with the continuous time dynamics, in Fig. (2.8), we find again that the sound mode is better described by a KPZ-type scaling while the heat mode appears to be closer to diffusive than the expected Levy-5/3. The sound speed from the simulations is $c \approx 0.816$ which is close to the theoretical estimate $c = 0.809$.

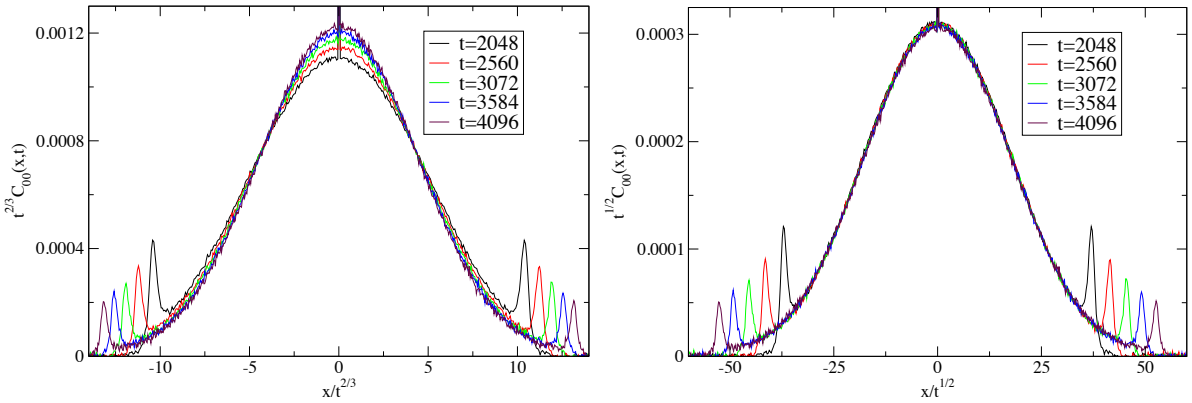

Figure 2.16: Results from discrete dynamics with $dt = 1.0$: Plot of $C_{00}(x,t)$, obtained after normal mode transformation, with Levy-3/2 and diffusive scaling respectively for parameters $\beta = 8.0, h = 0.0, N = 8192$, at five different times.

2.5.2 Case-IV ($\boldsymbol{\beta = 8.0, h = 0.0, N = 8192}$)

In Fig. (2.14), we show plots for evolution of the correlations $C_{ss}(x,t)$ and $C_{ee}(x,t)$, while in Figs. (2.15,2.16) we plot the sound mode and heat modes after appropriate translation and with different scalings. In this case the expectation from theory is that the sound modes are diffusive while the heat mode is Levy-3/2. However, as can be seen in Figs. (2.15,2.16), these scalings are not seen conclusively in the simulations. The sound speed from the simulations is $c \approx 0.831$. Note that, in contrast to the continuous time model, we do not have a simple construction of the stationary equilibrium state. Hence even for the sound speed we do not have a reliable prediction.

2.6 Summary

In this work we have mainly studied the classical XXZ or LLL model and an integrable counterpart of it in easy-plane regimes. We are mostly concerned with the basic conserved quantities — energy and magnetization in both models (integrable and non-integrable) at different regimes of model parameters and external parameters like temperature and magnetic field. For the LLL model, being non-integrable, these two are the only known conserved quantities but at low temperature a third almost conserved quantity emerges, producing sound modes. We have put this into the framework of NFH to get some predictions about the dynamical scaling. We have shown that the non-integrable XXZ chain in the easy-plane regime displays diffusive behaviour at high temperatures, and sound modes with KPZ broadening at low temperatures. The integrable spin chain however demonstrates ballistic behaviour in the easy plane regime. We also find that at high temperature the easy-axis nonintegrable case gives us perfectly diffusive behavior. Our various results are summarized in Table 3.1. For the heat mode, while NFH predicts anomalous Levy broadening, we have not been able to clearly observe this yet in the

simulations. It is possible that one requires larger system sizes and longer times to observe this and further studies are necessary. Similar problems related to non-observation of the expected asymptotic behaviour, due to possible finite size or finite time effects, have been reported in other recent transport studies[27–31], and understanding their origins is an open problem.

Table 2.3: Summary of the transport properties observed in this work.

Model and the parameter regime	**Observation**
(Non-integrable LLL chain)	
Easy plane at high T	Diffusive spin and energy peaks, no sound modes
Easy plane at low T and $h = 0$	Diffusive sound modes* and Levy-3/2 heat mode*
Easy plane at low T and small h	KPZ sound modes and Levy-5/3 heat mode*
Easy axis at high T	Diffusive spin and energy peaks, no sound modes
(Integrable LLL chain)	
Easy plane at high T	Ballistic spin and energy peaks

* Our results for these cases are not entirely conclusive.

Appendices

2.A Coupling coefficients for nonlinear fluctuating hydrodynamics

Given the magic identity (2.34), one can follow [15] to obtain the couplings of the quadratic nonlinearities of NFH. Our simulations are for $\nu = 0$. Restricting to this case, the averages below, denoted by $\langle\cdot\rangle$, $\langle\cdot;\cdot\rangle$, $\langle\cdot;\cdot\rangle$, refer to fixed h, β at $\nu = 0$. One obtains

$$G^0 = \frac{c_s}{2\beta}\,\langle e_0 - h\,s_0; e_0 - h\,s_0\rangle^{-1/2} \begin{pmatrix} -1 & 0 & 0 \\ 0 & 0 & 0 \\ 0 & 0 & 1 \end{pmatrix} \tag{2.46}$$

and

$$G^+ = \frac{c_s}{2\beta}\,\langle e_0 - h\,s_0; e_0 - h\,s_0\rangle^{-1/2} \left[\Upsilon \begin{pmatrix} -1 & 0 & 1 \\ 0 & 0 & 0 \\ 1 & 0 & 3 \end{pmatrix} + \begin{pmatrix} 0 & 0 & 0 \\ 0 & 0 & 1 \\ 0 & 1 & 0 \end{pmatrix}\right], \quad G^- = -(G^+)^{\mathcal{T}}. \tag{2.47}$$

Here c_s denotes the speed of sound determined through

$$c_s = \frac{1}{\beta}\,(\Gamma\langle r_0; r_0\rangle)^{-1/2}\,\langle e_0 - h\,s_0; e_0 - h\,s_0\rangle^{1/2}, \tag{2.48}$$

where $\Gamma = \langle s_0; s_0\rangle\langle e_0; e_0\rangle - \langle s_0; e_0\rangle^2$ and we have introduced the shorthand notation

$$\langle f_0; g_0\rangle = \sum_{j=1}^{N}\langle f_j; g_0\rangle \tag{2.49}$$

with $\langle f; g\rangle = \langle fg\rangle - \langle f\rangle\langle g\rangle$ denoting the second cumulant. Also $^{\mathcal{T}}$ denotes the transpose relative to the anti-diagonal and

$$\Upsilon = -\langle s_0; e_0 - h\,s_0\rangle(2\Gamma)^{-1/2}. \tag{2.50}$$

The thermodynamic averages and cumulants can be obtained as appropriate deriva-

tives of the free energy $F(h,\nu,\beta)$ defined in (2.31) with ν-derivative at $\nu = 0$,

$$\begin{aligned} \langle\!\langle r_0; r_0 \rangle\!\rangle &= -\beta^{-1}\,\partial_\nu^2 F, & \langle\!\langle s_0; s_0 \rangle\!\rangle &= -\beta^{-1}\,\partial_h^2 F, \\ \langle\!\langle e_0 - h\,s_0; e_0 - h\,s_0 \rangle\!\rangle &= -\partial_\beta^2\,(\beta F), & \langle\!\langle s_0; e_0 - h\,s_0 \rangle\!\rangle &= \partial_\beta \partial_h F\,. \end{aligned} \tag{2.51}$$

As second order Taylor coefficients, the G-matrices are symmetric.

The free energy has to be numerically evaluated. An efficient method is to use transfer operator techniques [15]. Inserting our simulation parameters yields (rounded to 4 digits):

$\Delta = 0.5$, $\beta = 10$, $h = 0.3$, speed of sound $c_\mathrm{s} = 0.85217$,

$$G^+ = \begin{pmatrix} 0.01179 & 0 & -0.01179 \\ 0 & 0 & 0.4079 \\ -0.01179 & 0.4079 & -0.03536 \end{pmatrix}, \qquad G^0 = \begin{pmatrix} -0.4079 & 0 & 0 \\ 0 & 0 & 0 \\ 0 & 0 & 0.4079 \end{pmatrix}. \tag{2.52}$$

$\Delta = 0.5$, $\beta = 10$, $h = 0$, speed of sound $c_\mathrm{s} = 0.92837$,

$$G^+ = \begin{pmatrix} 0 & 0 & 0 \\ 0 & 0 & 0.4488 \\ 0 & 0.4488 & 0 \end{pmatrix}, \qquad G^0 = \begin{pmatrix} -0.4488 & 0 & 0 \\ 0 & 0 & 0 \\ 0 & 0 & 0.4488 \end{pmatrix}. \tag{2.53}$$

In Table-2.1 and 2.2 these results are compared with data coming from molecular dynamics.

2.B Low temperature approximation

It is instructive to work out the prefactors of G-matrices (2.46), (2.47) in the harmonic approximation. In principle, also the next order correction could be computed, compare with [15]. We start from the hamiltonian

$$H = \sum_{j=-N/2}^{N/2-1} \left[-\sqrt{1-s_j^2}\sqrt{1-s_{j+1}^2}\cos(r_j) - \Delta s_j s_{j+1} - h s_j \right] \tag{2.54}$$

with $s_j \in [-1,1]$, phase difference $r_j = \phi_{j+1} - \phi_j$, and external field h.

The minimum of H is assumed for $r_j = 0$ and $s_j = \frac{h}{2(1-\Delta)}$ for all j. We expand H in a Taylor series around this minimum and set $t_j = s_j - \frac{h}{2(1-\Delta)}$. Neglecting boundary terms one obtains

$$H = N e_{\mathrm{g}} + H_0 + V + \dots \tag{2.55}$$

with the ground state energy $e_{\mathrm{g}} = -1 - \frac{h^2}{4(1-\Delta)}$, the quadratic contribution

$$H_0 = \frac{1}{2}\sum_j \left[a\, t_j^2 - \tfrac{1}{2} b\, t_j (t_{j-1} + t_{j+1}) + c\, r_j^2 \right], \tag{2.56}$$

and the cubic correction

$$V = \frac{h}{4(1-\Delta)} \sum_j \left[\frac{1}{c^2} t_j^2 \left(-t_{j-1} + 2t_j - t_{j+1} \right) - r_j^2 \left(t_j + t_{j+1} \right) \right]. \tag{2.57}$$

Here we introduced the shorthands

$$a = \frac{2}{c}, \quad b = a - 2(1-\Delta), \quad c = 1 - \left(\frac{h}{2(1-\Delta)} \right)^2. \tag{2.58}$$

We write $H_0 = \frac{1}{2}\langle x, Ax \rangle$ with $x = (t_{-N/2}, \dots, t_{N/2-1}, r_{-N/2}, \dots, r_{N/2-1}) \in \mathbb{R}^{2N}$ and a block-diagonal matrix A consisting of two blocks A_t and $A_r = c\mathbb{I}_N$, with tridiagonal

$$A_t = \begin{pmatrix} a & -\frac{b}{2} & & & \\ -\frac{b}{2} & a & -\frac{b}{2} & & \\ & \ddots & \ddots & \ddots & \\ & & -\frac{b}{2} & a & -\frac{b}{2} \\ & & & -\frac{b}{2} & a \end{pmatrix}. \tag{2.59}$$

The partition function of the quadratic part plus $N e_{\mathrm{g}}$ is defined as

$$Z_0^{(N)}(h,\beta) = \mathrm{e}^{-\beta N e_{\mathrm{g}}} \int_{([-1,1]\times[-\pi,\pi])^N} \mathrm{e}^{-\beta H_0} \prod_j \mathrm{d}s_j \mathrm{d}r_j. \tag{2.60}$$

For large β, the integration domain of s_j and r_j can be approximately extended to $\mathbb{R}$, which yields

$$\int_{\mathbb{R}^{2N}} \mathrm{e}^{-\beta H_0} \mathrm{d}^{2N}x = \int_{\mathbb{R}^{2N}} \mathrm{e}^{-\frac{1}{2}\langle x, \beta A x\rangle} \mathrm{d}^{2N}x = \left(\det \frac{\beta A}{2\pi}\right)^{-1/2}. \tag{2.61}$$

The determinant of the tridiagonal matrix A_t is available in closed form [32], such that

$$\det A = (\det A_t)(\det A_r) = \left(\frac{bc}{2}\right)^N \frac{\sinh((N+1)\lambda)}{\sinh(\lambda)} \quad \text{with} \ \cosh(\lambda) = \frac{a}{b}. \tag{2.62}$$

Inserting these relations results in the free energy

$$F_0^{(N)}(h,\beta) \equiv -\frac{1}{\beta N} \log\big(Z_0^{(N)}(h,\beta)\big) = e_{\mathrm{g}} + \frac{1}{\beta} \log\Big(\frac{\beta}{2\pi}\sqrt{bc/2}\Big) + \frac{1}{2\beta N} \log\Big(\frac{\sinh((N+1)\lambda)}{\sinh(\lambda)}\Big). \tag{2.63}$$

In the thermodynamic limit $N \to \infty$,

$$\begin{aligned} F_0(h,\beta) &= \lim_{N\to\infty} F_0^{(N)}(h,\beta) = e_{\mathrm{g}} + \frac{1}{\beta} \log\Big(\frac{\beta}{2\pi}\sqrt{bc/2}\Big) + \frac{\lambda}{2\beta} \\ &= e_{\mathrm{g}} + \frac{1}{\beta}\left[\frac{1}{2}\mathrm{arccosh}\Big(\frac{a}{b}\Big) + \log(\beta\sqrt{bc/2}) - \log(2\pi)\right]. \end{aligned} \tag{2.64}$$

With this input we work out the free energy derivatives (2.51) to leading order in $1/\beta$ and obtain

$$\begin{aligned} &-\beta^{-1}\,\partial_\nu^2 F = \frac{1}{\beta c}, \qquad -\beta^{-1}\,\partial_h^2 F = 0, \qquad -\partial_\beta^2\,(\beta F) = 0, \\ &\partial_\beta(\beta\, F_0(h,\beta)) = e_{\mathrm{g}} + \frac{1}{\beta}, \qquad \partial_\beta\partial_\nu F = 0, \qquad \partial_\beta\partial_h F = 0. \end{aligned} \tag{2.65}$$

Therefore the speed of sound is given by $c_{\mathrm{s}} = \sqrt{(a-b)c}$. For $h = 0$ and $\Delta = 0.5$, we get $c_s = 1$. For the G matrices (at $h = 0$) we arrive at

$$G^+ = \frac{c_{\mathrm{s}}}{2}\begin{pmatrix} 0 & 0 & 0 \\ 0 & 0 & 1 \\ 0 & 1 & 0 \end{pmatrix}, \qquad G^0 = \frac{c_{\mathrm{s}}}{2}\begin{pmatrix} -1 & 0 & 0 \\ 0 & 0 & 0 \\ 0 & 0 & 1 \end{pmatrix}. \tag{2.66}$$

which for our values of parameter ($\Delta = 0.5$) gives,

$$G^+ = \begin{pmatrix} 0 & 0 & 0 \\ 0 & 0 & 0.5 \\ 0 & 0.5 & 0 \end{pmatrix}, \qquad G^0 = \begin{pmatrix} -0.5 & 0 & 0 \\ 0 & 0 & 0 \\ 0 & 0 & 0.5 \end{pmatrix}. \tag{2.67}$$

Bibliography

[1] K. Aoki and D. Kusnezov, "Bulk properties of anharmonic chains in strong thermal gradients: non-equilibrium $\varphi 4$ theory," Phys. Lett. A **265**, 250 (2000).

[2] J. Sirker, R. G. Pereira, and I. Affleck, "Conservation laws, integrability, and transport in one-dimensional quantum systems," Phys. Rev. B **83**, 035115 (2011).

[3] C. B. Mendl and H. Spohn, "Dynamic correlators of Fermi-Pasta-Ulam chains and nonlinear fluctuating hydrodynamics," Phys. Rev. Lett. **111**, 230601 (2013).

[4] S. G. Das, A. Dhar, K. Saito, C. B. Mendl, and H. Spohn, "Numerical test of hydrodynamic fluctuation theory in the Fermi-Pasta-Ulam chain," Phys. Rev. E **90**, 012124 (2014).

[5] C. Giardinà, R. Livi, A. Politi, and M. Vassalli, "Finite thermal conductivity in 1d lattices," Phys. Rev. Lett.**84**, 2144 (2000).

[6] O. V. Gendelman and A. V. Savin, "Normal heat conductivity of the one-dimensional lattice with periodic potential of nearest-neighbor interaction," Phys. Rev. Lett. **84**, 2381 (2000).

[7] L. Yang and P. Grassberger, "Are there really phase transitions in 1-d heat conduction models?" arXiv preprint arXiv: cond-mat/0306173 (2003).

[8] S. G. Das and A. Dhar, "Role of conserved quantities in normal heat transport in one dimenison," arXiv preprint arXiv:1411.5247 (2014).

[9] H. Spohn, "Fluctuating hydrodynamics for a chain of nonlinearly coupled rotators," arXiv:1411.3907 (2014).

[10] H. Spohn, "Nonlinear fluctuating hydrodynamics for anharmonic chains," J. Stat. Phys. **154**, 1191 (2014).

[11] H. Spohn, "Fluctuating Hydrodynamics Approach to Equilibrium Time Correlations for Anharmonic Chains", in *Thermal Transport in Low Dimensions: From Statistical Physics to Nanoscale Heat Transfer* (Lecture Notes in Physics), (S. Lepri, Ed. , Springer International Publishing, 2016).

[12] L. Faddeev and L. Takhtajan, *Hamiltonian methods in the theory of solitons*. (Springer Science & Business Media, 2007).

[13] M. Kulkarni and A. Lamacraft, "Finite-temperature dynamical structure factor of the one-dimensional bose gas: From the Gross-Pitaevskii equation to the Kardar-Parisi-Zhang universality class of dynamical critical phenomena," Phys. Rev. A **88**, 021603 (2013).

[14] M. Kulkarni, D. A. Huse, and H. Spohn, "Fluctuating hydrodynamics for a discrete Gross-Pitaevskii equation: Mapping onto the Kardar-Parisi-Zhang universality class," Phys. Rev. A **92**, 043612 (2015).

[15] C. B. Mendl and H. Spohn, "Low temperature dynamics of the one-dimensional discrete nonlinear Schrödinger equation," J. Stat. Mech. **2015**, P08028 (2015).

[16] C. B. Mendl and H. Spohn, "Equilibrium time-correlation functions for one-dimensional hard-point systems," Phys. Rev. E **90**, 012147 (2014).

[17] J. Zagorodny, "Dynamics of vortices in the two-dimensional anisotropic heisenberg model with magnetic fields," Ph.D. thesis, Universität Bayreuth, Bayreuth, Germany (2004).

[18] C. B. Mendl and H. Spohn, "Current fluctuations for anharmonic chains in thermal equilibrium," J. Stat. Mech. **2015**, P03007 (2015).

[19] H. Zhao, "Identifying diffusion processes in one-dimensional lattices in thermal equilibrium," Phys. Rev. Lett. **96**, 140602 (2006).

[20] A. Kundu and A. Dhar, "Equilibrium dynamical correlations in the toda chain and other integrable models," Phys. Rev. E **94**, 062130 (2016).

[21] T. Prosen and B. Žunkovič, "Macroscopic diffusive transport in a microscopically integrable hamiltonian system," Phys. Rev. Lett. **111**, 040602, (2013).

[22] A. Das, M. Kulkarni, H. Spohn, and A. Dhar, "Kardar-parisi-zhang scaling for the faddeev-takhtajan classical integrable spin chain," arXiv preprint arXiv:1906.02760 (2019).

[23] A. Das, S. Chakrabarty, A. Dhar, A. Kundu, D. A. Huse, R. Moessner, S. S. Ray, and S. Bhattacharjee, "Light-cone spreading of perturbations and the butterfly effect in a classical spin chain," Phys. Rev. Lett. **121**, 024101 (2018).

[24] A. Das, M. Kulkarni, A. Dhar, and D. A. Huse, *In preparation*, 2019.

[25] M. Prähofer and H. Spohn, "Exact scaling functions for one-dimensional stationary Kardar-Parisi-Zhang growth," J. Stat. Phys. **115**, 255 (2004).

[26] J. Frank, W. Huang, and B. Leimkuhler, "Geometric integrators for classical spin systems," J. Comput. Phys. **133**, 160 (1997).

[27] Y. Zhong, Y. Zhang, J. Wang, and H. Zhao, "Normal heat conduction in one-dimensional momentum conserving lattices with asymmetric interactions," Phys. Rev. E **85**, 060102 (2012).

[28] S. G. Das, A. Dhar, and O. Narayan, "Heat conduction in the α-β fermi–pasta–ulam chain," J. Stat. Phys. **154**, 204 (2014).

[29] L. Wang, B. Hu, and B. Li, "Validity of fourier's law in one-dimensional momentum-conserving lattices with asymmetric interparticle interactions," Phys. Rev. E **88**, 052112 (2013).

[30] A. Dhar, A. Kundu, J. L. Lebowitz, and J. A. Scaramazza, "Transport properties of the classical toda chain: effect of a pinning potential," .

[31] P. D. Cintio, S. Iubini, S. Lepri, and R. Livi, "Transport in perturbed classical integrable systems: The pinned toda chain," Chaos, Solitons & Fractals **117**, 249 (2018).

[32] G. Y. Hu and R. F. O'Connell, "Analytical inversion of symmetric tridiagonal matrices," Journal of Physics A: Mathematical and General **29**, 1511 (1996).

Chapter 3

Kardar-Parisi-Zhang Scaling for an Integrable Lattice Landau-Lifshitz Spin Chain

Key idaes: Recent studies report on anomalous spin transport for the integrable Heisenberg spin chain at its isotropic point. Anomalous scaling is also observed in the time-evolution of non-equilibrium initial conditions, the decay of current-current correlations, and non-equilibrium steady state averages. These studies indicate a space-time scaling with $x \sim t^{2/3}$ behavior at the isotropic point, in sharp contrast to the ballistic form $x \sim t$ generically expected for integrable systems. In our contribution we study the scaling behavior for the integrable lattice Landau-Lifshitz spin chain. We report on equilibrium spatio-temporal correlations and dynamics with step initial conditions. Remarkably, for the case with zero mean magnetization, we find strong evidence that the scaling function is identical to the one obtained from the stationary stochastic Burgers equation, alias Kardar-Parisi-Zhang equation. In addition, we present results for the easy-plane and easy-axis regimes for which, respectively, ballistic and diffusive spin transport is observed, whereas the energy remains ballistic over the entire parameter regime.

3.1 Introduction

Classical Hamiltonian systems are usually classified as non-integrable and integrable, depending on whether they possess either a small or a macroscopically large number of conserved fields. More precisely, a Hamiltonian system with N degrees of freedom is called integrable if one can find N independent constants of motion – otherwise, it is referred to as non-integrable. In general, one would expect integrable and non-integrable systems to have drastically different transport properties. Let us consider the example of a translation invariant one-dimensional mechanical system with $Q = \sum_{j=1}^{N} Q_j$ a conserved field satisfying a local conservation law of the form $\partial Q_j/\partial t = J_j - J_{j+1}$, where J_j is the corresponding local current. The corresponding dynamical equilibrium correlation function is defined by

$$C(j,t) = \langle Q_j(t) Q_0(0) \rangle_{\text{eq}}^{\text{c}}, \tag{3.1}$$

where the average is over initial conditions chosen from the Gibbs equilibrium distribution and the superscript denotes the connected part of the correlator, defined as $\langle Q_j(t)Q_0(0)\rangle_{\text{eq}}^{\text{c}} := \langle (Q_j(t) - \langle Q_0\rangle_{\text{eq}})(Q_0(0) - \langle Q_0\rangle_{\text{eq}})\rangle_{\text{eq}}$. Since Q is conserved, one expects a scaling form as

$$C(j,t) = \chi(\Gamma t)^{-\alpha} f\big((\Gamma t)^{-\alpha}(j - ct)\big). \tag{3.2}$$

$\alpha > 0$ is the scaling exponent, c a potential systematic shift (the "sound" velocity), Γ a model dependent parameter, and f the scaling function normalized with total sum equal to 1. Our particular form ensures that $\sum_j C(j,t) = \chi$ independent of t, and χ is the static susceptibility. For integrable systems most commonly $\alpha = 1$ and $c = 0$, which is the ballistic behavior. The scaling function depends on Q. On the other hand, in non-integrable systems one often observes $\alpha = \frac{1}{2}$ with a Gaussian scaling function. But also anomalous scaling with $\alpha = \frac{2}{3}$ has been discovered [1–8]. Such differences between integrable and non-integrable systems are also observed in other transport simulations, for instance in the evolution of non-equilibrium initial conditions and in properties of boundary driven non-equilibrium steady states (NESS). Through generalized hydrodynamics much progress has been accomplished in the understanding of transport in integrable systems [9–14].

A surprising exception to the generic behavior has been discovered for spin transport in the integrable XXZ Heisenberg spin chain. The quantum XXZ spin $\frac{1}{2}$ chain is Bethe ansatz solvable for an arbitrary choice of the anisotropy parameter Δ. The spectrum is gapless for $|\Delta| \leq 1$ and gapped otherwise. A number of studies find that, for zero z-magnetization, spin transport in this system is diffusive for $\Delta > 1$, ballistic for $\Delta < 1$ and anomalous at $\Delta = 1$. First indications of this behavior came from the Drude weight for spin transport [15–17]. Subsequent evidence was obtained in NESS studies at infinite

temperatures [18, 19], in the form of equilibrium correlation functions [20], and in the evolution of quenched initial conditions [21]. There has been some understanding of the un-expected diffusive and anomalous regimes of spin transport using the GHD framework [11, 22].

The goal of our contribution is to find out whether a similar pattern persists in corresponding classical models. One natural choice would be the classical Heisenberg model on the one-dimensional continuum, also known as the Landau-Lifshitz model, which is integrable and has the same rotational symmetries as the XXZ chain [23–26]. However numerical discretizations schemes might spoil integrability. Also the equilibrium states live on non-smooth spin configurations. For these reasons it is better to keep the underlying lattice, leading to the lattice Landau-Lifshitz (LLL) model, which in fact is non-integrable. Recent work [8] has explored spin and energy correlations. They turn out to be diffusive at high temperatures, while anomalous features emerge at low temperatures. Fortunately one can adjust the coupling function between nearest neighbors on the lattice in such a way that the model is integrable and still has the usual rotational symmetries [27–29] . We will refer to this model as the integrable lattice Landau-Lifshitz (ILLL) system. The ILLL model has a parameter ρ, which plays the role of the anisotropy parameter Δ in the Heisenberg model, such that $\rho > 0$ corresponds to easy-plane and $\rho < 0$ corresponds to easy-axis, while $\rho \to 0$ is the isotropic case. At the isotropic point all three components of the total magnetization are conserved. For zero average magnetization the corresponding current correlations were studied in [30]. Quite remarkably, the current correlation shows an exponential decay for easy-axis ($\rho < 0$) and hence a vanishing Drude weight and diffusive transport. Saturation to a non-zero value is observed for easy-plane ($\rho > 0$), implying a finite Drude weight and ballistic transport. For the isotropic model an anomalous decay of the form $\sim t^{-\alpha}$ with $\alpha \approx 0.65$ is found. In our contribution we investigate the scaling properties of equilibrium space-time correlations, for both spin and energy transport, again for zero average magnetization. We confirm the scaling exponents from previous studies for spin transport in different parameter regimes. In addition, we determine the scaling functions: Gaussian for the case of diffusive transport in the easy-axis regime, while at the isotropic point, remarkably, we have a convincing fit to the Kardar-Parisi-Zhang (KPZ) scaling form f_{KPZ} [described later in Equation. (3.13)] . The energy transport remains ballistic in all regimes.

Returning to the quantum XXZ chain, in [14, 31] the time evolution of the magnetization profile with a tiny initial step is studied. As expected from linear response, it is observed that for $\Delta > 1$ the magnetization profile has diffusive scaling $\alpha = \frac{1}{2}$, while, for $\Delta = 1$, the respective scaling function is anomalous with $\alpha = \frac{2}{3}$. In more recent work [32], it was found that the scaling function is related to the stationary KPZ equation. Such dynamical properties live on the ballistic hydrodynamic scale and are implicitly based on the assumption of local equilibrium. A similar reasoning can be applied to

classical systems and generically one expects to have comparable dynamical properties. Our study of the ILLL allows us to test more sharply whether such a conjecture holds. Indeed, we observe a clear KPZ scaling in the correlation functions. However, when investigating whether the KPZ scaling also holds for the evolution of the step-profile our data are too noisy for arriving at a definite conclusion. In a recent complementary study [33, 34], the classical-quantum correspondence has been analyzed in the context of the continuum Landau-Lifshitz model, which is integrable, and the quantum XXZ model at zero temperature.

The chapter is organized as follows. In Sec. 4.2, we provide the details of the model, discuss the quantities of interest, and give a brief analysis using linear response theory. We also describe the numerical methods used. Sec. 3.3 focuses on analyzing the equilibrium time correlations for all the three cases of the classical ILLL chain – isotropic, easy-plane, and easy-axis regimes. In Sec. 3.4, we study the evolution of an initial step magnetization profile and its scaling. We summarize our findings in Sec. 3.5 along with an outlook.

3.2 The classical chain

The classical ILLL [27–29] spin chain for N spins, $\vec{S}_j (j = 1, ..., N)$, $|\vec{S}_j| = 1$, is defined by the following Hamiltonian

$$H = \sum_{j=1}^{N} h(\vec{S}_j, \vec{S}_{j+1}), \tag{3.3}$$

where the nearest neighbor interactions are given by

$$\begin{aligned} h(\vec{S}, \vec{S}') = -\log \big| &\cos(\gamma S^{(z)}) \cos(\gamma S'^{(z)}) + (\cot(\gamma))^2 \sin(\gamma S^{(z)}) \sin(\gamma S'^{(z)}) \\ &+ (\sin(\gamma))^{-2} G(S^{(z)}) G(S'^{(z)}) (S^{(x)} S'^{(x)} + S^{(y)} S'^{(y)}) \big|, \\ G(x) = &\left(1 - x^2\right)^{-\frac{1}{2}} \left(\cos(2\gamma x) - \cos(2\gamma)\right)^{\frac{1}{2}}. \end{aligned} \tag{3.4}$$

γ is the model parameter which can be either real or purely imaginary. Without loss of generality, we introduce the new parameter $\rho = \gamma^2$, $\rho \in \mathbb{R}$. The boundary conditions will be taken to be either periodic or open, depending on the particular physical situation studied. Easy-plane corresponds to $\rho > 0$, easy-axis to $\rho < 0$, while in the limit $\rho \to 0$ one obtains the isotropic interaction,

$$h\left(\vec{S}, \vec{S}'\right) = -\log\left(1 + \vec{S} \cdot \vec{S}'\right). \tag{3.5}$$

Note that the "$-$" sign in front of h corresponds to the ferromagnetic interaction, whereas the positive sign will correspond to an anti-ferromagnetic interaction. In the present work we focus on the ferromagnetic Hamiltonian. For the anti-ferromagnetic case, the

potential is not bounded from below and hence there would be equilibration problems at low temperatures. To see this, we note that for the general case with $h(\vec{S},\vec{S}') = -J\log\big(1+\vec{S}\cdot\vec{S}'\big)$, with $J>0$ ($J<0$) corresponding to ferromagnetic (antiferromagnetic) interactions, the equilibrium state is given by,

$$\prod_j \big(1+\vec{S}_j\cdot\vec{S}_{j+1}\big)^{\beta J}. \tag{3.6}$$

For $J<0$ this Boltzmann weight becomes unbounded as two neighboring spins point oppositely and can no longer be normalized once $\beta J\le -1$. Close to that value typically the chain will have long anti-ferromagnetic domains, which slow down the evolution. A trace of this feature is still present at $\beta=0$. Thus we find for $\beta=0$ and $J=1$ that after 10^6 averages the data are still too noisy to pin down the tail behavior. More precise numerical data are achieved for $\beta=1$, and we use this value for all the simulations presented in this chapter.

The dynamics of spins is governed by Hamilton's equations of motion,

$$\frac{d}{dt}\vec{S}_j = \{\vec{S}_j, H\} = \vec{S}_j\times\vec{B}_j, \quad \vec{B}_j = -\nabla_{\vec{S}_j}H. \tag{3.7}$$

We study transport in this model, through both equilibrium and nonequilibrium properties.

(i) In the equilibrium simulations we use periodic boundary conditions and compute spin and energy space-time correlators defined by

$$\begin{aligned} C_{\rm ss}(j,t) &= \langle S_j^{(z)}(t)S_0^{(z)}(0)\rangle^{\rm c}_{\rm eq},\\ C_{\rm ee}(j,t) &= \langle e_j(t)e_0(t)\rangle^{\rm c}_{\rm eq} \end{aligned} \tag{3.8}$$

where $e_j = h(\vec{S}_j,\vec{S}_{j+1})$ and the truncated average $\langle\dots\rangle^{\rm c}_{\rm eq}$ is taken with respect to the equilibrium distribution $e^{-\beta H}/Z$.

(ii) In the nonequilibrium simulations, we consider an open XXX chain initially prepared with a uniform temperature and a step in the magnetization. More precisely, the initial state is $Z^{-1}\exp\big[-\beta\big(H-\sum_j h_j^{(z)}S_j^{(z)}\big)\big]$, where $h_j^{(z)}=-h_0$ for $j\le 0$ and $h_j^{(z)}=h_0$ for $j>0$. Of interest is the average magnetization $s(j,t)=\langle S_j^{(z)}(t)\rangle_{h_0}$ at time t, where the dynamics is according to H and the index recalls the dependence of the initial state on h_0. If the step is small, this average can be expanded in h_0. The zeroth order vanishes and, using that $C_{\rm ss}(j,t)=C_{\rm ss}(-j,t)$, to first order one arrives at

$$s(j,t) = \beta\sum_i h_i^{(z)}C_{\rm ss}(j-i,t)$$

$$= \beta h_0 \Big(C(0,t) + 2 \sum_{i=1}^{j} C_{\mathrm{ss}}(i,t) \Big) \tag{3.9}$$

for $j \geq 1$ with $s(-j+1,t) = -s(j,t)$. As a consequence, if $C_{\mathrm{ss}}(j,t)$ scales as in (3.2) with $c = 0$, then $s(j,t)$ inherits the corresponding scaling. In the continuum form one arrives at

$$s(x,t) = 2\beta h_0 \chi \int_0^{x/(\Gamma t)^{\alpha}} dx' f(x') \tag{3.10}$$

for $x \geq 0$. The derivative of the scaling function of s yields the scaling function for C. For example, if C_{ss} has Gaussian scaling, then $s(x,t)$ would scale with the error function. Note that the scaling exponent remains unchanged.

3.2.1 KPZ equation and scaling functions

KPZ equation describes the surface growth under a random ballistic deposition. The height function $h(x,t)$ is governed by the Langevin equation,

$$\partial_t h = \tfrac{1}{2}\lambda(\partial_x h)^2 + \nu \partial_x^2 h + \sqrt{D}\eta, \tag{3.11}$$

where η is normalized space-time white noise. The slope $u(x,t) = \partial_x h(x,t)$ is governed by the stochastic Burgers equation

$$\partial_t u + \partial_x \big(-\tfrac{1}{2}\lambda u^2 - \nu \partial_x u - \sqrt{D}\eta \big) = 0. \tag{3.12}$$

In the stationary state the mean of u can be chosen to vanish and $x \mapsto u(x,0)$ is spatial white noise of strength $\chi = D/2\nu$. As shown in [36] the two-point function of the stationary stochastic Burgers equation is given by

$$\langle u(0,0)u(x,t)\rangle \sim \chi(\Gamma t)^{-2/3} f_{\mathrm{KPZ}}\left((\Gamma t)^{-2/3} x\right). \tag{3.13}$$

Γ determines the non-universal time scale, which in the case of the Burgers equation turns out to be $\Gamma = \sqrt{2}\lambda$. The scaling function $f_{\mathrm{KPZ}}(x)$ is positive, symmetric relative to the origin, and normalized to 1. It looks like a Gaussian in bulk but has tails which decay as $\exp(-0.295|x|^3)$, hence faster than a Gaussian.

3.2.2 Simulation details

We integrate the evolution equation (3.7) using the adaptive Runge-Kutta method [35]. In some some regions in configuration space, the logarithmic interaction potential is very steep, and because of this the fixed step-size Runge-Kutta method turned out to be

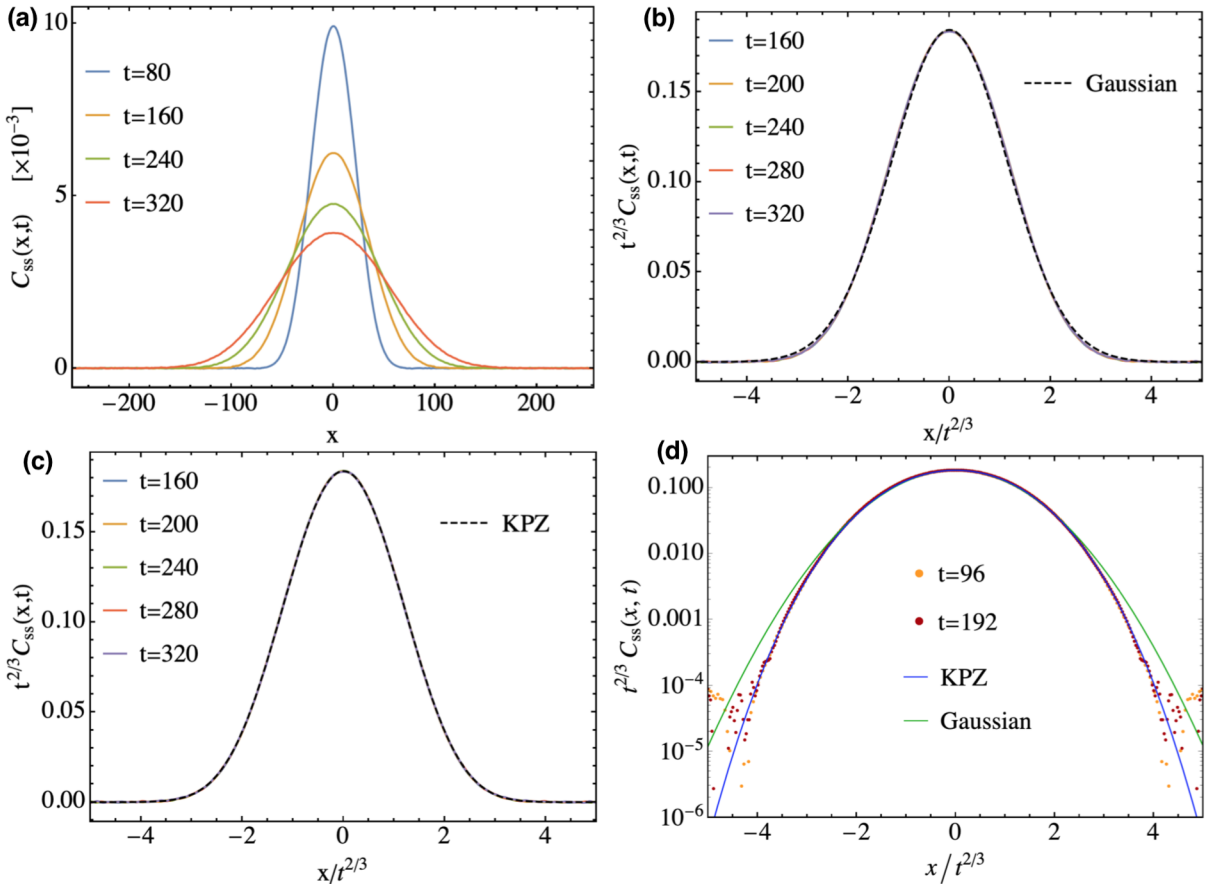

Figure 3.1: (Isotropic regime) (a) Plot of the spin-spin correlation $C_{\rm ss}(x,t)$. And the same after a $t^{2/3}$ scaling with a fit to (b) Gaussian and (c) the KPZ scaling functions. In (d) we show the two fits compared to the data in logarithmic $y-$scale. This plot reveals that the KPZ scaling function offers a much better fit to the data. Parameter values: system size = 2048, averaging over $\sim 10^6$ initial conditions and inverse temperature $\beta = 1$.

insufficient, especially at large times. One challenge is to keep the energy and the lengths of individual spins conserved during the numerical integration. Both these quantities dissipate quite a bit with time due to the accumulation of numerical errors. We give the input tolerance in the adaptive algorithm such that at the final time total energy remains conserved up to four decimal places and individual lengths of spins up to five decimal places. Total magnetization remains conserved well, up to 13 decimal places.

We use Metropolis Monte Carlo sampling to generate the canonical ensemble. Starting from an ordered initial configuration, we allow 5000 Monte Carlo swipes to make sure that the system has reached thermal equilibrium at the desired temperature. Once equilibrium has reached, we drop 500 swipes every time we generate a new thermal configuration to use as the initial condition for the time evolution. Thereby one ensures that the initial conditions used in the time evolution are sufficiently uncorrelated among themselves. All averages are taken over these initial conditions. The step initial profile is generated by equilibrating the system using a step magnetic field of the appropriate size at given temperature. In our study we chose the value of $\beta = 1$. At higher temperatures, the

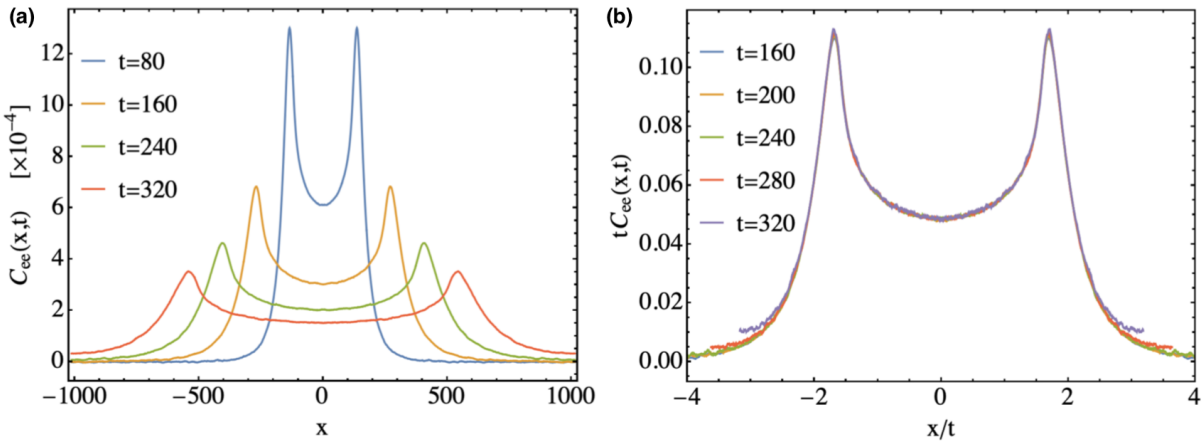

Figure 3.2: (Isotropic regime) Plot of the energy-energy correlation $C_{ee}(x,t)$ and the ballistic scaling of it. Parameter values: system size = 2048, final time = 320, averaging over $\sim 10^6$ initial conditions and inverse temperature $\beta = 1$.

average energy per site increases and the spins access the steeper parts of the inverted log potential [see (3.4)] and as a result the simulation using the adaptive step size algorithm becomes very slow [see discussion around Eq. (3.6)]. For the choice $\beta = 1$, the simulation efficiency is reasonable and it is expected that our main results should be valid at other temperatures.

3.3 Simulation results for equilibrium dynamical correlations

3.3.1 Isotropic regime

This corresponds to the choice $\rho \to 0$ in (3.4), which leads to the simpler form of the Hamiltonian (3.5). In this regime, spins have no directional bias and lie uniformly on the unit sphere. At infinite temperature these directions don't have any correlation but at finite and low temperatures the correlation grows. In Fig. 3.1(a) we plot the spin-spin correlation function $C_{\rm ss}(x,t)$ for $\beta = 1$. We see a very good $x \sim t^{2/3}$ scaling of the data. In Fig. 3.1(b) we compare the scaled data with a Gaussian distribution, while in Fig. 3.1(c) we compare the same data with the KPZ distribution. We first compute the sum $\sum_j C_{\rm ss}(j,t)$, which is independent of time and gives an estimate of the area under the fit curve. This is essentially the value of χ in (3.2). Then we find the best fit parameter Γ using the NonlinearModelFit function of Mathematica. In particular, we found that $\chi = 0.526698$ and $\Gamma = 1.93609$ for $f_{\rm KPZ}$ and 1.21582 for $f_{\rm Gaussian}$. Although the distinction is not so significant on this scale, we see that a much better fit is obtained with the KPZ distribution. The distinction becomes very prominent in the log plot shown in Fig. 3.1(d). This is because the KPZ scaling function differs from a Gaussian only in

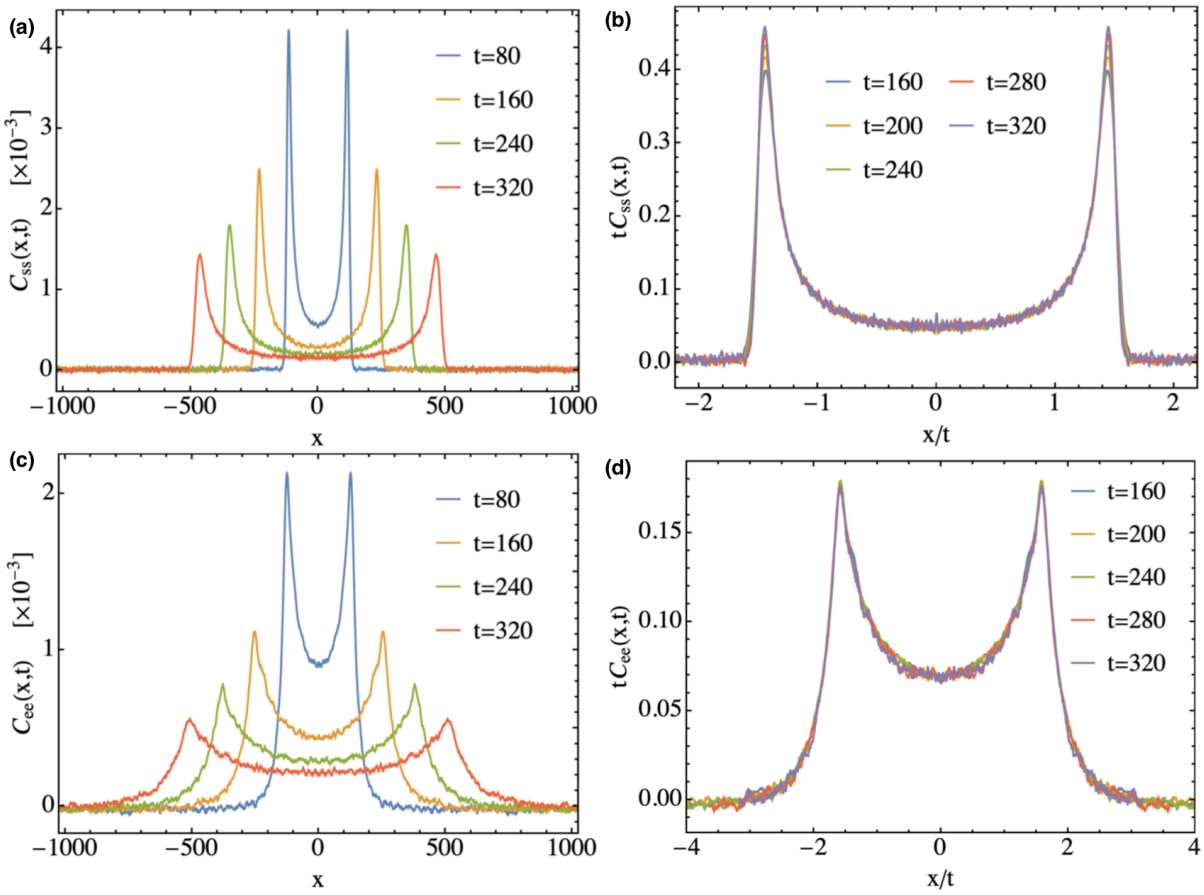

Figure 3.3: (Easy plane regime) Plot of the spin-spin correlation $C_{\rm ss}(x,t)$ and energy-energy correlation $C_{ee}(x,t)$ in easy-plane regime and corresponding ballistic scalings. Parameter values: system size =2048, averaging over $\sim 4\times 10^4$ initial conditions and inverse temperature $\beta = 1$.

the tails. Although spin transport is superdiffusive in this regime of the Hamiltonian, energy transport is ballistic. Energy correlations are plotted in Fig. 3.2 which show a clear ballistic scaling.

Note that, in many cases, the diffusive or superdiffusive modes come coupled with the ballistic modes and to see them one needs to subtract the ballistic contributions, which is a difficult task in general [10]. In our case it turns out that for spin transport at the isotropic point the ballistic contribution does not exist and we directly see the superdiffusive mode.

3.3.2 Easy-plane regime

This corresponds to the choice $\rho > 0$ in Eq. (3.4). Spins tend to lie near the $x-y$ plane at finite temperatures. We use the value $\rho = 1$. As shown in Fig. (3.3), both spin and energy show ballistic scaling in this regime. We however observe that spin transport is slower than the energy transport. In other words, in Fig. 3.3 the line shapes for spin and energy transport are distinctly different.

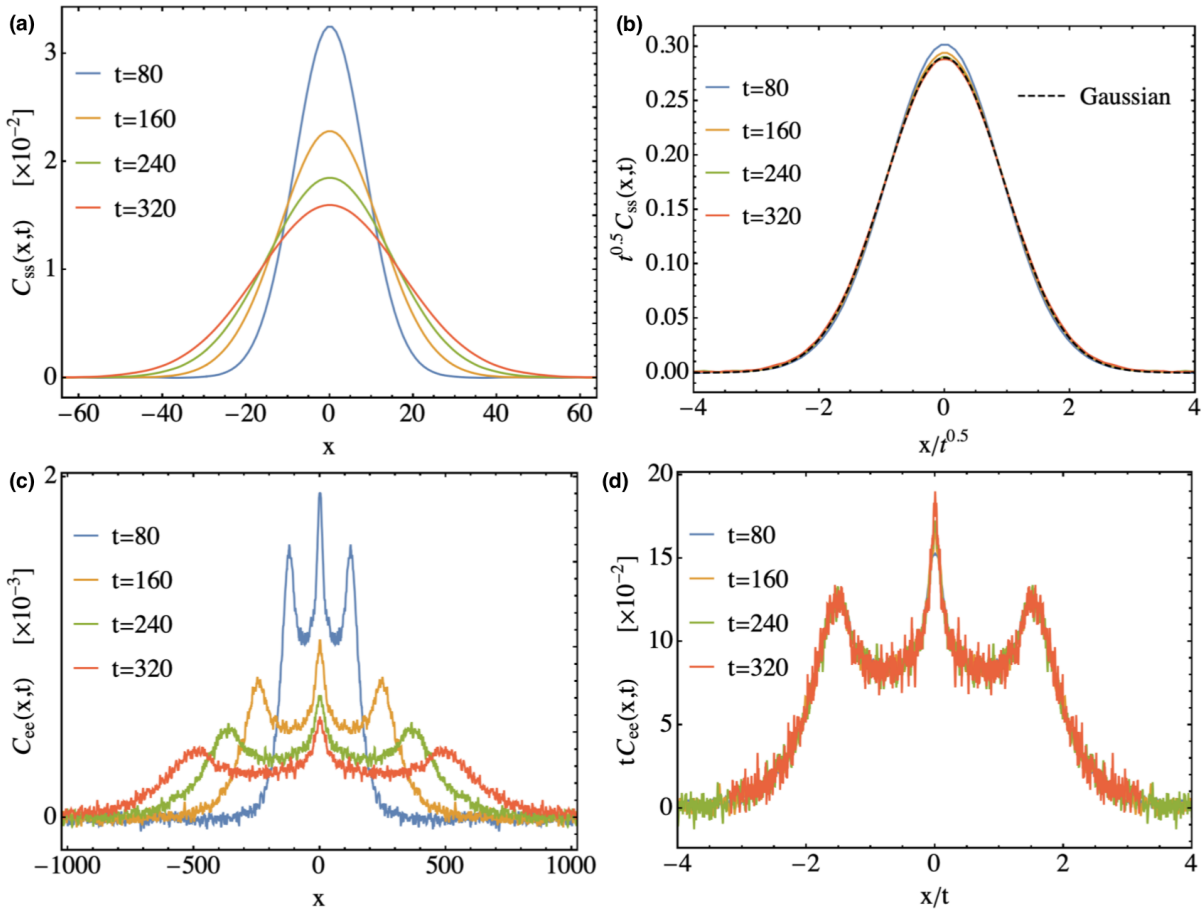

Figure 3.4: (Easy axis regime) Spin-spin correlation $C_{ss}(x,t)$ and energy-energy correlation $C_{ee}(x,t)$ in easy-axis regime. In (b) we show the diffusive scaling of spin correlations while in (d) we see the ballistic scaling of energy correlations. Parameter values: system size = 2048, averaging over $\sim 4 \times 10^4$ initial conditions and inverse temperature $\beta = 1$.

3.3.3 Easy-axis regime

This corresponds to the choice $\rho < 0$ in Eq. (3.4), i.e. γ becomes purely imaginary and the trigonometric functions become hyperbolic functions in the Hamiltonian. For our purpose, we use the value $\rho = -1$. In this regime, spins have the tendency to lie near the z-axis at finite temperatures. As shown in Fig. 3.4, we now observe that spin correlations spread diffusively while energy correlations spread ballistically. In this particular regime we have diffusive transport of spin. In Table. 3.1, we summarize the transport properties in the ILLL chain.

3.4 Magnetization profile for step initial condition

We consider now a chain of $N = 512$ spins and prepare it at the inverse temperature $\beta = 1$ using a step magnetic field as described in Sec. 4.2 with $h_0 = 0.01$. We average over 8×10^5 such initial conditions. The resulting step height in the magnetization is ± 0.00665. These

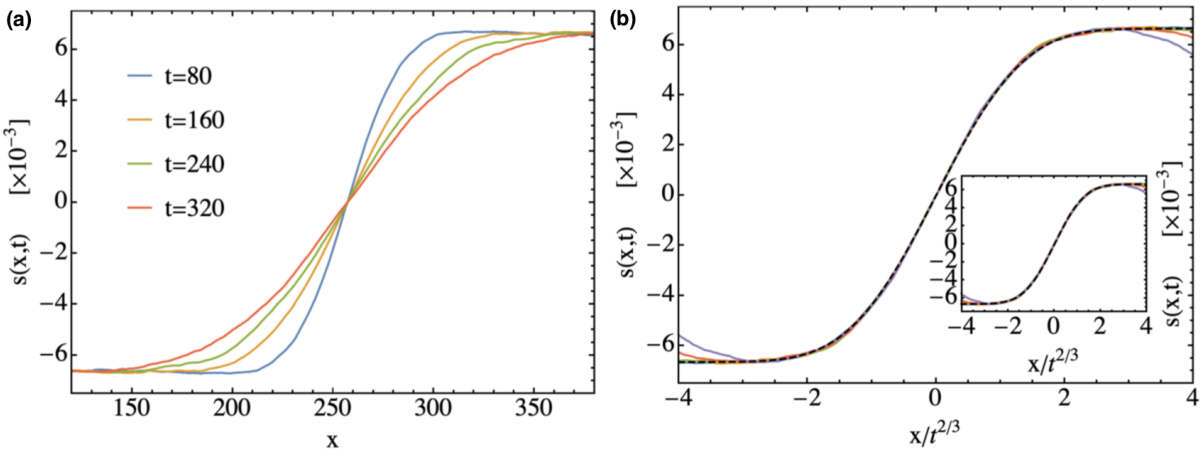

Figure 3.5: (Isotropic regime) (a) Magnetization profile at different times starting from a step initial condition. (b) Collapse of the data under a $t^{2/3}$ scaling. The dashed line corresponds to the integrated KPZ scaling function (3.10). Inset shows the fit with integrated Gaussian, namely the Error function. Although the 2/3 scaling is prominent, we cannot distinguish the (integrated) Gaussian and KPZ here. Parameter values: System size = 512, inverse temperature $\beta = 1$ and averaging over $\sim 8 \times 10^5$ initial conditions.

step initial conditions are evolved according to the isotropic Hamiltonian (3.5) and we monitor the average magnetization profile $s(x,t)$ at later times. Magnetization profiles at different times are shown in Fig. 3.5(a), while Fig. 3.5(b) shows the 2/3 scaling of $s(x,t)$. This is expected from (3.10) and our previous finding of 2/3 scaling of $C_{SS}(x,t)$ in the isotropic regime. Although $s(x,t)$ correctly reproduces the scaling exponent, the data is noisy and not accurate enough for us to rule out a fit to an error function (integral of a Gaussian). In Fig. 3.5(b) we show the fit with integral of $f_{\rm KPZ}$ and, in the inset, we show the fit with the error function. Much more averaging over the initial conditions is required to arrive at smoother data shown here. Here we are essentially dealing with (3.10). This equation is supposed to be exact in the linear response limit $h_0 \to 0$, and so one should recover the same values of Γ's and χ obtained from $C_{\rm ss}$ data by analyzing the step profile. However, in our simulations we have kept $h_0 = 0.01$ and as a result we observe slight deviations in the Γ and χ values. Here we see $\chi = 0.665$ and $\Gamma = 1.74603$ for both KPZ and Gaussian functions.

3.5 Summary

From the study of several integrable many-body systems, there seems to be a consensus that their large scale behavior has many common features. In particular, since based on hydrodynamic type arguments, quantum models should not differ from their classical version. We presented the numerical study of the classical integrable ILLL spin chain and compared with previous studies of the quantum XXZ Heisenberg model. Our findings are summarized in Table-3.1 and support the view that on hydrodynamic scales

Table 3.1: Summary of transport properties in the ILLL model for zero z-magnetization

Regime	**Spin transport**	**Energy transport**
Easy plane ($\rho > 0$)	Ballistic	Ballistic
Isotropic ($\rho \to 0$)	Super-diffusive scaling exponent: 2/3 scaling function: KPZ	Ballistic
Easy axis ($\rho < 0$)	Diffusive scaling function: Gaussian	Ballistic

Note: Diffusive transport implies scaling exponent = 1/2 and ballistic transport implies scaling exponent = 1.

classical and quantum cannot be distinguished. At the isotropic point with zero average magnetization, we find that the quantities involving spin show superdiffusive behavior with scaling exponent 2/3 and the scaling function is KPZ. In the easy-plane regime, we find that the spin transport is ballistic, while in the easy-axis regime it is diffusive. The energy correlations are shown to exhibit ballistic scaling in all parameter regimes. To probe the KPZ behavior further we also studied the evolution of an initial magnetization step. Again, we find the $t^{2/3}$ scaling but, from these data, we are not able to conclusively differentiate between KPZ and Gaussian scaling.

While the numerical evidence is pointing in the expected direction, strong theoretical arguments are still missing.Of course, a first inclination is to compare the corresponding GHD, which is available for the quantum XXZ model but currently not for its classical version. In addition, KPZ scaling requires a particular nonlinearity and noise, which is beyond conventional GHD.

Bibliography

[1] C. B. Mendl, and H. Spohn. "Dynamic correlators of Fermi-Pasta-Ulam chains and nonlinear fluctuating hydrodynamics", Phys. Rev. Lett. **111**, 230601 (2013).

[2] C. B. Mendl and H. Spohn, "Equilibrium time-correlation functions for one-dimensional hard-point systems", Phys. Rev. E **90**, 012147 (2014).

[3] S. G. Das, A. Dhar, K. Saito, C. B. Mendl, and H. Spohn, "Numerical test of hydrodynamic fluctuation theory in the Fermi-Pasta-Ulam chain", Phys. Rev. E **90**, 012124 (2014).

[4] M. Kulkarni, and A. Lamacraft, "Finite-temperature dynamical structure factor of the one-dimensional bose gas: From the Gross-Pitaevskii equation to the Kardar-Parisi-Zhang universality class of dynamical critical phenomena", Phys. Rev. A **88**, 021603(R) (2013).

[5] M. Kulkarni, D. A. Huse, and H. Spohn, "Fluctuating hydrodynamics for a discrete Gross-Pitaevskii equation: Mapping onto the Kardar-Parisi-Zhang universality class", Phys. Rev. A **92**, 043612 (2015).

[6] H. Spohn, "Fluctuating hydrodynamics for a chain of nonlinearly coupled rotators", arXiv preprint arXiv:1411.3907 (2014).

[7] S. G. Das, and A. Dhar, "Role of conserved quantities in normal heat transport in one dimension", arXiv preprint arXiv:1411.5247 (2014).

[8] A. Das, K. Damle, A. Dhar, D. A. Huse, M. Kulkarni, C. B. Mendl, and H. Spohn, "Nonlinear Fluctuating Hydrodynamics for the Classical XXZ Spin Chain", arXiv preprint arXiv:1901.00024v1 (2019).

[9] H. Spohn, "Interacting and noninteracting integrable systems", J. Math. Phys. **59**, 091402 (2018).

[10] J. De Nardis, D. Bernard, and B. Doyon, "Hydrodynamic Diffusion in Integrable Systems", Phys. Rev. Lett. **121**, 160603 (2018).

[11] E. Ilievski, J. De Nardis, M. Medenjak, and T. Prosen, "Superdiffusion in One-Dimensional Quantum Lattice Models", Phys. Rev. Lett. **121**, 230602 (2018).

[12] O. A. Castro-Alvaredo, B. Doyon, and T. Yoshimura, "Emergent Hydrodynamics in Integrable Quantum Systems Out of Equilibrium", Phys. Rev. X **6**, 041065 (2016).

[13] V. B. Bulchandani, R. Vasseur, C. Karrasch, and J. E. Moore, "Solvable Hydrodynamics of Quantum Integrable Systems", Phys. Rev. Lett. **119**, 220604 (2017).

[14] B. Bertini, M. Collura, J. De Nardis, and M. Fagotti, "Transport in Out-of-Equilibrium XXZ Chains: Exact Profiles of Charges and Currents", Phys. Rev. Lett. 117, 207201 (2016).

[15] X. Zotos, F. Naef, and P. Prelovsek, "Transport and conservation laws", Phys. Rev. B **55**, 11029 (1997).

[16] X. Zotos, "Finite Temperature Drude Weight of the One-Dimensional Spin-$\frac{1}{2}$ Heisenberg Model", Phys. Rev. Lett. **82**, 1764 (1999).

[17] J. Sirker, R. G. Pereira, and I. Affleck, "Conservation laws, integrability, and transport in one-dimensional quantum systems", Phys. Rev. B **83**, 035115 (2011).

[18] T. Prosen, and M. Žnidarič, "Matrix product simulations of non-equilibrium steady states of quantum spin chains", J. Stat. Mech.: Theory Exp. **P02035** (2009).

[19] M. Žnidarič, "Spin Transport in a One-Dimensional Anisotropic Heisenberg Model", Phys. Rev. Lett. **106**, 220601 (2011).

[20] R. Steinigeweg, and J. Gemmer, "Density dynamics in translationally invariant spin-$\frac{1}{2}$ chains at high temperatures: A current-autocorrelation approach to finite time and length scales", Phys. Rev. B **80**, 184402 (2009).

[21] C. Karrasch, J. E. Moore, and F. Heidrich-Meisner, "Real-time and real-space spin and energy dynamics in one-dimensional spin-$\frac{1}{2}$ systems induced by local quantum quenches at finite temperatures" Phys. Rev. B **89**, 075139 (2014).

[22] S. Gopalakrishnan, and R. Vasseur, "Kinetic theory of spin diffusion and superdiffusion in XXZ spin chains", Phys. Rev. Lett. **122**, 127202 (2019).

[23] M. Lakshmanan, T. Ruijgrok, and C. Thompson, "On the dynamics of a continuum spin system", Physica A **84**, 577 (1976).

[24] M. Lakshmanan, "Continuum spin system as an exactly solvable dynamical system", Phys. Lett. A **61**, 53 (1977).

[25] L. Takhtajan, "Integration of the continuous Heisenberg spin chain through the inverse scattering method", Phys. Lett. A **64**, 235 (1977).

[26] H. C. Fogedby, "Solitons and magnons in the classical Heisenberg chain", J. Phys. A **13**, 1467 (1980).

[27] E. K. Sklyanin, "Classical limits of the SU (2)-invariant solutions of the Yang-Baxter equation", Journal of Soviet Mathematics **40**, 93 (1988).

[28] E. K. Sklyanin, "Some algebraic structures connected with the Yang—Baxter equation", Func. Anal. Appl. **16**, 263 (1982).

[29] L. Faddeev, and L. Takhtajan, *Hamiltonian methods in the theory of solitons*, Springer Science and Business Media (2007).

[30] T. Prosen and B. Žunkovič, "Macroscopic Diffusive Transport in a Microscopically Integrable Hamiltonian System", Phys. Rev. Lett. **111**, 040602 (2013).

[31] M. Ljubotina, M. Žnidarič, and T. Prosen, "Spin diffusion from an inhomogeneous quench in an integrable system", Nat. comm. **8**, 16117 (2017).

[32] M. Ljubotina, M. Žnidarič, and T. Prosen, "Kardar-Parisi-Zhang physics in the quantum Heisenberg magnet", Phys. Rev. Lett. **122**, 210602 (2019).

[33] O. Gamayun, Y. Miao, and E. Ilievski, "Domain-wall dynamics in the Landau-Lifshitz magnet and the classical-quantum correspondence for spin transport", Phy. Rev. B **99**, 140301(R) (2019).

[34] G. Misguich, N. Pavloff, and V. Pasquier, "Domain wall problem in the quantum XXZ chain and semiclassical behavior close to the isotropic point" arXiv preprint arXiv:1905.08756.

[35] W. H. Press, S. A. Teukolsky, W. T. Vetterling, and B. P. Flannery, *Numerical recipes 3rd edition: The art of scientific computing*, Cambridge university press (2007).

[36] M. Prähofer, and H. Spohn, "Exact scaling functions for one-dimensional stationary KPZ growth", J. Stat. Phys. **115**, 255–279 (2004).

Chapter 4

Quantum Brownian Motion: Drude and Ohmic Baths as Continuum Limits of the Rubin Model

Key ideas: The motion of a free quantum particle in a thermal environment is usually described by the quantum Langevin equation, where the effect of the bath is encoded through a dissipative and a noise term, related to each other via the fluctuation dissipation theorem. The quantum Langevin equation can be derived starting from a microscopic model of the thermal bath as an infinite collection of harmonic oscillators prepared in an initial equilibrium state. The spectral properties of the bath oscillators and their coupling to the particle determine the specific form of the dissipation and noise. Here we investigate in detail the well-known Rubin bath model, which consists of a one-dimensional harmonic chain with the boundary bath particle coupled to the Brownian particle. We show how in the limit of infinite bath bandwidth, we get the Drude model and a second limit of infinite system-bath coupling gives the Ohmic model. A detailed analysis of relevant correlation functions, such as the mean squared displacement, velocity auto-correlation functions, and the response function are presented, with the aim of understanding of the various temporal regimes. In particular, we discuss the quantum to classical crossover time scales where the mean square displacement changes from a $\sim \ln t$ to a $\sim t$ dependence. We relate our study to recent work using linear response theory to understand quantum Brownian motion.

4.1 Introduction

A good effective description for the motion of a classical Brownian particle in a thermal environment at temperature T is given by the Langevin equation[1]. Considering motion in one dimension this is given by

$$M\dot{v} = -\gamma v + \eta(t) \ , \tag{4.1}$$

where $v = \dot{x}$ is the velocity of the particle, x its position, γ the dissipation constant and $\eta(t)$ is a Gaussian noise term with mean zero and correlations given by the fluctuation-dissipation relation $\langle \eta(t)\eta(t')\rangle = 2\gamma k_B T\delta(t-t')$. Some of the most important properties of this effective dynamics are that the particle reaches thermal equilibrium with its velocity given by the Maxwell distribution with $\langle v\rangle = 0$ and $\langle v^2\rangle = k_BT/M$. On the other hand, the mean square displacement (MSD) shows diffusive growth at long times, $\Delta(t) = \langle [x(t) - x(0)]^2\rangle = 2Dt$ (for $t \to \infty$), with a diffusion constant $D = k_BT/\gamma$.

The quantum version of this equation was first written by Ford, Kac and Mazur [2]. Unlike the classical case, where the Langevin equation can be established using a purely phenomenological approach (see [3]), the quantum case requires a microscopic modeling of the heat bath. The standard model for a heat bath is to treat it as an infinite collection of oscillators which is coupled to the system of interest, namely the Brownian particle. Eliminating the bath degrees, it can be shown that the effective dynamics of the particle is described by a quantum generalized Langevin equation, where the dissipation term has memory. A special choice of bath leads to the so-called Ohmic form [4] of Eq. (4.1), with the noise correlations changed to the form

$$\langle \eta(t)\eta(t')\rangle = \frac{\gamma}{\pi}\int_0^\infty d\omega\hbar\omega[2f(\omega,T)+1]\cos\omega(t-t') \ , \tag{4.2}$$

where $f(\omega,T) = [e^{\beta\hbar\omega}-1]^{-1}$ is the phonon distribution function. In particular we notice that in the quantum case, the noise is always correlated and there is no Markovian limit. Interestingly, even at zero temperature there is noise arising from quantum fluctuations and it has been shown that this leads to a logarithmic growth of the MSD with time, $\Delta_t \sim (\hbar/\gamma)\ln(t\gamma/M)$[5, 6]. A pecularity of the quantum system is that the kinetic energy of the particle diverges [7]. This divergence arises due to the contribution of high frequency modes to the zero-point energy and can be avoided by considering a finite bandwidth bath which leads to a damping term with memory. Since the original work of [2], quantum Brownian motion has been investigated using multiple approaches including quantum Langevin equations [8], path integral methods [9, 10], equilibrium dynamical correlations[11] and linear response theory[11]. Other relevant references are [12–26].

In the present work, we discuss one of the simplest models of a quantum heat bath,

the so-called Rubin bath [14]. In general it corresponds to a bath with a dissipation kernel with long time memory, decaying as a power-law. However we point out that as special limits it leads to the Ohmic bath (dissipation kernel is a delta function in time) and the Drude bath (dissipation kernel is exponentially decaying in time) [4]. A different limiting procedure to obtain the Ohmic bath has been discussed in [27]. For the three bath models we discuss in detail the form of the MSD, as well as the velocity auto-correlation function and the response function. We try to understand interesting physical aspects and highlight some of the qualitative differences. In recent years an approach based on linear response and fluctuation-dissipation theorem [28, 29] has been used to study Brownian motion at zero temperature. We point out here that this approach is exact for the case of the Rubin model of bath.

This chapter is organized as follows. In Sec. (4.2) we introduce the Hamiltonian and derive the generalized Langevin equation for the system by integrating out the bath degrees of freedom. In Sec. (4.3) we compute relevant correlation functions - mean square displacements, velocity auto-correlation functions and the response functions. In the same section we take a continuum limit of the model and show that the conventional and simpler models of bath, Drude and Ohmic, emerge. We end the chapter with a few concluding remarks.

4.2 Hamiltonian and derivation of the generalised Langevin equation

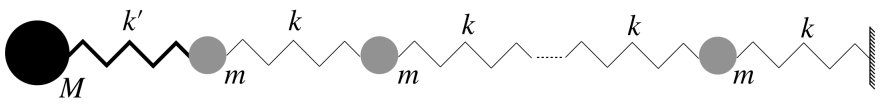

Figure 4.1: Setup of the problem.

Our set-up consisting of a single particle coupled to the Rubin bath is schematically shown in Fig. (4.1). We consider a particle of mass M with position and momentum operators specified by x and p respectively, while the bath consists of N particles of mass m and position and momentum operators given by $\{x_j, p_j\}$, $j = 1, 2, \ldots N$ that are coupled by harmonic springs of stiffness k. The Hamiltonian of the coupled system and bath is given by

$$\mathcal{H} = \frac{p^2}{2M} + \frac{k'}{2}(x - x_1)^2 + \sum_{n=1}^{N} \frac{p_n^2}{2m} + \frac{k}{2}\sum_{n=1}^{N}(x_n - x_{n+1})^2, \tag{4.3}$$

where we consider the right boundary to be fixed $x_{N+1} = 0$. Even though our test particle (x, p) is tied to the bath, we will see that in the limit $N \to \infty$, the effective

motion corresponds to that of a free particle. For our analysis, it is convenient to write the above Hamiltonian in the following form:

$$\begin{aligned}
&\mathcal{H} = \mathcal{H}_S + \mathcal{H}_B + \mathcal{H}_{SB} \ , \qquad (4.4)\\
&\text{where} \ \ \mathcal{H}_S = \frac{p^2}{2M} + \frac{k'}{2}x^2 \ , \ \ \mathcal{H}_{SB} = -k'xx_1 \ ,\\
&\mathcal{H}_B = \sum_{n=1}^{N} \frac{p_n^2}{2m} + \frac{k'}{2}x_1^2 + \frac{k}{2}\sum_{n=1}^{N-1}(x_n - x_{n+1)})^2 + \frac{k}{2}x_{N+1}^2 \ .
\end{aligned}$$

The bath Hamiltonian can be written in the compact form $\mathcal{H}_B = \mathbf{p}^T m^{-1}\mathbf{p}/2 + \mathbf{x}^T\phi\mathbf{x}/2$, where $\mathbf{x} = (x_1, x_2, \ldots, x_N)$ and $\mathbf{p} = (p_1, p_2, \ldots, p_N)$ and ϕ is the force matrix. Let us consider a linear transformation $\mathbf{X} = m^{1/2}U\mathbf{x}$ and $\mathbf{P} = m^{1/2}U\mathbf{p}$ where U is an orthogonal transformation which diagonalizes the force matrix, i.e, $U\phi U^T = m\Omega^2$, where Ω^2 is the diagonal matrix with elements given by the normal mode frequencies of the bath $\Omega^2 = \{\Omega_s^2\}$, with $s = 1, 2, \ldots, N$. Note that the column vector formed by the matrix elements U_{si} gives the normal mode eigenfunction corresponding to the eigenvalue Ω_s^2. Using the normal mode coordinates X_s and momenta P_s the system-bath coupling and the bath Hamiltonian can be written as

$$\begin{aligned}
&\mathcal{H}_{SB} = -k'xx_1 = -k'\sum_{s=1}^{N} C_s x X_s, \ \text{where} \ C_s = m^{-1/2}U_{s1}\\
&\mathcal{H}_B = \sum_{s=1}^{N} \frac{P_s^2}{2} + \frac{\Omega_s^2 X_s^2}{2} \ . \qquad (4.5)
\end{aligned}$$

To derive the effective Langevin equations for the system, one starts by writing the Heisenberg equations of motion of the system and the bath degrees of freedom given by

$$M\ddot{x} = -k'x + k'\sum_{s=1}^{N} C_s X_s, \qquad (4.6)$$

$$\ddot{X}_s = -\Omega_s^2 X_s + k'C_s x \ , \quad s = 1, 2, \ldots, N. \qquad (4.7)$$

The bath equations of motion Eq. (4.7) can be solved formally, assuming initial conditions $\{X_s(t_0), P_s(t_0)\}$ that are chosen, at time t_0, from the Boltzmann distribution $e^{-\beta\mathcal{H}_B}/\mathrm{Tr}\left[\mathrm{e}^{-\beta\mathcal{H}_\mathrm{B}}\right]$ at temperature $T = (k_B\beta)^{-1}$. This gives

$$\begin{aligned}
X_s(t) = &\cos\{\Omega_s(t-t_0)\}\, X_s(t_0) + \frac{\sin\{\Omega_s(t-t_0)\}}{\Omega_s}P_s(t_0)\\
&+ k'C_s\int_{t_0}^{t} dt' \frac{\sin\{\Omega_s(t-t')\}}{\Omega_s}x(t') \ . \qquad (4.8)
\end{aligned}$$

Plugging this into the equation of motion of the system we get

$$M\ddot{x} = -k'x + \int_{t_0}^{t} dt' \Sigma(t-t')x(t') + \eta(t) \ , \tag{4.9}$$

where

$$\begin{aligned}
\Sigma(t) &= k'^2 \sum_{s=1}^{N} C_s^2 \frac{\sin(\Omega_s t)}{\Omega_s}, \\
\eta(t) &= k' \sum_{s=1}^{N} C_s \Big[\cos\left\{\Omega_s(t-t_0)\right\} X_s(t_0) + \frac{\sin\left\{\Omega_s(t-t_0)\right\}}{\Omega_s} P_s(t_0) \Big].
\end{aligned} \tag{4.10}$$

The form in Eq. (4.9) is in the form of a generalized Langevin equation, with $\Sigma(t)$ as the memory kernel and $\eta(t)$ as the random force term. The information about the baths is completely contained in these two terms. In the above equation it is necessary to take the limits $N \to \infty$ and then $t_0 \to -\infty$, in this precise order, to get the required bath properties. Indeed, apparent dissipation arises in this Hamiltonian model because of the flow of energy into the infinite degrees of freedom of the bath. It is instructive to write the above equations in the usual form of Langevin equations where the dissipation term involves the velocity rather than the positional degree of freedom. For this we define the dissipation kernel

$$\gamma(t) = k'^2 \sum_{s=1}^{N} C_s^2 \frac{\cos(\Omega_s t)}{\Omega_s^2}, \tag{4.11}$$

so that,

$$\Sigma(t) = -\frac{d\gamma(t)}{dt} \ . \tag{4.12}$$

We plug this into Eq. (4.9) and perform an integration by parts. Then, using the identities $\gamma(0) = k'^2 \sum_{s=1}^{N} \frac{C_s^2}{\Omega_s^2} = k'^2 \left[\phi^{-1}\right]_{11} = k'$ and $\gamma(\infty) = 0$, which can be proved in the $N \to \infty$ limit (for a reasonable choice of bath properties which are indeed satisfied by the baths we have considered here) and setting $t_0 \to -\infty$, we get

$$M\ddot{x} = -\int_{-\infty}^{t} dt' \gamma(t-t')\dot{x}(t') + \eta(t) \ , \tag{4.13}$$

where we now see that the pinning potential does not appear, which is what one would like for a free particle. We will now compute the bath properties in the $N \to \infty$ limit. It is useful to define the bath spectral functions

$$\Sigma^{+}(\omega) = \int_0^{\infty} dt \Sigma(t) e^{i\omega t} = k'^2 \sum_s \frac{C_s^2}{-(\omega + i\epsilon)^2 + \Omega_s^2}$$

$$\Gamma(\omega) = \mathrm{Im}\left[\Sigma^{+}(\omega)\right] = \mathrm{k'}^{2} \sum_{\mathrm{s}} \frac{\pi \mathrm{C}_{\mathrm{s}}^{2}}{2\omega} \left[\delta(\omega - \Omega_{\mathrm{s}}) + \delta(\omega + \Omega_{\mathrm{s}})\right]. \tag{4.14}$$

The statistical properties of the noise term can be obtained using the fact that at $t = t_0$ the bath is in thermal equilibrium at temperature T. Thus we find that $\langle \eta(t) \rangle = 0$ while the noise correlations are easiest to state in the Fourier domain. Defining $\tilde{\eta}(\omega) = \int_{-\infty}^{\infty} dt \eta(t) e^{i\omega t}$, we find [4]

$$\langle \tilde{\eta}(\omega) \tilde{\eta}(\omega') \rangle = 4\hbar\pi \ \Gamma(\omega)[f(\omega, T) + 1] \ \delta(\omega + \omega') \ , \tag{4.15}$$

where $f(\omega, T) = [e^{\beta\hbar\omega} - 1]^{-1}$ is the phonon distribution function. To compute $\Sigma^{+}(\omega)$, we note that it is precisely given by $k'^{2} \ g^{+}_{1,1}$ where $g^{+} = [-m(\omega + i\epsilon)^2 + \phi]^{-1}$ is the phonon Green's function of the heat bath and g^{+}_{11} refers to its diagonal element at site $n = 1$, corresponding to the particle that is coupled to the system. The computation of $g^{+}(\omega)$ becomes a bit involved because of the presence of the "impurity" term in the bath Hamiltonian $\mathcal{H}_B$ in Eq. (4.4). However, this can still be obtained explicitly and one eventually obtains [30]

$$\Sigma^{+}(\omega) = k'^{2} \frac{e^{iq}}{k + (k' - k)e^{iq}}, \tag{4.16}$$

where q is given by the solution of the dispersion $\omega^2 = (2k/m)(1 - \cos q)$. In the frequency range $|\omega| \leq 2\sqrt{k/m}$, we get real values for q and then we have

$$\Gamma(\omega) = \frac{k'^{2} k \sin q}{|k' - k + ke^{-iq}|^2} = \frac{k'^{2}}{k} \frac{\omega \sqrt{\frac{m}{k}} \sqrt{1 - \frac{m\omega^2}{4k}}}{(\frac{k'}{k})^2 + (1 - \frac{k'}{k}) \frac{m\omega^2}{k}}, \tag{4.17}$$

while for $|\omega| > 2\sqrt{k/m}$, we get $\Gamma(\omega) = 0$. The real part of $\Sigma^{+}(\omega)$ is the following:

$$\mathrm{Re}\left[\Sigma^{+}(\omega)\right] = \begin{cases} \frac{k'^{2}}{k} \frac{\frac{k'}{k} - \frac{m\omega^2}{2k}}{\left(\frac{k'}{k}\right)^2 + \left(1 - \frac{k'}{k}\right) \frac{m\omega^2}{k}} & ; \quad |\omega| \leq 2\sqrt{\frac{k}{m}} \\ \frac{k'^{2}}{k} \frac{\frac{k'}{k} - \frac{m\omega^2}{2k} + \frac{m\omega^2}{2k} \sqrt{1 - \frac{4k}{m\omega^2}}}{\left(\frac{k'}{k}\right)^2 + \left(1 - \frac{k'}{k}\right) \frac{m\omega^2}{k}} & ; \quad |\omega| > 2\sqrt{\frac{k}{m}}. \end{cases} \tag{4.18}$$

Note that $\mathrm{Re}\left[\Sigma^{+}(\omega)\right]$ is even with respect to ω whereas $\Gamma(\omega) = \mathrm{Im}\left[\Sigma^{+}(\omega)\right]$ is an odd function of ω. $\Sigma^{+}(\omega)$ decays to zero for $|\omega| \to \infty$ which is necessary for its Fourier transform $\Sigma(t)$ to exist. These expressions of $\Sigma^{+}(\omega)$ become particularly simple for the case $k = k'$. Finally we note that $\tilde{\gamma}(\omega) = \int_0^{\infty} dt \gamma(t) e^{i\omega t}$ is given by,

$$i\omega\tilde{\gamma}(\omega) = \Sigma^{+}(\omega) - k' \ . \tag{4.19}$$

4.2.1 Continuum string limit

An interesting special case is to consider the limit corresponding to the bath being a continuous string. This has been discussed earlier in [27] but in a somewhat different setting. We introduce a lattice spacing a and define the mass density $\sigma = m/a$, Young's modulus $E = ka$. The lattice parameter can be introduced in Eq. (4.17) and (4.18) in a consistent way by substituting $m = \sigma a$, $k = E/a$, etc. The continuum limit is obtained by taking $a \to 0$, $m \to 0$ and $k \to \infty$ while keeping E and σ constant. This then gives

$$\Gamma(\omega) = \frac{\gamma_0 \omega}{1 + \omega^2 \tau^2} \ , \quad \tilde{\gamma}(\omega) = \frac{\gamma_0}{1 - i\omega\tau}, \\ \text{where} \quad \gamma_0 = (\sigma E)^{1/2}, \quad \tau = \gamma_0 / k' \ . \tag{4.20}$$

This corresponds to the so called *Drude* model of the bath, corresponding to a dissipation kernel $\gamma(t) = (\gamma_0/\tau)e^{-t/\tau}$. Taking the strong coupling limit $k' \to \infty$, so that $\tau \to 0$, gives us the *Ohmic* bath model with

$$\Gamma(\omega) = \gamma_0 \omega, \ \tilde{\gamma}(\omega) = \gamma_0 \ , \tag{4.21}$$

which gives us a memory-less dissipation kernel $\gamma(t) = \gamma_0 \delta(t)$. We note that the presence of the phonon distribution function $f(\omega, T)$ in the quantum system ensures that the noise in Eq. (4.15) is still correlated and has memory. However, in the high temperature limit, $\beta\hbar \to 0$, we achieve the strictly Markovian limit $\langle \eta(t)\eta(t') \rangle = 2\gamma_0 k_B T \delta(t - t')$. The authors in [27] obtained the Ohmic bath starting from a continuum field description of the bath and using a different limiting procedure.

In the next section we discuss the behavior of various physical observables for the quantum Brownian particle that are obtained from the Rubin model and its limiting forms.

4.3 Mean Square Displacement, Velocity Autocorrelation Function and Response Function

In the long time limit the particle reaches the equilibrium state and we focus on properties in this state such as the mean square displacement, the velocity autocorrelation function and response functions. The mean square displacement and the velocity autocorrelation function are defined as

$$\Delta(t) = \left\langle \big(x(t) - x(0)\big)^2 \right\rangle, \ C(t) = \frac{1}{2} \langle \{v(t), v(0)\} \rangle,$$

where $\{\ldots\}$ denotes the anticommutator. The response function $R(t)$ and velocity response function $\bar{R}(t)$ are defined through the following equations for the average displacement and average velocity in the presence of a driving force $f(t)$.

$$\langle \Delta x(t) \rangle := \langle x(t) \rangle_f - \langle x(0) \rangle_{f=0} = \int_{-\infty}^{t} dt' R(t-t') f(t') \tag{4.22}$$

$$\langle v(t) \rangle = \int_{-\infty}^{t} dt' \bar{R}(t-t') f(t') \ , \tag{4.23}$$

where $\langle \cdots \rangle_f$ is the expectation value in the presence of the force and $\langle \cdots \rangle_{f=0}$ is in the absence of it. By definition $\bar{R}(t) = \dot{R}(t)$. All these three quantities can be obtained through the Fourier transform solution of Eq. (4.9) (after taking the limits $N \to \infty$ and $t_0 \to -\infty$) and Eq. (4.13). The transform $\tilde{x}(\omega) = \int_{-\infty}^{\infty} dt x(t) e^{i\omega t}$ is given by

$$\tilde{x}(\omega) = G(\omega)\tilde{\eta}(\omega), \quad \text{where} \tag{4.24}$$

$$G(\omega) = \frac{1}{-M\omega^2 + k' - \Sigma^+(\omega)} = \frac{1}{-M\omega^2 - i\omega\tilde{\gamma}(\omega)} \ . \tag{4.25}$$

Using this and the noise properties leads immediately to

$$\Delta(t) = 2\langle x^2(0) \rangle - \langle \{x(t), x(0)\} \rangle \tag{4.26}$$

$$\begin{aligned} &= \frac{\hbar}{\pi} \int_{-\infty}^{\infty} d\omega \coth(\beta\hbar\omega/2) \Gamma(\omega) G(\omega) G(-\omega) \left(1 - e^{-i\omega t}\right) \\ &= \frac{2\hbar}{\pi} \int_{0}^{\infty} d\omega \coth(\beta\hbar\omega/2) \Gamma(\omega) G(\omega) G(-\omega) \left(1 - \cos\omega t\right) \\ &= \frac{2\hbar}{\pi} \int_{0}^{\infty} d\omega \coth(\beta\hbar\omega/2) \mathrm{Im}\left[G(\omega)\right] \left(1 - \cos\omega t\right) , \end{aligned} \tag{4.27}$$

where we used the Green's function identity $\Gamma(\omega)G(\omega)G(-\omega) = [G(\omega) - G(-\omega)]/(2i)$. The velocity auto-correlation function can be obtained from $\Delta(t)$ as

$$C(t) = \frac{1}{2} \frac{d^2\Delta(t)}{dt^2} \tag{4.28}$$

$$\begin{aligned} &= \frac{\hbar}{\pi} \int_{0}^{\infty} d\omega \coth(\beta\hbar\omega/2) \Gamma(\omega) G(\omega) G(-\omega) \omega^2 \cos\omega t \\ &= \frac{\hbar}{\pi} \int_{0}^{\infty} d\omega \coth(\beta\hbar\omega/2) \mathrm{Im}\left[G(\omega)\right] \omega^2 \cos\omega t \ . \end{aligned} \tag{4.29}$$

The velocity response function is given by

$$\bar{R}(t) = \frac{1}{2\pi} \int_{-\infty}^{\infty} d\omega \frac{e^{-i\omega t}}{-i\omega M + \tilde{\gamma}(\omega)} = \frac{1}{2\pi} \int_{-\infty}^{\infty} d\omega (-i\omega) G(\omega) e^{-i\omega t} \ . \tag{4.30}$$

Whereas the relation $\bar{R}(t) = \dot{R}(t)$ gives us an expression of the position response

function,

$$R(t) = \int_0^t dt' \bar{R}(t') = \frac{1}{2\pi} \int_{-\infty}^{\infty} d\omega \; G(\omega)(e^{-i\omega t} - 1) \tag{4.31}$$

$$= \frac{1}{\pi} \int_0^{\infty} d\omega \Big(\mathrm{Re}[G(\omega)][\cos(\omega t) - 1] + \mathrm{Im}[G(\omega)] \sin(\omega t) \Big), \tag{4.32}$$

where we have used the symmetry properties of $G(\omega)$: $\mathrm{Re}[G(-\omega)] = \mathrm{Re}[G(\omega)]$ and $\mathrm{Im}[G(-\omega)] = -\mathrm{Im}[G(\omega)]$. On the other hand, the positional correlation function is given by

$$\begin{aligned} \frac{1}{i\hbar} \langle [x(t), x(0)] \rangle &= \frac{1}{\pi i} \int_{-\infty}^{\infty} d\omega \Gamma(\omega) G(\omega) G(-\omega) e^{-i\omega t} \\ &= \frac{-1}{2\pi} \int_{-\infty}^{\infty} d\omega [G(\omega) - G(-\omega)] e^{-i\omega t} \\ &= \frac{-1}{\pi} \int_{-\infty}^{\infty} d\omega \mathrm{Im}[G(\omega)] \sin(\omega t) \; . \end{aligned} \tag{4.33}$$

Using the Kramer's Kronig identity, $\int_{-\infty}^{\infty} d\omega \; \mathrm{Im}[G(\omega)] \sin(\omega t) = \int_{-\infty}^{\infty} d\omega \; \mathrm{Re}[G(\omega)][\cos(\omega t) - 1]$, we verify explicitly that the linear response formula

$$R(t) = -\frac{1}{i\hbar} \langle [x(t), x(0)] \rangle, \tag{4.34}$$

holds exactly. This is expected since the dynamics of system and bath is completely linear.

4.4 Comparison of the forms of $\gamma(t)$, $\Delta(t)$ and $C(t)$ for the three models

4.4.1 Form of $\gamma(t)$

Rubin model: In this case one can obtain the expression of $\tilde{\gamma}(\omega)$ using Eq. (4.16) and Eq. (4.19):

$$\mathrm{Re}\left[\tilde{\gamma}(\omega)\right] = \begin{cases} \frac{k'^2}{k} \sqrt{\frac{m}{k}} \frac{\sqrt{1 - \frac{m\omega^2}{4k}}}{\left(\frac{k'}{k}\right)^2 + \left(1 - \frac{k'}{k}\right)\left(\frac{m\omega^2}{k}\right)} & ; \quad |\omega| \leq 2\sqrt{\frac{k}{m}} \\ 0 & ; \quad |\omega| > 2\sqrt{\frac{k}{m}} \end{cases} \tag{4.35}$$

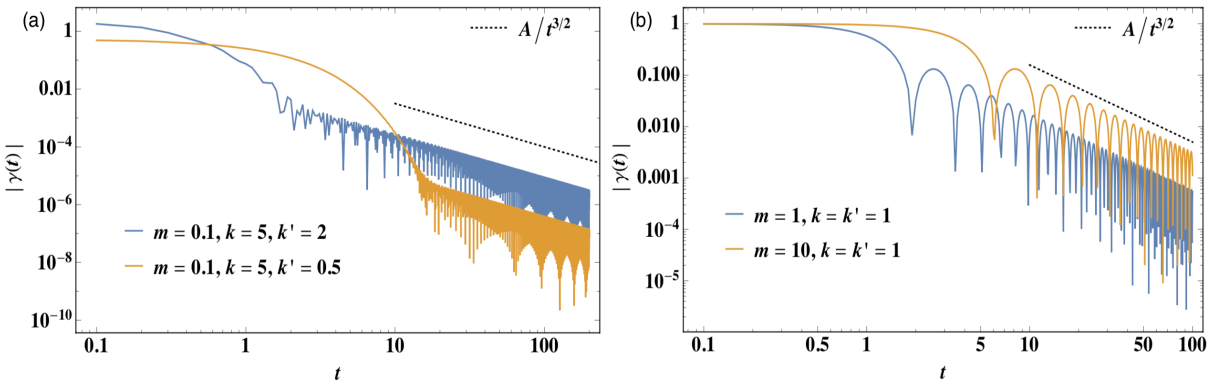

Figure 4.2: **(Rubin model)** Log-Log plot of $|\gamma(t)|$ for a set of values of m, k, k' to show that $\gamma(t)$ initially decays fast and then as a power law $\sim t^{-3/2}$. We propose that the crossover time, t^*, can be estimated from the location of the branch point of $\tilde{\gamma}(\omega)$: $t^* \propto \sqrt{\frac{m}{k'}\left(\frac{k}{k'}-1\right)}$ when $k > k'$ and $t^* \propto \sqrt{\frac{m}{k}}$ for $k \leq k'$. (a) $(k > k')$; if we decrease just k' by a factor of 4 keeping other parameters fixed, t^* increases 4 times. (b) $(k = k')$; m is increased by 10 times, which results in a shift of t^* by a factor of $\sqrt{10}$. These observations support our claim about the crossover time.

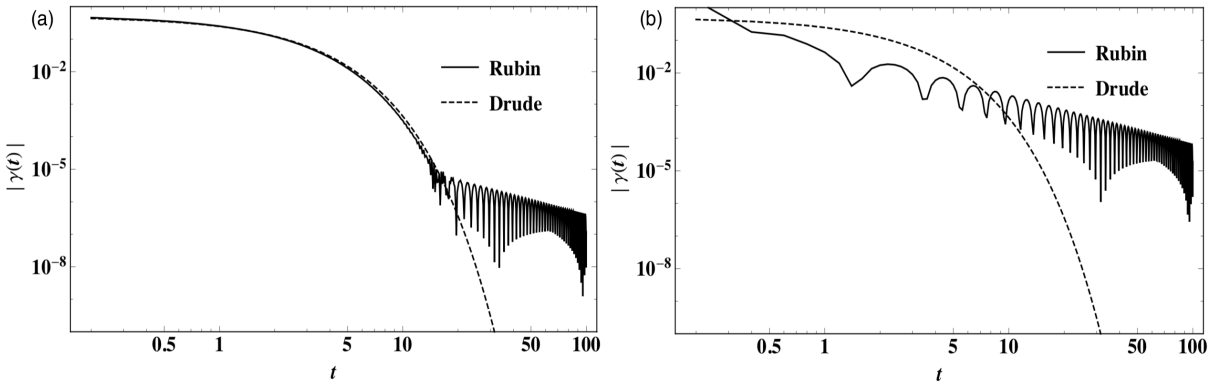

Figure 4.3: **Comparison of $\gamma(t)$ between the Rubin and Drude models:** (a) Weak coupling case $\boldsymbol{k' = 0.5}$; (b) Strong coupling case with $\boldsymbol{k' = 4.0}$. Other parameters are taken as $M = 1, m = 0.1, k = 5$. This data supports the fact that the Drude approximation of the Rubin bath is good when k is large but k' is not. If both k and k' are made large, the Ohmic approximation is better than the Drude.

$$\mathrm{Im}\left[\tilde{\gamma}(\omega)\right] = \begin{cases} m\omega \frac{\frac{k'}{k} - \frac{1}{2}\left(\frac{k'}{k}\right)^2}{\left(\frac{k'}{k}\right)^2 + \left(1-\frac{k'}{k}\right)\left(\frac{m\omega^2}{k}\right)} & ; \quad |\omega| \leq 2\sqrt{\frac{k}{m}} \\ m\omega \frac{\frac{k'}{k} - \frac{1}{2}\left(\frac{k'}{k}\right)^2\left[1+\sqrt{1-\frac{4k}{m\omega^2}}\right]}{\left(\frac{k'}{k}\right)^2 + \left(1-\frac{k'}{k}\right)\left(\frac{m\omega^2}{k}\right)} & ; \quad |\omega| > 2\sqrt{\frac{k}{m}}. \end{cases} \tag{4.36}$$

Note that $\mathrm{Re}\left[\tilde{\gamma}(\omega)\right]$ is odd function of ω while $\mathrm{Im}\left[\tilde{\gamma}(\omega)\right]$ is even. This property is common for various response functions in physical systems. For the special case $k = k'$, it is possible to evaluate $\gamma(t) = \frac{1}{2\pi}\int_{-\infty}^{\infty} d\omega\ \tilde{\gamma}(\omega)e^{-i\omega t}$ to obtain

$$\gamma(t) = \frac{\sqrt{km}J_1\left(2\sqrt{\frac{k}{m}}t\right)}{t}\ , \tag{4.37}$$

where J_n is the Bessel function of 1st kind. Since $J_n(x) \sim \sqrt{\frac{2}{\pi x}}\cos\left[x - (n+1/2)\frac{\pi}{2}\right]$ at large x, we get the leading order asymptotic behavior $\gamma(t) \sim t^{-3/2}$. This leading asymptotic form can be seen as arising from the branch point at $\omega = 2\sqrt{k/m}$ in the integrand in Eq. (4.35). For the general case, $k \neq k'$, we note that the integrand has additional poles at $\omega = k'/\sqrt{m(k'-k)}$. For $k > k'$, this is imaginary and gives rise to an exponentially decaying part in $\gamma(t)$. Thus we expect that for $k > k'$, $\gamma(t)$ should initially have a fast exponential decay $\sim e^{-w_p t}$,where $\omega_p = k'/\sqrt{m(k-k')}$. After a time scale $t_c \approx 2\pi/\omega_p$, this is followed by a $\sim t^{-3/2}$ decay. This feature is clearly seen in the numerical evaluation of $\gamma(t)$ is presented in Fig. (4.2) for two different parameter sets. In [31] the authors have addressed this question of crossover timescales in a similar system heuristically.

Drude bath and Ohmic bath limits : From Eq. (4.20) one obtains $\gamma(t) = \frac{\gamma_0}{\tau}e^{-t/\tau}$ and $\Sigma(t) = \frac{\gamma_0}{\tau^2}e^{-t/\tau}$. Ohmic bath is obtained simply taking the limit $\tau \to 0$ and gives $\gamma(t) = \gamma_0\delta(t)$.

In Fig. (4.3) we show a comparison of the forms of $\gamma(t)$ obtained from the Rubin and Drude models. As expected we see that for the weak-coupling case ($k' = 0.5$), we expect an exponential decaying regime for the Rubin model over the time-scale $t_c \approx 2\pi/\omega_p \approx 25.3$ and here we see agreement with the Drude model. On the other hand, when $k' = 4.0$, we see that $t_c \approx 1.5$ and correspondingly one finds that there is no regime where the Drude approximation is good.

We next explore the question on how well the behavior of other physical observables such as $\Delta(t)$ and $C(t)$ are reproduced by the Drude and Ohmic approximations.

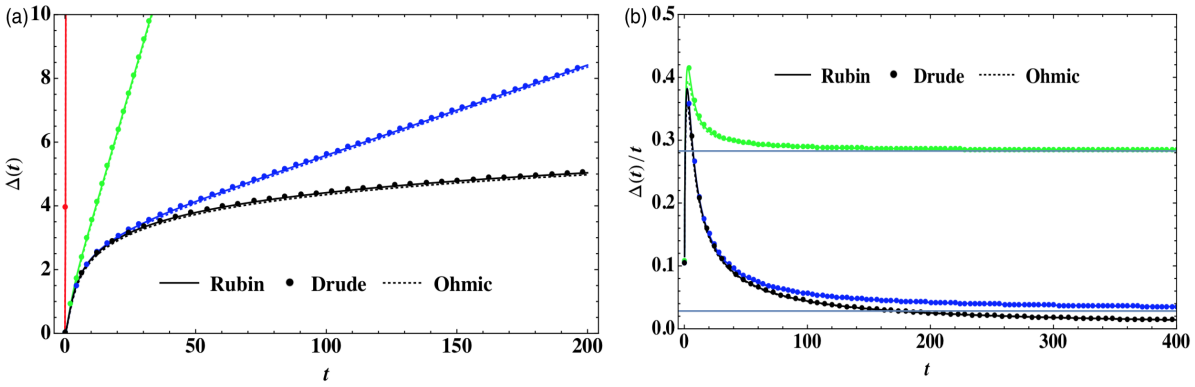

Figure 4.4: (a) Comparison of $\Delta(t)$ between the Rubin, Drude and Ohmic models. T he β values from the top are $0.01, 10, 100$ and ∞ (from above). (b) For the β values $10, 100, \infty$ (from above) we plot $\Delta(t)/t$. Other parameters are taken as $M = 1, m = 0.1, k = 5, \boldsymbol{k' = 4.0}$. This figure is the counterpart of Fig. (4.7) with k and k' both large. The saturation values (0.283 and 0.0283) are indicated in the figure. We see a agreement between the three models compared to Fig. (4.7).

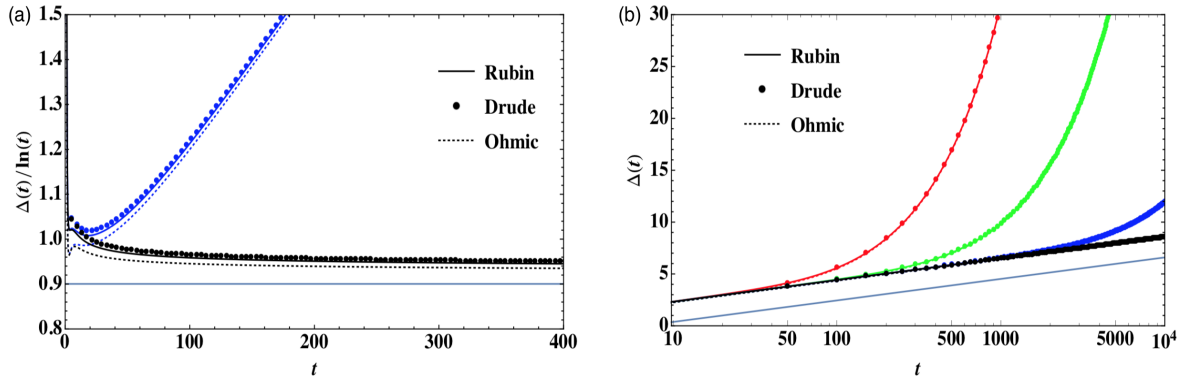

Figure 4.5: (a) Comparison of $\Delta(t)/\ln(t)$ between the Rubin, Drude and Ohmic models for $\beta = 10, \infty$ (from above) in linear scale. (b) $\Delta(t)$ in log-linear scale for $\beta = 100, 500, 5000, \infty$ (from above). Other parameters were taken as $M = 1, m = 0.1, k = 5, \boldsymbol{k' = 4.0}$. Note the match between different models, as k and k' both are large in contrast to Fig. (4.8). From Eq. (4.42) the prefactor of $\ln(t)$ is $2\hbar/\pi\gamma_0 = 0.9$ which has been indicated both in (a) and (b).

4.4.2 Form of $\Delta(t)$

To compute $\Delta(t), C(t)$, and $R(t)$ we need information on Im $[G(\omega)]$. Using Eqs. (4.25), (4.35) and (4.36) we get,

$$\text{Im}\left[G(\omega)\right] = \frac{\frac{k'^2}{k}\frac{1}{m\omega^3}\sqrt{\frac{1}{mk}}\sqrt{1-\frac{m\omega^2}{4k}}\left(\left[\frac{k'}{k}\right]^2+\frac{m\omega^2}{k}\left[1-\frac{k'}{k}\right]\right)}{\left[\frac{M\omega^2}{k}\left[1-\frac{k'}{k}\right]+\frac{k'^2}{k^2}\left[\frac{M}{m}+\frac{1}{2}\right]-\frac{k'}{k}\right]^2+\frac{k'^4}{m\omega^2k^3}\left[1-\frac{m\omega^2}{4k}\right]}; \tag{4.38}$$

for $|\omega| \leq 2\sqrt{k/m}$ and 0 for $|\omega| > 2\sqrt{k/m}$.

The corresponding forms for the Drude bath is given by:

$$\text{Im}[G(\omega)] = \frac{\gamma_0}{\omega\left[M^2\omega^2 + (M\omega^2\tau - \gamma_0)^2\right]}. \tag{4.39}$$

Ohmic bath is obtained from the above expression by letting $\tau \to 0$. Most of the integrals of $\Delta(t)$ and $C(t)$ for the Rubin model are intractable analytically, but can be done numerically to extract some limiting behaviors:

Numerical results from the evaluation of the integral Eq. (4.27) and a comparison with results from the corresponding Drude and Ohmic limits is shown in Figs. (4.4), (4.5), (4.6), (4.7), and (4.8).

Some of the interesting observations can be summarized as follows:

1. At long times we see a linear growth of $\Delta(t)$ with time, at all finite temperatures, as expected for a diffusive system. We notice that the integrand has an oscillatory factor $[1-\cos(\omega t)]$, so at large t the major contribution to the integral comes from $\omega << 1/t$. Hence, for any non-vanishing β, we take $\coth\left(\frac{\beta\hbar\omega}{2}\right) \to \frac{2}{\beta\hbar\omega}$ to get (in the $t \to \infty$ limit):

$$\begin{aligned}\Delta(t) &= \frac{4}{\pi\beta}\int_0^\infty d\omega\Big(\omega\text{Im}[G(\omega)]\Big)_{\omega\to 0}\frac{1-\cos(\omega t)}{\omega^2} \\ &= \frac{2}{\beta\sqrt{mk}}t = 2Dt \qquad (4.40)\end{aligned}$$

$$\text{where}\quad D = \frac{1}{\beta\sqrt{mk}} = \frac{k_BT}{\gamma_0} \tag{4.41}$$

can be identified as the usual diffusion constant satisfying the Stokes-Einstein relation. In Fig. (4.7b) and (4.4b), we verify that $\Delta(t)/t$ does converge to this limit at finite temperatures. As can be seen from this figure, the long time asymptotics of $\Delta(t)$ and the diffusion constant are thus correctly obtained by both the Drude and Ohmic limits. The Diffusion constant values are specified in Fig. (4.7b) for two different β values and other parameter choices. Note that D vanishes at zero temperature ($\beta = \infty$), which is also clear from the Fig. (4.7b).

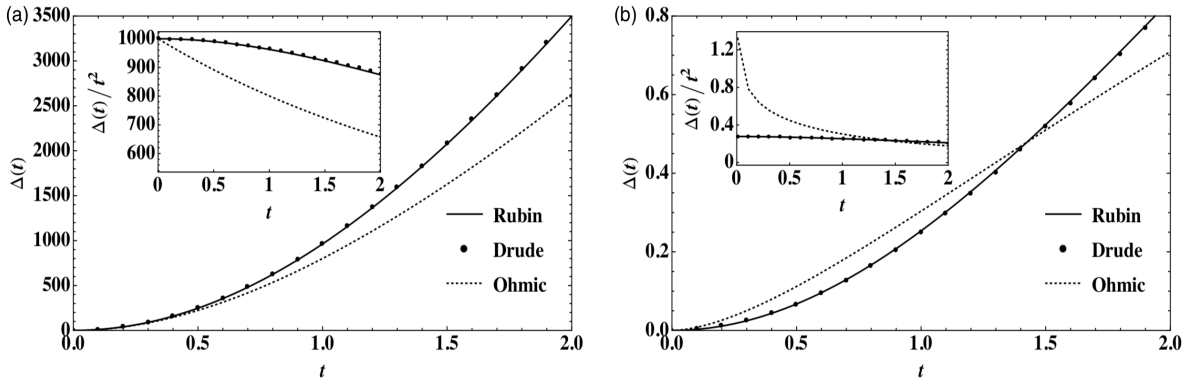

Figure 4.6: Comparison of $\Delta(t)$ between the Rubin, Drude and Ohmic models at short times. (a) $\beta = 0.001$. We can see that at high temperatures $\Delta(t)$ behaves as $\sim t^2$ for all three models. The correction to the t^2 behavior for the Ohmic case is t^3, which is evident from the inset. (b) $\beta = 100$. At low and finite temperatures, the short time behavior is $\sim -t^2 \ln(t)$ for the Ohmic bath whereas it is $\sim t^2$ for the Rubin and Drude baths. Other parameters are $M = 1, m = 0.1, k = 5, k' = 0.5$. Note that the log divergence of $C(0)$ for the Ohmic case is present at any finite temperature and diminishes for $\beta\hbar$ is equal to zero, which is hard to achieve numerically. Thus in the data presented in (a) for the Ohmic case, we have taken the classical limit first and then performed the integral.

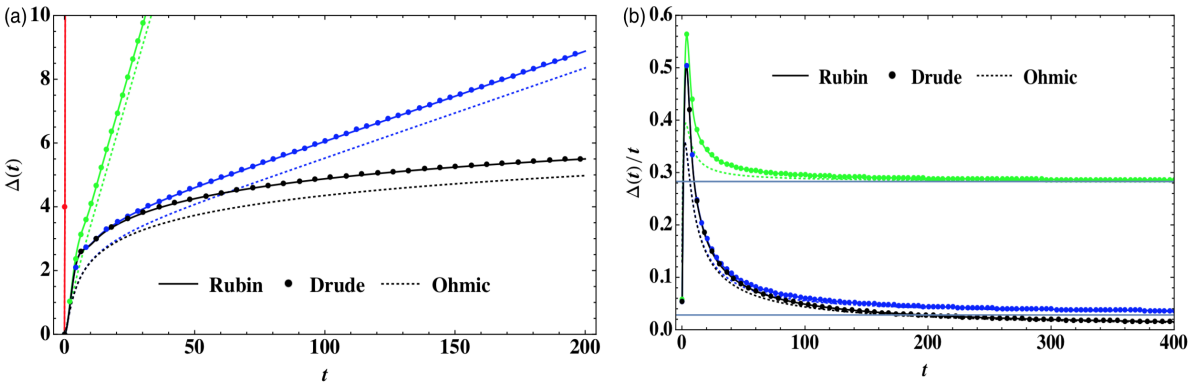

Figure 4.7: **Comparison of $\Delta(t)$ between the Rubin, Drude and Ohmic models:** (a)The β values are $0.01, 10, 100$ and ∞ (from above). (b) For the β values $10, 100, \infty$ (from above) we plot $\Delta(t)/t$. We verify the asymptotic formulas presented in Eq. (4.40) and (4.41) at finite temperatures. At $\beta = 10$, the saturation value is $2D = 2/\beta\sqrt{km} = 0.283$ and for $\beta = 100$ it's 0.0283 which match with the data. These saturation values are indicated in the figure. Other parameters were taken as $M = 1, m = 0.1, k = 5, \boldsymbol{k' = 0.5}$.

2. At zero temperature ($\beta \to \infty$) we find that $\Delta(t)$ has a slower logarithmic growth at large times. In this quantum regime we have $\coth\left(\frac{\beta\hbar\omega}{2}\right) = 1$ and the integrals simplify. As before, we have to consider only the small ω contribution to the integral for the large time asymptotic behavior of $\Delta(t)$

$$\begin{aligned}\Delta(t) &\simeq \frac{2\hbar}{\pi}\int_0^{2\sqrt{k/m}} d\omega \Big(\omega \mathrm{Im}[G(\omega)]\Big)_{\omega\to 0} \frac{1-\cos(\omega t)}{\omega} \\ &\simeq \frac{2\hbar}{\pi\gamma_0}\ln(t)\ . \end{aligned} \tag{4.42}$$

In Fig. (4.8a) we verify this form and the value of the prefactor of $\ln(t)$. We see that Rubin, Drude and Ohmic models reproduce the logarithmic growth. The prefactors of $\ln(t)$ are same, which is evident from Fig. (4.8b) and Fig. (4.5b), as the slopes of different models of the linear regime are same in log-linear scale. Note that there must be a timescale included in the argument of the log for dimensional constraints. The log behavior can be represented by, $\Delta(t) \sim A + B\ln(t)$, which implies that $\Delta(t)/\ln(t) \sim A/\ln(t) + B$. As $\ln(t)$ is a slowly varying (increasing) function of t, there is a slow convergence to the model independent pre-factor B of $\ln(t)$, as seen in Fig. (4.8a) and Fig. (4.5a). The chosen parameters are mostly $M = 1, m = 0.1, k = 5, k' = 0.5$ or 4 throughout the numerical data presented here for various β values. For Drude and Ohmic baths, γ_0 and τ are also chosen correspondingly [see Eq. (4.20)].

3. At finite temperatures, the cross-over from the quantum (logarithmic growth) to the classical (linear growth) takes place at the time scale $t_{\rm qc} \sim \beta\hbar$. We study this timescale in the Fig. (4.8b) and Fig. (4.5b), by plotting the $\Delta(t)$ for various β values keeping $\hbar = 1$. In the log-linear scale, the log behavior of $\Delta(t)$ is represented by a linear regime which persists up to a timescale of the order of $\beta\hbar$.

4. Finally we discuss the short time behavior. At high temperatures, we approximate $\frac{1-\cos(\omega t)}{\omega^2} \sim t^2/2$ and $\coth\left(\frac{\beta\hbar\omega}{2}\right) \sim \frac{2}{\beta\hbar\omega}$, to obtain

$$\Delta(t) \simeq \frac{2}{\pi\beta}t^2\int_0^{2\sqrt{\frac{k}{m}}} d\omega\ \omega \mathrm{Im}[G(\omega)] \sim c\frac{k_B T}{M}t^2\ , \tag{4.43}$$

where c is a dimensionless constant. The ballistic growth can be simply understood as that of a thermal particle with $\langle v^2\rangle = k_B T/M$. On the other hand at zero temperature, we get

$$\Delta(t) \simeq c'\ \frac{\hbar k^{1/2}}{M^{3/2}}t^2\ , \tag{4.44}$$

where $c' = [2M^{3/2}/(k^{1/2}\pi)]\int_0^{2\sqrt{k/m}} d\omega\ \omega^2 \mathrm{Im}[G(\omega)]$ is a dimensionless constant. The

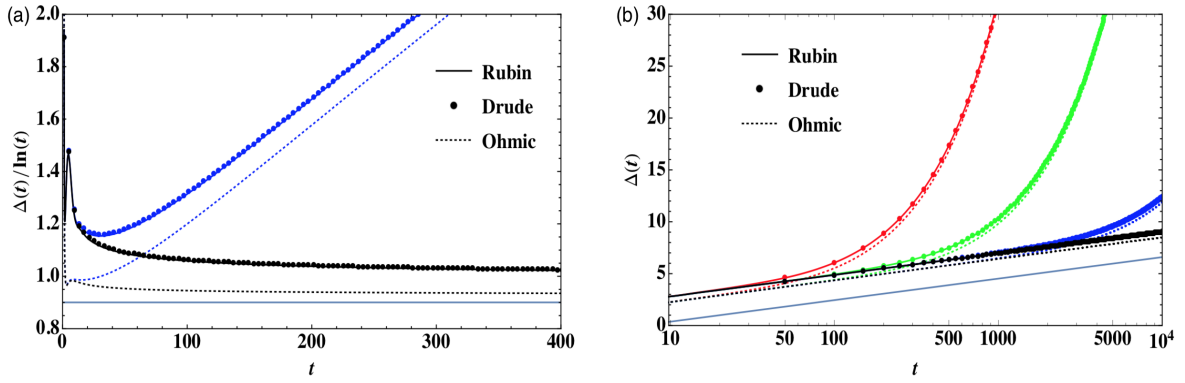

Figure 4.8: (a) Comparison of $\Delta(t)/\ln(t)$ between Rubin, Drude and Ohmic $\beta = 10, \infty$ (from above) in linear scale. (b) $\Delta(t)$ in log-linear scale for $\beta = 100, 500, 5000, \infty$ (from above). This figure indicates the log behavior of $\Delta(t)$ for all three models with same pre-factors (slopes of the linear region) up to a time scale of the order of $\sim \beta\hbar$. Beyond this timescale $\Delta(t)$ behaves linearly in time which causes an exponential growth in log-linear scale. Other parameters were taken as $M = 1, m = 0.1, k = 5, \boldsymbol{k' = 0.5}$. We note that the Rubin and Drude models are matching well but the Ohmic is deviating. This is happening because k is large but k' is relatively small. However, as (b) suggests, the prefactors of $\ln(t)$ are same for these models and hence there is a slow convergence of the data at (a) for $\beta = \infty$. From Eq. (4.42) the prefactor of $\ln(t)$ is $2\hbar/\pi\gamma_0 = 0.9$ which has been indicated both in (a) and (b).

ballistic growth in this case roughly corresponds to a particle with velocity fluctuations determined by the zero point energy so that $\langle v^2 \rangle = \hbar(k/M)^{1/2}/M$.

As presented in the Fig. (4.6a), we see that in the high temperature limit, all three models show the t^2 behavior with same prefactor. This is consistent with the equipartition interpretation.

At zero temperature or any finite temperature, the Drude and Rubin models have the expected form of (4.44) with same pre-factor while the Ohmic model has a logarithmic correction given by:

$$\Delta(t) \simeq -\frac{\hbar\gamma_0}{M^2\pi} t^2 \ln\left(\gamma_0 t/M\right) + \mathcal{O}\left[t^4 \ln(t)\right]. \tag{4.45}$$

The data is presented in Fig. (4.6b).

4.4.3 Form of $C(t)$

$C(t)$ is obtained from $\Delta(t)$ by taking two time derivatives [Eq. (4.28)]. Numerical data is presented in Fig. (4.9). Some important features are the following:

1. One general feature is a damped oscillatory behavior in most of the parameter regimes. We can also see the agreement between the three models when both k

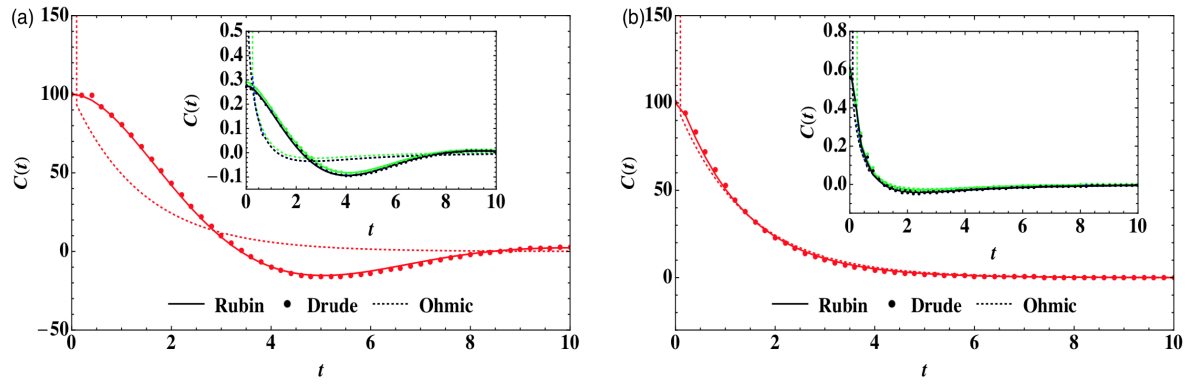

Figure 4.9: **Comparison of $C(t)$ between the Rubin, Drude and Ohmic baths:** (a) $M = 1, m = 0.1, k = 5, \boldsymbol{k' = 0.5}$. The main figure shows $\beta = 0.01$ and the inset shows $\beta = 10, 100, \infty$ (from above). (b) $M = 1, m = 0.1, k = 5, \boldsymbol{k' = 4}$. The main figure shows $\beta = 0.01$ and the inset shows $\beta = 10, 100, \infty$ (from above). As in the case of $\Delta(t)$, there is a better agreement between the Rubin and Drude models than the Ohmic bath when k value is sufficiently large but k' is not. And all three models coincide when k and k' both are chosen to large. Near $t = 0$, there is a log divergence, which is only present in the Ohmic case [see Eq. (4.46)] and this deviation is always visible near $t = 0$.

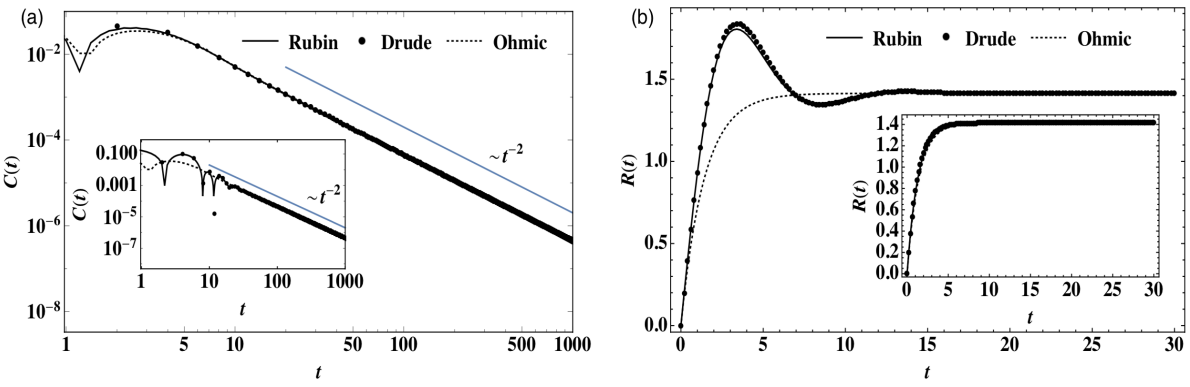

Figure 4.10: (a) $C(t)$ at large times for $M = 1, m = 0.1, k = 5, \boldsymbol{k' = 4}$ and $\beta = \infty$. The inset shows the same plot for $\boldsymbol{k' = 0.5}$. $C(t)$ behaves as $1/t^2$ as discussed in the text. (b) Comparison of the response function $R(t)$ between the three models for $M = 1, m = 0.1, k = 5, \boldsymbol{k' = 0.5}$. The inset shows the same plot for $\boldsymbol{k' = 4}$. $R(t)$ saturates to the value $R_\infty = 1/\gamma_0 = 1/\sqrt{km} = 1.414$ [see Eq. (4.47)].

and k' are chosen to be large. However there is a significant deviation of the Ohmic bath near $t = 0$.

2. In case of the Rubin and Drude model, at all temperatures, $\Delta(t)$ behaves as $\sim t^2$ near $t = 0$ which gives a finite value of $C(0)$. Note that $C(0) = k_B T/M$ in classical regime and $C(0) = \hbar(k/M)^{1/2}/M$ in quantum regime. $C(t) \sim C(0) + \mathcal{O}(t^2)$ at small times.

   However, for Ohmic bath, from Eq. (4.45) we get,

$$C(t) \simeq -\frac{\gamma_0 \hbar}{\pi m^2} \ln(\gamma_0 t/M) + \mathcal{O}\left[t^2 \ln(t)\right]. \tag{4.46}$$

   This log divergence near $t = 0$ explains the deviation from other bath models shown in Fig. (4.9). Although the Eq. (4.45) was derived for low temperatures, this log divergence shows up at any finite temperature. In the classical limit, i.e. when $\beta\hbar = 0$, one gets an exponential decay of the velocity autocorrelation.

3. In the previous section, we obtained the leading order term for the $\Delta(t)$, which behaves as $\sim t$ in the large time limit at any finite temperature. If we take double derivatives naively, it does not lead to the correct leading order asymptote of $C(t)$. In a detailed calculation (to be published), we have shown that the correction to this linear behavior is $\sim e^{-ct}$ for the Drude and Ohmic models and $\sim \cos(\omega t)/t^{3/2}$ for the Rubin bath. Thus the large time behavior ($t >> \beta\hbar$) of $C(t)$ is $\sim e^{-ct}$ for the Drude and Ohmic baths and $\sim \cos(t)/t^{3/2}$ for Rubin. At zero temperature or $t << \beta\hbar$ the leading order behaviors are $\sim 1/t^2$ for all three models.

4.4.4 Form of $R(t)$

Using Eq. (4.31) we obtain,

$$R(t) = \left[1 - \exp(-\gamma_0 t/m)\right]/\gamma_0 \tag{4.47}$$

for the Ohmic model. For Drude model, the integrals can also be evaluated exactly and $R(t)$ takes similar functional form. The general feature that $R(t)$ increases initially and then saturates to a value is present in all models and parameter regimes. This behavior physically describes the fact that if we perturb the Brownian particle, it will initially have a directional displacement before it becomes completely random. For the Rubin bath the integrals are intractable. Data from numerical integration for all three modes are shown in Fig. (4.10).

Numerical details: To perform the integrals numerically MATHEMATICA has been used extensively, especially the NIntegrate command. To obtain the analytical and asymptotic formulas, doing the summations, etc., the commands like Integrate, AsymptoticIntegrate, Series, FullSimplify, etc. of MATHEMATICA have been particularly used.

4.5 Summary

In this chapter we study in detail the well-known Rubin bath model, which consists of a one-dimensional semi-infinite harmonic chain with the boundary bath particle coupled to a test particle, which is then shown to effectively execute Brownian motion.

We point out two interesting and important limits of the Rubin model: (i) the Drude model which is obtained in the infinite bath bandwidth limit of the Rubin model and (ii) the Ohmic model which, in addition to an infinite bath bandwidth, also needs the limit of infinite system-bath coupling. For the Rubin model and the special limiting cases, we analyze in detail the temporal dependence of the mean square displacement, the velocity autocorrelation function and the response function. In addition, we studied the crossover behavior of the dissipation kernel $\gamma(t)$ from an exponentially decaying behavior at short times to an oscillatory power law ($\sim t^{-3/2}$) decaying behavior at larger times.

Taking the special limits of either the Drude and Ohmic baths is useful since the bath kernels are much simpler and the mathematical analysis becomes considerably simpler. In real physical situations one might have large but finite bath bandwidths and system-bath couplings. One important question in these situations is as to how closely physical properties are reproduced when we ignore the fact that the original Rubin bath kernel has long time power-law tails. Our numerical results show that many properties are indeed accurately reproduced by the approximate models. In particular, we discussed the quantum to classical crossover time scales where the mean square displacement changes from a logarithmic to a linear time dependence. The analysis presented in this work provides a microscopic justification for the choice of the position response function used in a recent analysis [29] of quantum Brownian motion based on linear response theory as the starting point.

We have shown that the Ohmic limit, when the dissipation kernel becomes a δ-function, is obtained in the limit of a continuum string and surprisingly, for strong coupling. This is unlike the weak coupling limits usually discussed in the derivation of quantum master equations in the literature [32, 33]. An interesting observation is that at any finite temperature the noise correlations always have a finite correlation time even in the Ohmic limit when the dissipation kernel becomes a δ-function. Thus a quantum bath is never truly Markovian. However at high temperatures one can make the approximation $\coth(\beta\hbar\omega/2) \to 2/(\beta\hbar\omega)$ in the noise correlations and then get the Markovian

limit. Thus our study shows the precise conditions under which the Markovian approximation is valid. We note that the microscopic derivation of quantum master equations typically starts with exactly the same system-bath setup as the one used in the derivation of the quantum Langevin equation. There, the Born-Markov approximation leads to the Redfield equation and further approximations lead to the Lindblad equation which is Markovian. The precise conditions for the validity of the Born-Markov approximation are however subtle and not clearly understood [32–34] and we believe that our work, with very explicit results, could provide insights on this issue.

Bibliography

[1] P. Langevin, "Sur la théorie du mouvement brownien," Compt. Rendus **146**, 530–533 (1908).

[2] G. W. Ford, M. Kac, and P. Mazur, "Statistical mechanics of assemblies of coupled oscillators," J. Math. Phys. **6**, 504–515 (1965).

[3] N. G. Van Kampen, *Stochastic processes in physics and chemistry*, 3rd ed. (Elsevier, 2007).

[4] U. Weiss, *Quantum Dissipative Systems*, 4th ed. (World Scientific, 2012).

[5] P. E. Phillipson, "Effects of long range interactions in harmonically coupled systems. i. equilibrium fluctuations and diffusion," J. Math. Phys. **15**, 2127–2147 (1974).

[6] V. Hakim and V. Ambegaokar, "Quantum theory of a free particle interacting with a linearly dissipative environment," Phys. Rev. A **32**, 423 (1985).

[7] H. Grabert, P. Schramm, and G. L. Ingold, "Quantum brownian motion: The functional integral approach," Physics reports **168**, 115–207 (1988).

[8] G. W. Ford, J. T. Lewis, and R. F. O'Connell, "Quantum langevin equation," Phys. Rev. A **37**, 4419–4428 (1988).

[9] A. O. Caldeira and A. J. Leggett, "Path integral approach to quantum brownian motion," Physica A: Statistical Mechanics and its Applications **121**, 587 – 616 (1983).

[10] R. P. Feynman and F. L. Vernon, "The theory of a general quantum system interacting with a linear dissipative system," Annals of Physics **24**, 118 – 173 (1963).

[11] R. Balescu, *Equilibrium and nonequilibrium statistical mechanics* (John Wiley & Sons, 1975).

[12] P. C. Hemmer, *Dynamic and stochastic types of motion in the linear chain* (Norges tekniske hoiskole, 1959).

[13] P. Mazur and E. Montroll, "Poincaré cycles, ergodicity, and irreversibility in assemblies of coupled harmonic oscillators," Journal of mathematical physics **1**, 70–84 (1960).

[14] R. J. Rubin, "Statistical dynamics of simple cubic lattices. model for the study of brownian motion," Journal of Mathematical Physics **1**, 309–318 (1960).

[15] R. E. Turner, "Motion of a heavy particle in a one dimensional chain," Physica **26**, 269–273 (1960).

[16] R. E. Turner, "Temporal fluctuations in a classical linear system," Physica **26**, 274–283 (1960).

[17] R. J. Rubin, "Statistical dynamics of simple cubic lattices. model for the study of brownian motion. ii," Journal of Mathematical Physics **2**, 373–386 (1961).

[18] P. Mazur and E. Braun, "On the statistical mechanical theory of brownian motion," Physica **30**, 1973–1988 (1964).

[19] P. Ullersma, "An exactly solvable model for brownian motion: I. derivation of the langevin equation," Physica **32**, 27–55 (1966).

[20] P. Ullersma, "An exactly solvable model for brownian motion: III. motion of a heavy mass in a linear chain," Physica **32**, 74–89 (1966).

[21] R. Zwanzig, "Nonlinear generalized langevin equations," Journal of Statistical Physics **9**, 215–220 (1973).

[22] C. Presilla, R. Onofrio, and U. Tambini, "Measurement quantum mechanics and experiments on quantum zeno effect," annals of physics **248**, 95–121 (1996).

[23] C. Presilla, R. Onofrio, and M. Patriarca, "Classical and quantum measurements of position," Journal of Physics A: Mathematical and General **30**, 7385 (1997).

[24] P. Hänggi and G. L. Ingold, "Fundamental aspects of quantum brownian motion," Chaos: An Interdisciplinary Journal of Nonlinear Science **15**, 026105 (2005).

[25] S. T. Smith and R. Onofrio, "Thermalization in open classical systems with finite heat baths," The European Physical Journal B **61**, 271–275 (2008).

[26] A. Lampo, M. G. March, and M. Lewenstein, *Quantum Brownian motion revisited: extensions and applications* (Springer, 2019).

[27] J. P. Eckmann, C. A. Pillet, and L. Rey-Bellet, "Non-equilibrium statistical mechanics of anharmonic chains coupled to two heat baths at different temperatures," Communications in Mathematical Physics **201**, 657–697 (1999).

[28] S. Sinha and R. D. Sorkin, "Brownian motion at absolute zero," Phys. Rev. B **45**, 8123–8126 (1992).

[29] U. Satpathi, S. Sinha, and R. D. Sorkin, "A quantum diffusion law," J. Stat. Mech.: Theory Exp. **12**, 123105 (2017).

[30] S. G. Das and A. Dhar, "Landauer formula for phonon heat conduction: relation between energy transmittance and transmission coefficient," Eur. Phys. J. B **85**, 372 (2012).

[31] A. Chakraborty and R. Sensarma, "Power-law tails and non-markovian dynamics in open quantum systems: An exact solution from keldysh field theory," Phys. Rev. B **97**, 104306 (2018).

[32] H. J. Carmichael, *Statistical methods in quantum optics 1: master equations and Fokker-Planck equations* (Springer Science & Business Media, 2013).

[33] H. P. Breuer, F. Petruccione, *et al.*, *The theory of open quantum systems* (Oxford University Press on Demand, 2002).

[34] A. Purkayastha, A. Dhar, and M. Kulkarni, "Out-of-equilibrium open quantum systems: A comparison of approximate quantum master equation approaches with exact results," Physical Review A **93**, 062114 (2016).